

UNIVERSITY OF CALIFORNIA

Los Angeles

**Resonant And Non-Resonant Beat-Wave Excitation Of
Relativistic Plasma Waves**

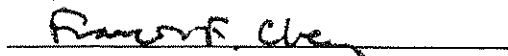
A dissertation submitted in partial satisfaction of the
requirements for the degree
Doctor of Philosophy in Electrical Engineering

by

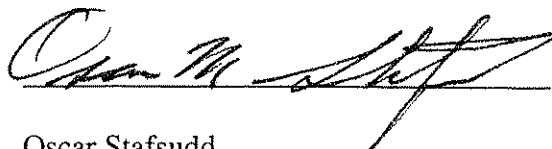
Catalin Vasile Filip

2003

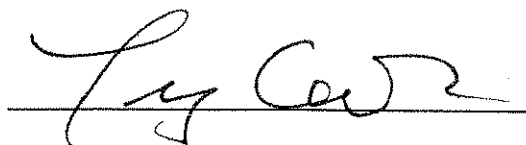
The dissertation of Catalin Vasile Filip is approved.



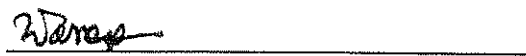
Francis F. Chen



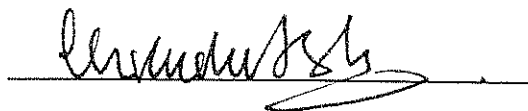
Oscar Stafsudd



Troy Carter



Warren Mori



Chan Joshi, Committee Chair

University of California, Los Angeles

2003

DEDICATION

To my parents, Victoria and Ion.

Contents

DEDICATION	iii
List of Figures	vii
List of Tables	x
ACKNOWLEDGMENTS	xi
VITA AND PUBLICATIONS	xii
ABSTRACT	xvi
1. Introduction	1
2. Introduction to beat-wave excitation of collective motion of the plasma	
electrons	6
2.1 The ponderomotive force.....	6
2.2 Beat-wave excitation of relativistic plasma waves.....	10
3. Simulations	12
3.1 Resonant Excitation.....	12
3.2 Non-Resonant Excitation.....	24
4. Experimental apparatus	35
4.1 Introduction.....	35
4.2 The Neptune Laser System.....	35

4.3 Neptune Experimental Area.....	46
5. Collinear Thomson Scattering Diagnostic System	50
5.1 Introduction.....	50
5.2 Experimental Setup.....	54
5.3 The Etalon.....	61
5.4 The Filtering Grating.....	64
5.5 Detection System.....	68
5.6 White light characterization of the entire optical system.....	71
6. Experimental Results	75
6.1 F/3 Collinear Thomson Scattering.....	75
6.2 F/18 Collinear Thomson Scattering And Electron Injection.....	87
7. Conclusions	93
Appendix A. Motion Of A Free Electron In The Field Of A Plane EM	
Wave	96
Appendix B. Experimental Measurements Based On The Optical Kerr	
Effect	102
B.1 Production Of Picosecond, Multi-Wavelength CO ₂ Laser Pulses.....	102
B.2 Portable Kerr Setup For The Measurement Of CO ₂ Pulses.....	111
B.3 Delay Of The CO ₂ Pulses In The Large Aperture Amplifier.....	112
Appendix C. 90° Thomson Scattering From Non-Relativistic	
Plasma Waves	116
C.1 Scattering Geometry.....	116

C.2 Experimental Setup.....	119
C.3 Experimental Results.....	120
Appendix D. High-Amplitude Non-Resonant Plasma Waves	126
Bibliography	133

List Of Figures

2.1	Trajectory Of A Free Electron In The Field Of A EM Wave.....	8
2.2	Bunching Of Plasma Electrons By The Ponderomotive Force.....	9
3.1	Snapshot Of The Intensity Of The Laser Pulse At Resonance.....	13
3.2	Snapshot Of The Longitudinal Electric Field At Resonance.....	14
3.3	Phase Velocity Of The Plasma Wave At Resonance.....	16
3.4	Laser Intensity And The Electric Field On Axis As A Function Of Time At Resonance.....	17
3.5	Longitudinal Electric Field Seen By An Electron At Resonance.....	19
3.6	Trajectory-Averaged Electric Field And Laser Intensity Versus The Injection Time At Resonance.....	20
3.7	The Phase Slippage Versus The Injection Time.....	22
3.8	Snapshot Of The Longitudinal Electric Field Off Resonance At $n=7 \times n_{res}$	25
3.9	Normalization Of The Electric Field As Output From TurboWAVE	27
3.10	Laser Intensity And The Electric Field On Axis As A Function Of Time Off Resonance At $n=7 \times n_{res}$	28
3.11	Wave Amplitude And Longitudinal Electric Field Versus Normalized Plasma Density For 1-D And 2-D Waves.....	30
3.12	Phase Velocity Of The Plasma Wave Off Resonance At $n=7 \times n_{res}$	32

2.	Longitudinal Electric Field Seen By An Electron	
	Off Resonance At $n=7 \times n_{res}$	32
3.14	Trajectory-Averaged Electric Field And Laser Intensity	
	Versus The Injection Time Off Resonance At $n=7 \times n_{res}$	33
4.1	Schematic Of The Neptune Laser System.....	36
4.2	10.6 And 10.3 μm Pulse Trains From The Regenerative Amplifier.....	41
4.3	10.6 And 10.3 μm Line Ratio From The Regenerative Amplifier.....	42
4.4	Single Pulse From The Regenerative Amplifier.....	43
4.5	Streak Of The Single Pulse From The Regenerative Amplifier.....	44
4.6	Schematic Of The Neptune Experimental Area.....	47
5.1	Plasma Density From The SRS Measurements.....	55
5.2	Collinear Thomson Scattering Experimental Setup.....	59
5.3	Spectral Properties Of The Etalon.....	62
5.4	Stray Light Measurements With The Filtering Grating.....	66
5.5	Stretching Of A Laser Pulse On A Grating.....	70
5.6	White Light Characterization Of The Collinear TS Optical Filter.....	72
6.1	F/3 Thomson Scattering Spectra At Resonance.....	76
6.2	F/3 Thomson Scattering Spectra Off Resonance.....	78
6.3	Wave Amplitude From The F/3 Thomson Scattering.....	79
6.4	Wave Amplitude Comparison, Experiment Versus Simulations.....	82
6.5	Streak Of The Second TS Harmonic.....	83
6.6	Temporal Lineout Of The Second TS Harmonic.....	84

6.7	Snapshot Of The Transverse Electric Fields In 2-D Simulation.....	87
6.8	F/18 Thomson Scattering Spectra At And Off Resonance.....	90
6.9	Single-shot spectrum of the f/18 accelerated electron.....	92
A.1	Interaction Geometry Between A Free Electron And A EM Wave.....	97
B.1	Experimental Setup For Producing Picosecond CO ₂ Laser Pulses Using The Optical Kerr Effect.....	104
B.2	Temporal Dynamics Of The 1- μ m Pump And 10- μ m Probe Pulses.....	105
B.3	Streaks Of The Switched-Out Pulses.....	109
B.4	Picture Of The Kerr-Switch Portable Apparatus.....	111
B.5	Delay Of The CO ₂ Pulses In The Large Aperture Amplifier.....	115
C.1	90-Degree Thomson Scattering Geometry	118
C.2	Schematic Of The 90-Degree Thomson Scattering Experimental Setup.....	120
C.3	F/3 90-Degree Thomson Scattering Spectra	121
C.4	F/18 90-Degree Thomson Scattering Spectra	123
C.5	F/3 and F/18 90-Degree Thomson Scattering Spectra	124
D.1	Maximum Longitudinal Electric Field Versus The Normalized Vector Potential Off Resonance At $n=7 \times n_{res}$	128
D.2	Plasma Channel Formation Through Relativistic Self-Focusing.....	130
D.3	Longitudinal Electric Field In The Plasma Channel.....	131

List Of Tables

I. Parameters Of The Etalon.....	63
II. Parameters Of The Filtering Grating.....	68

ACKNOWLEDGEMENTS

First, I would like to thank my advisor, Prof. Chan Joshi, for the chance he gave me to use the latest technology available in Neptune Laboratory to pursue various research projects. His guidance and his help contributed significantly to the success of these projects. Second, I am indebted to Dr. Sergei Tochitsky and Dr. Ritesh Narang for their suggestions, ideas and constant help with the experimental program in the Neptune laboratory. Many thanks go to Dr. Chris Clayton and Ken Marsh for their support with the simulations and experiments and to Prof. Warren Mori for his help with the theoretical issues. Thanks are also due to Pietro Musumeci for providing the electron beam and to Dr. Dan Gordon for his help with the TurboWAVE code. Finally, I would like to thank Maria Guerrero for her assistance with any student-related matters.

VITA

January 31, 1970 Born, Slanic-Prahova, Romania

1994 B. S., Physics, Bucharest University, Romania

1999 M.S., Electrical Engineering, University of California,
Los Angeles

1996-2003 Graduate Student Researcher, Electrical Engineering
Department, University of California, Los Angeles

PUBLICATIONS

S. Ya. Tochitsky, R. Narang, C. Filip, C. E. Clayton, K. A. Marsh, and C. Joshi,
“Generation of 160-ps terawatt-power CO₂ laser pulses,” *Opt. Lett.* **24**, 1717
(1999).

S. Ya. Tochitsky, R. Narang, C. Filip, B. Blue, C. E. Clayton, K. A. Marsh, and
C. Joshi, “Amplification of two-wavelength CO₂ laser pulses to terawatt level,”
Proceed. LASERS’99, December 13-16, Quebec, STS press McLean, VA, 2000,
p. 265-272.

C. Filip, K. Sanders, S. Ya. Tochitsky, and C. Joshi, "All-Optical THz modulation using a two-frequency pump laser pulse," Program of the OSA Annual Meeting and Exhibit, October 22-26, 2000, Providence, RI., p. 125.

S. Ya. Tochitsky, C. Filip, R. Narang, C. E. Clayton, K. A. Marsh, and C. Joshi, "Generation of 40-ps, "Terawatt 10- μ m Pulses Using Self-Phase Modulation in Plasma", in *Digest of Conference on Lasers and Electro-Optics* (Optical Society of America, Washington, D.C., 2001), pp. 159-160.

S. Ya. Tochitsky, C. Filip, R. Narang, C. E. Clayton, K. A. Marsh, and C. Joshi, "Efficient shortening of self-chirped picosecond pulses in a high-power CO₂ amplifier," *Opt. Lett.*, **26**, no.11, (2001) p.813-15.

R. Narang, C. Filip, S. Ya. Tochitsky, D. Gordon, C. E. Clayton, K. A. Marsh, and C. Joshi, "Characteristics of plasmas produced by a double beat wave interaction in the Neptune facility at UCLA," Particle Accelerator Conference, Chicago, June 18-22 2001.

C. V. Filip, R. Narang, S. Ya. Tochitsky, C. E. Clayton, K. A. Marsh, and C. Joshi, "Exact forward scattering from a relativistic plasma wave induced by the beatwave technique," *Bull. American Phys. Soc.* **46**, no.8, 90 (2001).

C. V. Filip, R. Narang, S. Ya. Tochitsky, C. E. Clayton, K. A. Marsh, and C. Joshi, "Non-resonant excitation of relativistic plasma waves using a two-wavelength TW CO₂ laser pulse," in *Digest of Conference on Lasers and Electro-Optics* (Optical Society of America, Washington, D.C., 2002), pp. 185-186.

C. V. Filip, R. Narang, S. Ya. Tochitsky, C. E. Clayton and C. Joshi, "Optical Kerr switching technique for the production of a picosecond, multi-wavelength CO₂ laser pulse," *Applied Optics* **41**, 3743-3747 (2002).

C. V. Filip, S. Ya. Tochitsky, R. Narang, C. E. Clayton, K. A. Marsh and C. Joshi, "Interpretation of Resonant and Non-Resonant Beat-Wave Excitation: Experiments and Simulations," AIP Conference Proceedings, vol. **647** Advanced Accelerator Concepts, 10th Workshop, Mandalay Beach, CA, 770-785 (2002).

C. V. Filip, S. Ya. Tochitsky, R. Narang, C. E. Clayton, K. A. Marsh and C. Joshi, "Non-resonant beat-wave excitation of relativistic plasma waves," *Bull. American Phys. Soc.* **47**, no.9, 317 (2002).

C. V. Filip, S. Ya. Tochitsky, R. Narang, C. E. Clayton, K. A. Marsh and C. Joshi, "Collinear Thomson scattering diagnostic system for the detection of

relativistic waves in low-density plasmas," *Rev. Sci. Instr.* **74**, 3576-3578
(2003).

C. V. Filip, C. E. Clayton., S. Ya. Tochitsky, R. Narang, P. Musumeci, R. Yoder, K. A.
Marsh, J. B. Rosenzweig, C. Pellegrini and C. Joshi, "Non-resonant beat-wave
excitation of constant phase-velocity, relativistic plasma waves," submitted to *Phys.*
Rev. E.

ABSTRACT OF THE DISSERTATION

Resonant And Non-Resonant Beat-Wave Excitation Of Relativistic Plasma Waves

by

Catalin Filip

Doctor of Philosophy in Electrical Engineering

University of California, Los Angeles, 2003

Professor Chan Joshi, Chair

The phase relationship between a beat-wave excited relativistic plasma wave and its laser pulse driver is important for the phase-locked acceleration of externally injected electrons. This relationship is studied using 2-D particle-in-cell simulations for both the resonant and non-resonant waves excited in a non-uniform plasma whose density is a time and space-varying quantity due to the slow ponderomotive expulsion of the plasma electrons by the laser pulse. It is found that the waves excited at the resonant density get dephased with respect to the beat pattern of the laser pulse. Therefore, externally injected electrons could interact with both accelerating and decelerating fields of the plasma wave, resulting in a decrease in the overall energy gain. Furthermore, the dynamics of this dephasing is highly sensitive of the initial plasma density and laser pulse parameters, as it is expected from an oscillator being driven just slightly off resonance. As opposed to the resonant case, the accelerating electric fields associated

with the extremely non-resonant plasmons are always in phase with the beat-pattern of the laser pulse, regardless of the variations in the plasma density. Although the normalized amplitude of the oscillation is small, the longitudinal electric field of such a wave can still be substantial if the plasma density is much higher than the resonant density. The excitation of such non-resonant relativistic plasma waves by a TW CO₂ laser pulse is shown to be possible for plasma densities as high as 12 times the resonant density. The density fluctuations and the fields associated with these waves are measured experimentally with a novel collinear Thomson scattering diagnostic system and by the energy change of the injected electrons, respectively.

Chapter 1

Introduction

Undeniably, the most widespread application of a beam of charged particles is in the domestic TV set. Here, a beam of electrons from a cathode ray tube generates light by hitting a matrix of phosphorescent pixels. The use of charged particle beams is not though limited to this example. Many more applications could be found in scientific research, industry, medicine, and even in space where artificial satellites are propelled by ion motors that eject a beam of heavy ions and electrons.

Understanding of physics and the structure of matter at the subatomic level is one of the uses of charged particles beams in scientific research. Particle accelerators and storage rings have contributed greatly to our understanding of the physical world. New types of particles -e.g., positrons, mesons, etc.- have been copiously produced from the interaction of highly relativistic electron beams with matter. These beams are of great importance to various research fields like high-energy, nuclear and theoretical physics. The higher the energy of the charged particles, the wider is the spectrum of potential breakthrough discoveries.

The production of highly relativistic electrons in the laboratory is based on the availability of ultra-high, coherent accelerating electric fields that interact with particles over significant distances. Since plasmas can sustain very high space-charge induced electric fields and laser pulses can generate such relativistically-moving space-charge perturbations in a plasma, it is expected that a laser-plasma combination could provide the needed acceleration. Since this idea was theoretically presented[1], numerous experiments proved the validity of this concept[2].

One way to generate relativistically moving electric fields in a plasma is by exciting a plasma wave using an intense, two-frequency laser pulse (ω_1 and ω_2), in, what is known as a plasma beat-wave accelerator (PBWA)[3]. The action of the ponderomotive force of the beat pattern of the laser pulse on the plasma electrons creates a space-charge density perturbation or a wave in the plasma that has a phase velocity very close to that of the speed of light. Chapter 2 presents a simple picture of the beat-wave excitation process of a relativistic plasma wave (RPW). The motion of a free electron in the field of a constant-amplitude, plane electromagnetic wave is first analyzed. The results are further used to describe the action of the ponderomotive force on the plasma electrons and the subsequent excitation of the plasma wave.

For many applications of high-energy particles one needs a nearly mono-energetic beam. To obtain mono-energetic acceleration, the externally injected relativistic electrons are tightly (less a tenth of a plasma wavelength) pre-bunched with the same periodicity as the laser beat pattern that is also used to excite the RPWs[4,5]. In the ideal case, it is then possible to maintain the phase synchronism between the injected

electrons and the accelerating structure. Successful acceleration of phase-locked electrons, in which the RPW has typically a sub-millimeter wavelength, will depend on four factors: ability to pre-bunch, ability to load the pre-bunched electrons within the acceptance of the RPW structure, control of the experimental time (<100 fs) and space (<50 μm) jitter and control of the phase jitter introduced by the RPW itself. This last factor can be a serious problem in the resonant excitation of RPWs using the laser beat-wave technique. Computer simulations are used in Chapter 3 to model the excitation process of the RPWs because no analytical treatment has been developed for a two-dimensional (2-D) or a 3-D system. Initially, the phase relationship between the plasmon and the driver is followed for the resonant case, when the beat frequency in the plasma, $\Delta\omega=\omega_1-\omega_2$, is equal to the plasma frequency, ω_p . The results show that, transverse and longitudinal plasma inhomogeneities, relativistic saturation of the plasma wave near resonant densities, small deviations from the exact resonance condition in an otherwise uniform plasma, and fluctuations in the laser intensity and rise time, can all dephase the beat wave driver and therefore the pre-bunched electrons with respect to the RPW. In continuation, Chapter 3 describes a possible solution to this issue in which the RPW is non-resonantly excited at plasma densities much greater than the resonant density, $n \gg n_{\text{res}}$. The 2-D particle-in-cell (PIC) computer simulations show that, as opposed to the resonant case, the non-resonantly excited plasmons are similarly always in phase with the beat pattern of the laser pulse. Although the normalized amplitude of the oscillation is smaller, the longitudinal electric field of such a wave can still be substantial if the plasma density is much higher than the resonant density. The results of

Chapter 3 indicate that non-resonantly excited RPWs may be suitable for phase-locked injection in the second-generation PBWA experiments, where the goal is to demonstrate a high-gradient, mono-energetic electron acceleration[2].

Experimentally, a TW CO₂ laser pulse is used to simultaneously produce the plasma and excite the RPWs. The two-frequency pulse is produced by a laser system (described in Chapter 4) that represents a step forward in the laser technology because: (a) it uses an active method to produce and control the two-frequency picosecond pulses, (b) a novel pulse-shortening technique is used in combination with a specially-designed pre-amplifier to finally achieve pulses as short as 40 ps at a TW level of power. The output of this laser system is used to excite both resonant and non-resonant waves in plasmas with densities up to $12 \times n_{\text{res}}$. Moreover, these waves, excited at relatively low plasma densities, from $2 \times 10^{15} \text{ cm}^{-3}$ to 10^{17} cm^{-3} , are characterized using a collinear Thomson scattering (TS) technique whose novelty is reflected in the high-quality notch optical filter that is used to analyze the scattered light, see Chapter 5. The measurements show that the density perturbation δn of the non-resonant waves is significant, on the order of the δn of the resonant waves, as it is actually shown by the simulation results. The simulations also predict significant values for the electric fields that are associated with the RPWs. This information is confirmed in Chapter 6 from the electron injection experiments from the spectrum of the accelerated electrons. The capability of the plasma waves to accelerate phase-locked electrons, as it is studied in the simulations, is not explored here since the injected electrons cover all phases of the plasma wave. With

the advent of the production of shorter electron bunches, such an experimental confirmation of the results from computer modeling could be obtained.

The Appendices contain other data or descriptions of experimental devices that were indirectly used in the study, and, are, therefore, presented in appendices. This information will be helpful to the reader in understanding various results described in the thesis. Appendix A contains the set of equations used to plot the trajectory of an electron in the field of a constant-amplitude electromagnetic wave. Appendix B focuses on the applications of the optical Kerr effect to produce and measure 10- μm pulses. Appendix C describes the method used to detect non-relativistic plasma waves using 90° Thomson scattering. The results shown in this appendix are used to precisely determine the plasma density in the experimental measurements. For future projects, Appendix D elaborates on the possibility of using the self-focusing effect to enhance the amplitude of the non-resonant RPWs.

Chapter 2

Introduction To Beat-Wave Excitation Of Collective Motion Of The Plasma electrons

2.1 The Ponderomotive Force

The understanding of many nonlinear phenomena in the field of laser-plasma interactions lies in the study of the ponderomotive force that acts on the plasma electrons. This force is associated with the radiation pressure that a light wave exerts on a charged particle. Generally, this pressure and the ponderomotive force have very small values, becoming important only when associated with powerful laser pulses. The idea of the ponderomotive force and pressure of radiation can be easily understood if we first consider the simple case of the motion of a free electron in the field of a linearly-polarized, plane electromagnetic (EM) wave. The equation of motion is:

$$\frac{d\mathbf{p}}{dt} = -e(\mathbf{E} + \mathbf{v} \times \mathbf{B}), \quad (2.1)$$

where \mathbf{p} is the momentum of the electron and \mathbf{E} and \mathbf{B} are the intensities of the electric and magnetic fields associated with the EM wave. The motion of the electron has two components; one that is oscillatory in the direction of \mathbf{E} , and another that distorts the orbit due to the second-order $\mathbf{v} \times \mathbf{B}$ term in Eq. 2.1. Without this term the electron would quiver only in the direction of \mathbf{E} , having just a simple oscillatory motion along the axis defined by the electric field. In reality the electron motion is slightly more complex[6,7]. To study this motion we consider a Cartesian system of coordinates with the electron initially at rest in the origin. The EM wave that propagates in the x-direction has \mathbf{E} along the y-axis and \mathbf{B} along the z-axis, as it is shown in the Appendix A in Fig. A.1. To be illustrative for the experiments that will be presented later in this dissertation, the case of a EM wave of a 10- μm wavelength and an intensity given by the normalized vector potential (defined in Eq. A.18) with two different values, $a_{\text{max}}=0.1$ and $a_{\text{max}}=0.3$, is considered. The trajectory of the electron is given by the formulas in Eqs. A.29 that are derived in the Appendix A using Maxell's equations and the equation of motion for an arbitrary a_{max} . Figures 2.1 (a) and 2.1 (b) show the trajectories of the electron, y versus x, for the two values of a_{max} with $z=0$ at all times since there is no force along the z-axis acting on the electron.

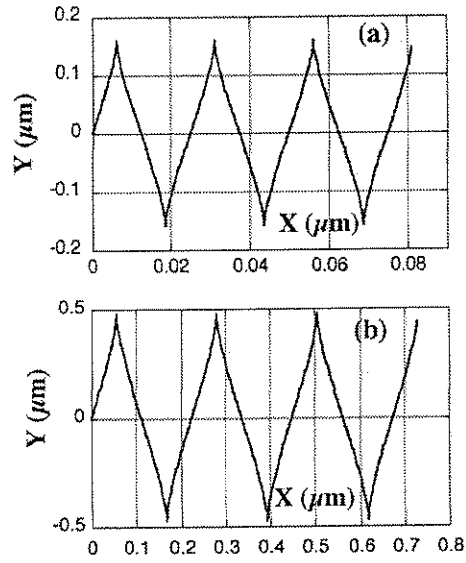


Fig. 2.1. Trajectories, y vs. x , of a free electron (initially at rest) interacting with a 10- μm plane EM wave with a normalized vector potential of $a_{\text{max}}=0.1$ (a), and $a_{\text{max}}=0.3$ (b).

Over a period of time of slightly more than 3 cycles of oscillation for the EM wave, the electron “drifts” approximately 0.08 μm in the direction of \mathbf{k} from its initial position $x=0$ for the $a_{\text{max}}=0.1$ case, see Fig. 2.1 (a). Similarly, if $a_{\text{max}}=0.3$, see Fig. 2.1 (b), the electron moves in the \mathbf{k} direction $\sim 0.72 \mu\text{m}$. Actually, from Appendix A, Eq. A.19, it can be determined that the time-averaged momentum p_x of the electron in the x -direction is proportional to a_{max}^2 . Therefore, the stronger the EM wave, the larger the displacement on the x -axis over the same period of time. This fact becomes important in a plasma where electrons from one region in space could drift into another region under the influence of a strong laser pulse whose electric field has a spatial dependence. This phenomenon is sketched in Fig. 2.2 that shows the beat-pattern of the electric field of a two-frequency laser pulse propagating through a plasma. The plasma electrons are pushed in the direction of the wave vector \mathbf{k} . The electrons in region A drift a longer

distance than those in region B due to a larger electric field of the laser pulse. The plasma electrons are therefore bunched in the regions with lower laser pulse intensity and a density distribution δn is created in the plasma as it is schematically represented in Fig.2.2 by the thick black line. Thus a plasma beat wave is being formed.

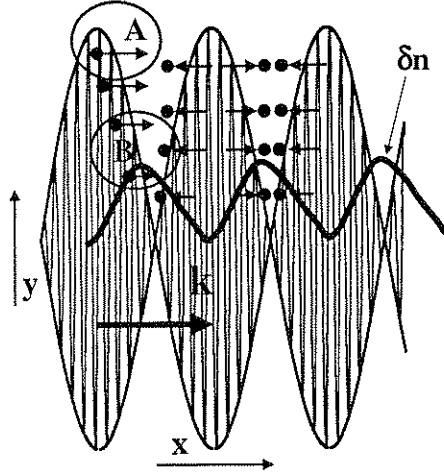


Fig. 2.2. Representation of the electron bunching as a result of the action of the ponderomotive force of a two-frequency laser pulse in a plasma. Larger electron drifts in zone A than in zone B groups the electrons in the regions with smaller intensity of the laser pulse thus creating a density perturbation.

A precise expression of the ponderomotive force is given in [8] for the motion of a free electron in the field of a EM wave that has an electric field:

$$\mathbf{E} = \mathbf{E}_s(\mathbf{r}) \cos(\omega t) \quad (2.2)$$

Here, $\mathbf{E}_s(\mathbf{r})$ represents the maximum value of the electric field that has a spatial dependence. The formula of the ponderomotive force acting on one electron is [8]:

$$f_{pond} = -\frac{1}{4} \frac{e^2}{m\omega^2} \nabla E_s^2, \quad (2.3)$$

where ω is the frequency of the laser pulse and m and e are the mass and the charge of the electron, respectively.

2.2 Beat-Wave Excitation Of Relativistic Plasma Waves

Equation 2.3 can be used to compute the ponderomotive force exerted on the plasma electrons by a laser pulse of an arbitrary shape and length propagating through that plasma. This equation is explicitly used in particle-in-cell (PIC) simulation codes to model the excitation of various plasma waves[9].

As mentioned before, for an efficient beat wave excitation of RPWs, intense laser beams have to be used. Experimentally, these beams are tightly focussed to achieve extremely high intensities, up to 10^{18} W/cm². In such a case, the ponderomotive force of a beat EM wave will develop a transverse component as well as a longitudinal one. Therefore, 2-D (two-dimensional) and 3-D PIC modeling of the beat wave excitation process using Eq. 2.3 becomes important especially since no multi-dimensional analytical solutions (other than 1-D) exist.

The excitation process of a RPW when $\Delta\omega=\omega_p$ was investigated by Rosenbluth and Liu in 1972 using Lagrangian fluid equations for a cold, homogeneous plasma[10]. Then it was shown that the amplitude $\epsilon=\delta n/n$ of the plasma wave initially grows linearly in time:

$$\epsilon=F t, \tag{2.4}$$

where the growth rate $F=a_1a_2\omega_p/4$ (a_1 and a_2 are the normalized vector potentials corresponding to the ω_1 and ω_2 frequencies of the laser pulse, respectively). Whilst the amplitude of the RPW increases, the driving force of the laser beat pattern and the relativistic plasmon begin to go out-of-phase. The RPW gradually acquires an amplitude-dependent frequency shift that ultimately limits the maximum amplitude that the wave could achieve to:

$$\epsilon_{\text{sat}}=(16/3a_1a_2)^{1/3} \quad (2.5)$$

At saturation, the excitation process actually becomes “anti-resonant” with a $\pi/2$ shift between the driver and the RPW. At this point, the amplitude of the RPW starts to decrease as the energy of the wave begins to flow back into the laser pulse. This phenomenon was investigated by Tang et al.[11] who proposed to compensate for this “relativistic” saturation by employing a density detuning. In addition, the study pointed out the importance of having a consistent and exact value for the plasma density. For example, a 2% difference between $\Delta\omega$ and ω_p , can lower ϵ_{sat} ~ 5 times while the RPW saturates ~ 2 times faster. Therefore, if fluctuation of this level exist between $\Delta\omega$ and ω_p , an externally injected relativistic electron could find itself in the decelerating field of the plasma wave and it could begin to lose energy, particularly if there are density inhomogeneities in the plasma. Other analytical and numerical 1-D studies have also investigated the critical issue of RPW dephasing with[12] and without density inhomogeneities[13,14]. In the next chapter we analyze the electron-plasmon interaction in space and time *during* the acceleration process in 2-D, using the PIC code TurboWAVE[9].

Chapter 3

Simulations

3.1 Resonant Excitation

We use the code TurboWAVE[9] that includes ionization of gas and mobile ions to model the growth and saturation of the beat wave-driven RPW and in particular to follow the phase relationship between the plasmon and the driver. The simulations are set to trace in space (2-D) and time the intensity of the laser pulse, the ion and electron density, and the electric fields associated with the density perturbations. Figure 3.1 shows a snapshot of the beat pattern (intensity) of the laser pulse close to the moment when its peak reaches the center of the simulation box. The 50-ps (FWHM), two-frequency pulse with $\omega_1, \omega_2/\omega_p \sim 30$ and $a_1 = a_2 = 0.3$ (maximum values) propagates in hydrogen from left to right. For this laser pulse the normalized intensity at the focus can be written as:

$$a^2(t) = [a_1(t)\cos(\omega_1 t) + a_2(t)\cos(\omega_2 t)]^2 \quad (3.1)$$

If $a_1 = a_2 = a_0$, then Eq. 3.1 simplifies as:

$$a^2(t) = 4a_0^2(t)\cos^2\left(\frac{\Delta\omega t}{2}\right), \quad (3.2)$$

where we dropped the high-frequency component. Therefore, the maximum value of the normalized intensity at the focus (see Fig. 3.1) is $4 \times (0.3)^2 = 0.36$.

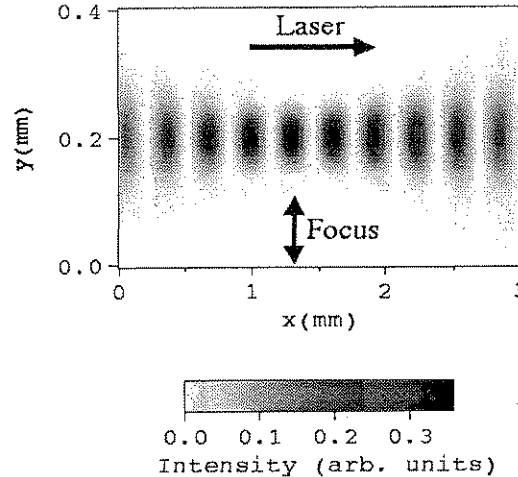


FIG. 3.1: Snapshot of the normalized intensity (a^2) of the two-frequency laser pulse at ~ 53 ps after the front of the pulse, moving from left to right, reached the center of the simulation box; y and x are the transverse and longitudinal directions, respectively. The vertical arrow indicates the position of the “vacuum” focus. The initial plasma density is $n = 1.3 \times n_{\text{res}}$.

The beat period in Fig. 3.1 is approximately $330 \mu\text{m}$ (1.1 ps). This beat period is maintained constant, equal to $330 \mu\text{m}$, for all simulations, both at resonance and away from resonance. The same procedure is applied in the experiments (described later) where the relative change between $\Delta\omega$ and ω_p is done by adjusting the plasma density.

We first illustrate the dephasing between the plasmon and the driver caused by the plasma density inhomogeneities introduced by the transverse component of the ponderomotive force of the laser pulse. This is done by choosing the ratio of the plasma wavelength to the spot size of the laser beam to be 6. For a CO_2 laser, used in the experiments described in the next chapter, this corresponds to a spot size w_0 of $50 \mu\text{m}$. The hydrogen gas is tunnel-ionized and plasma is formed with a density initially above

resonance, $n=1.3 \times n_{\text{res}}$. The plasma density decreases in the focal region with a maximum $dn/dt = -0.8\% \times n/ps$ due to the transverse ponderomotive force of the laser pulse which expels the plasma electrons. Therefore, n is a function of the longitudinal (x) and transverse (y) positions and time, $n=n(x, y, t)$. To illustrate how the variations in the plasma density affect the saturation process of the RPW, Fig. 3.2 (a) shows a snapshot of the longitudinal electric field E_x associated with the RPW. Figure 3.2 (b) shows a horizontal lineout through the center of Fig. 3.2 (a), which is also the axis of symmetry of the laser beam.

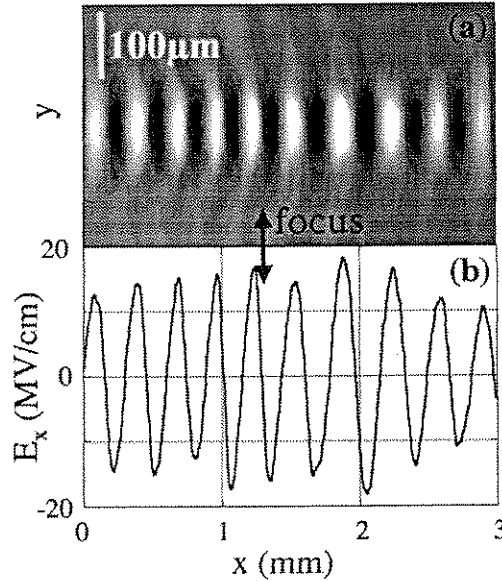


FIG. 3.2: (a) Snapshot of the longitudinal electric field E_x associated with the RPW at 53 ps after the front of the pump pulse, moving from left to right, reached the center of the simulation box; y and x are the transverse and longitudinal directions, respectively. The initial plasma density is $n=1.3 \times n_{\text{res}}$. (b) Horizontal lineout through (a). The black arrow indicates the location of the vacuum focus.

Following ionization, the plasma density slowly begins to decrease in the focal region as a result of the ponderomotive blowout. The RPW grows faster here than upstream

and downstream of the best focus, especially when the plasma density approaches n_{res} . The phase velocity of the wave begins to drop below c , reaching a minimum when ϵ is close to its maximum value. In other words, in the focal region, the wave is slowing down. This effect is visible in Fig. 3.2 (a) and Fig. 3.2 (b) around $x=1$ mm, where the wavefronts of the plasma wave are “squeezed” compared to the region downstream of the focus. The snapshot is taken at $t=53$ ps after the front of laser pulse reached the center of the simulation box. To better illustrate this effect and to quantify the evolution of the phase velocity v_{ph} , a crest of the RPW which enters the simulation box on axis at $x=0$ mm and $t=47.5$ ps is followed in space and time. The dots in Fig. 3.3 (a) show the dependence of the position of the crest versus time, $x=x(t)$. The solid straight line is the speed-of-light trajectory that is followed by the beat pattern of the laser pulse which moves with a nearly constant group velocity $v_g \sim 0.9994c$ during this simulation. The departure of the dots from the straight line illustrates the dephasing of the RPW with respect to the laser pulse. The instantaneous phase velocity v_{ph} of the RPW is determined by taking the derivative of a curve that best fits the dots in Fig. 3.3 (a). The ratio v_{ph}/v_g is shown in Fig. 3.3 (b). The RPW slows down to $\sim 0.82c$ in the region upstream of focus and “speeds up” to $\sim 1.18c$ downstream of focus. This behavior of the phase velocity of the RPW is due mainly to the longitudinal variations in the plasma density caused by the ponderomotive force of the laser pulse and not to relativistic detuning.

The $x(t)$ dependence shown in Fig. 3.3 (a) by the dotted line is a function of the “injection” time, that is, the time when the crest of the RPW appears at $x=0$ in the simulation box. It is possible to show the position x (on axis) of both the beat pattern of

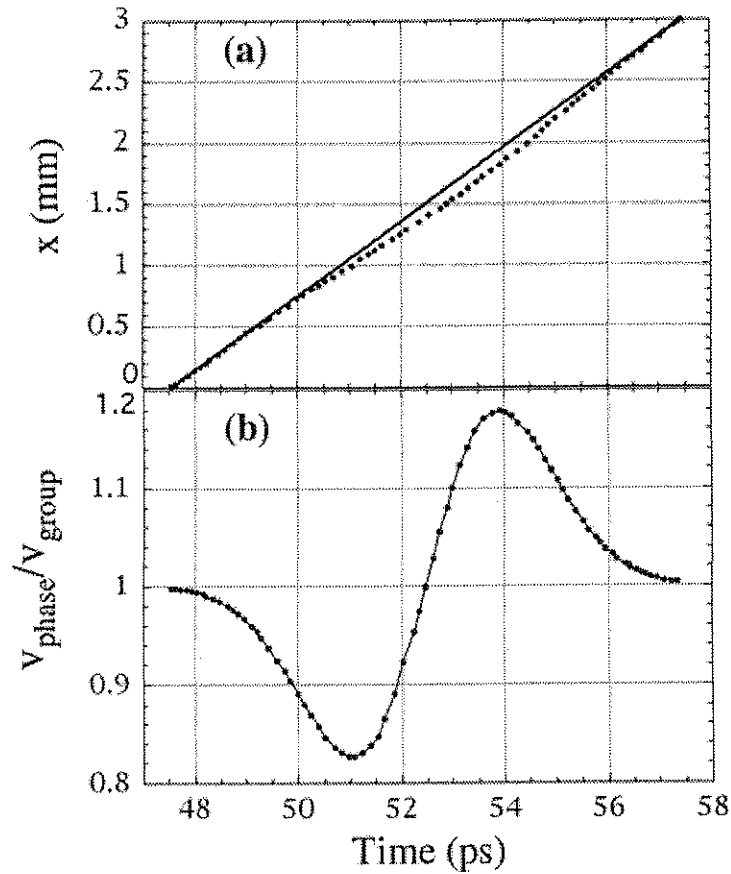


FIG. 3.3: (a) Horizontal position x of a crest of the plasma wave that enters the simulation box at $x=0$ and $t=47.5$ ps versus time (dots) and the speed-of-light trajectory (solid line). The initial plasma density is $n=1.3 \times n_{\text{res}}$. (b) The ratio of the instantaneous phase velocity of the plasma wave to the group velocity of the laser pulse versus time, obtained from (a).

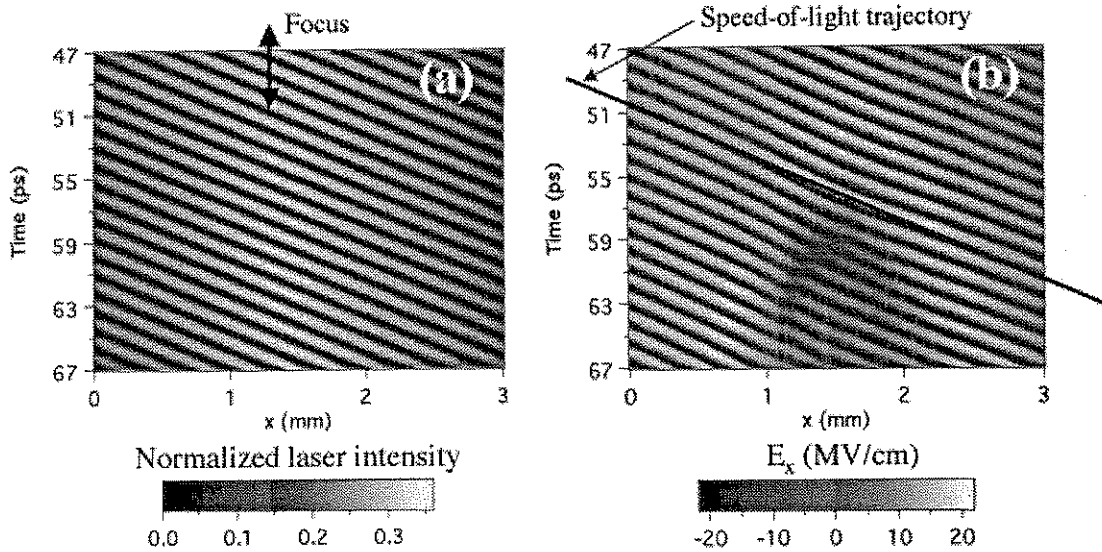


FIG. 3.4: (a) The normalized laser intensity on axis (from $x=0$ mm to $x=3$ mm) as a function of time from $t=47$ ps to $t=67$ ps; the vertical arrow indicates the position of the “vacuum” focus. (b) The longitudinal electric field associated with the plasma wave on axis, also as a function of time; the solid line represents a speed-of-light trajectory. The initial plasma density is $n=1.3 \times n_{\text{res}}$.

the laser pulse and the crests of the RPW at all injection times by recording in a 2-D matrix the information on the x -axis at all simulation steps. Figure 3.4 (a) shows the normalized intensity of the laser pulse (the beat pattern) on the axis, for all times starting with $t=47$ ps and ending with $t=67$ ps. Before $t=47$ ps, the pulse already ionized the hydrogen gas and it propagates now through the plasma with $v_g \sim 0.9994c$. The fringes in this figure represent the motion of the beats of the laser pulse in time. These fringes are straight as opposed to those corresponding to the crests of the longitudinal electric field E_x of the RPW shown in Fig. 3.4 (b) which curve around the focal plane due to the dephasing phenomenon discussed above. The interval $t=47$ ps to $t=67$ ps was chosen to clearly show: (1) the difference between the spatial evolution of the beat pattern of the laser pulse in comparison with that of the electric field E_x of the RPW and

(2) the gradual dephasing in time of the plasma wave that could not be represented in Fig. 3.3. The solid line in Fig. 3.4 (b) shows a speed-of-light trajectory that is actually followed not only by the beat pattern of the laser pulse but also by the externally injected relativistic electrons that are supposed to “surf” the plasma wave.

The continuous dephasing of the RPW can have a profound influence on such a relativistic electron that is injected at $x=0$ at a particular phase, and initially moving synchronously with it. The maximum spatial separation Δx accumulated between the electron and the RPW can be found from Fig. 3.3 (a) to be $\Delta x \cong 135 \mu\text{m}$, which is close to half of a plasma wavelength. Therefore, it is possible for the electron to interact with both positive and negative fields (see also Fig. 3.4 (b) where the solid line intersects both positive and negative values of E_x). The electric field E_x seen by a “virtual” relativistic electron initially injected on axis at $x=0$ and injection time $t_{inj} \cong 47.5 \text{ ps}$ is shown in Fig. 3.5 (dotted line). Figure 3.5 also shows the longitudinal plasma density profile at the time of the injection (solid line). The electron feels a positive electric field upstream and downstream of the focus, but in the focal region it is significantly decelerated as a result of the rapid dephasing represented in Fig. 3.5. The electric field E_x has a strong dependence not only of the position of the electron, but also of the injection time, t_{inj} , as pointed out in Fig. 3.4.

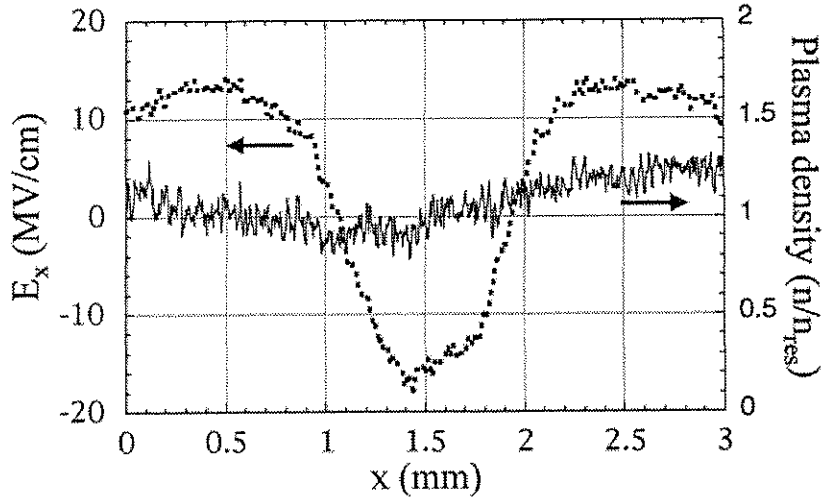


FIG. 3.5: Longitudinal electric field E_x seen by a “virtual”, relativistic electron injected on-axis at $x=0$ and $t_{inj} \cong 47.5$ ps at the speed of light versus its position x in the plasma (left axis, dotted line) for $n=1.3 \times n_{res}$. Axial profile of the plasma density, normalized to n_{res} , at the injection time (right axis, solid line).

To find out what is the influence of the dephasing on the overall energy gain for an electron injected at an arbitrary t_{inj} , we introduce two new quantities, F and G . The quantity F , calculated for each injection time, $F=F(t_{inj})$, is the electric field averaged over a certain interaction length L where the RPWs are driven. This quantity, multiplied by the interaction length, gives the overall energy gain achieved by the electron. In a similar way, G represents the normalized laser intensity that an injected electron would “ride” along with in the plasma, averaged over the same L , for each injection time, $G=G(t_{inj})$. The interaction length L that the average is performed over is taken to be 3 mm. These two “trajectory-averaged” quantities, F and G , are presented in Fig. 3.6 as a function of t_{inj} for a selected time interval that was specifically chosen to show a clear change in the relative phase between F (solid line) and G (dotted line).

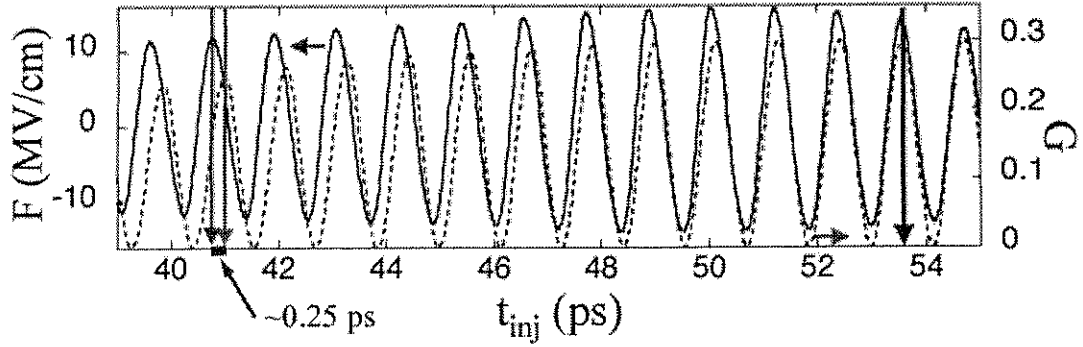


FIG. 3.6: The solid line (left axis) shows the trajectory-averaged electric field F seen by a relativistic electron injected on axis (at $x=0$) versus the injection time, $F=F(t_{inj})$. The dotted line (right axis) shows the trajectory-averaged normalized laser intensity G that the electron is riding along with in the plasma, versus the injection time, $G=G(t_{inj})$. The initial plasma density is $n=1.3 \times n_{res}$. The separation (phase) between the maxima of F and G is changing from -0.25 ps, see the vertical arrows at $t_{inj} \cong 40$ ps, to approximately 0 ps (see the arrow at $t_{inj} \cong 54$ ps).

Over approximately 11 laser beat periods, from $t_{inj} \cong 41$ ps to $t_{inj} \cong 53$ ps, the separation between the maxima of the two quantities, F and G , changes from $\Delta t \cong 0.25$ ps, see vertical arrows in the left side of Fig. 3.6, to $\Delta t \cong 0$ ps (see vertical arrow in the right side of Fig. 3.6). Such a phase shift between F and G could force an externally injected electron phase-locked with G to “miss” the proper injection phase that maximizes F by as much as 25% of a beat period, τ_{beat} . As a result, the electron would see a smaller overall accelerating field, as it is the case presented in Fig. 3.5, where the injected electron, instead of being accelerated with the maximum of $F \cong 15$ MV/cm, sees a much smaller trajectory-averaged accelerating gradient of ~ 4 MV/cm.

The decrease in the overall accelerating field is not the only negative aspect that results from the local dephasing of the RPW. This dephasing can also affect the acceleration of short, multiple bunches (equally spaced with τ_{beat}) of injected electrons that are phase-locked to the beat pattern of the laser pulse. Each bunch will be

accelerated by electric fields with different values because of the gradual dephasing between F and G from bunch to bunch, as it is shown in Fig. 3.6. This will result in a significant spread in the energy gained by these bunches. If one single bunch is to be injected at the proper phase that maximizes the overall accelerating field F, then it is possible to obtain a narrow spread in the energy gained by the electrons for as long as the parameters of the excitation process of the RPW are kept the same, shot after shot. 2-D simulations with small changes (few percent) in the initial plasma density were performed. We compare the simulation results from the run where the initial plasma density is $n=1.3 \times n_{res}$ to a run where the plasma density is $\sim 10\%$ lower, $n=1.13 \times n_{res}$. All other parameters are the same in both cases. The simulation results are summarized in Fig. 3.7 that shows on the left axis, solid line with filled circles, the peak positive values of the quantity F (extracted from graphs similar to the one shown in Fig. 3.6) versus the injection time, t_{inj} . In both situations the maximum trajectory-averaged accelerating field is approximately 16 MV/cm. For the lower density case this value is achieved faster, around $t_{inj}=40$ ps, as the plasma density drops down to n_{res} faster than in the other case. Figure 3.7 also shows the accumulated phase slippage $\Delta\Phi$ between F and G represented by the interrupted line (square dots) on the right axis. The phase slippage was recorded by, first, calculating the temporal separations between all maxima of F and, second, by adding these separations together to obtain the accumulated phase slippage as a function of the injection time, for both density cases.

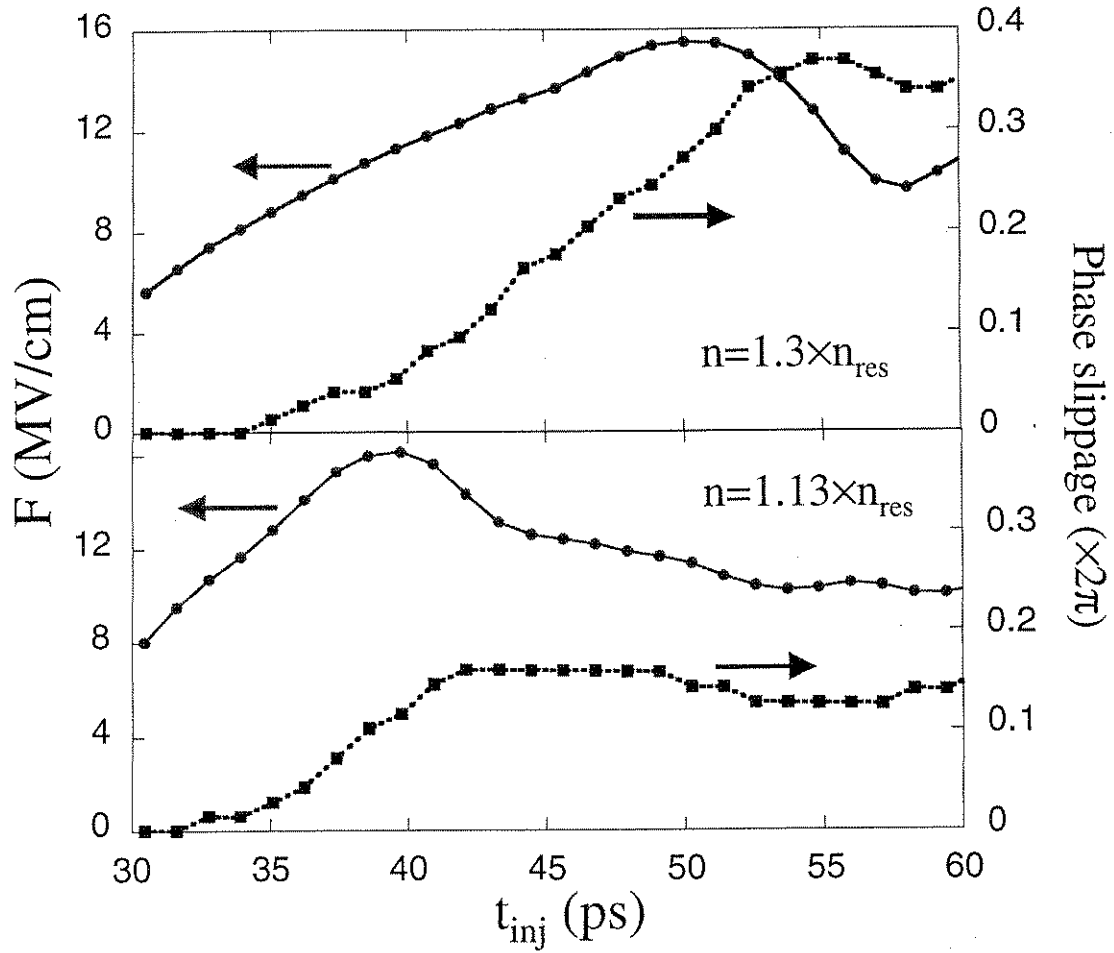


FIG. 3.7: The solid line (filled circles, left axis) shows the maximum values of the trajectory-averaged electric field F . The interrupted line (squares, right axis) shows the accumulated phase slippage between F and G , normalized to the beat period $\tau_{beat}=1.1$ ps (a value of 1 on this axis means a phase slippage of 2π). Top graph is for the $n=1.3n_{res}$ case and the bottom is for the $n=1.13n_{res}$ case.

The phase slippage is normalized to the appropriate number of beat periods $\tau_{beat}=1.1$ ps (or plasma wave buckets) for each t_{inj} . A value of 1 on the right axis in Fig. 3.7 means a phase slippage of 2π or, equivalently, a temporal shift of τ_{beat} . Two important conclusions can be obtained from the evolution of $\Delta\Phi$ in Fig. 3.7: (1) in both density cases the phase slippage increases with the increasing accelerating gradient represented by the maxima of F on the left axis; for the early times the plasma wave is not dephased

with respect to the laser pulse and electric field associated with it is maximum 8 MV/cm, and (2) the accumulated phase slippage is very different for the two cases in discussion (as a function of t_{inj}), $\Delta\Phi$ reaching a maximum of 0.36 for the $n=1.3n_{res}$ case, as opposed to a maximum $\Delta\Phi$ of 0.15 for the $n=1.13n_{res}$ case.

Supposing that the maximum attainable acceleration of $F=16$ MV/cm is targeted in the $n=1.3n_{res}$ case, and the phase slippage $\Delta\Phi\cong 0.3$ is compensated for, if the plasma density decreases for one shot with 10%, the maximum of F will only be ~ 10 MV/cm with an unexpected phase shift $\Delta\Phi\cong 0.3-0.15=0.15$. This phase shift further means that the phase-locked electrons meant to be accelerated with 16 MV/cm will see an accelerating gradient even smaller than 10 MV/cm, probably only 5-6 MV/cm given the significant unexpected $\Delta\Phi$. Note that the accelerating field is approximately zero for an electron bunch that “misses” any maxima of F by $\Delta\Phi=0.25$.

The temporal profile of the dephasing $\Delta\Phi$ between the driver (G) and the RPW (F) changes if different rise times or intensities of the laser pulse are used in the simulations at the same plasma density. Therefore, the acceleration of phase locked electrons is highly sensitive of these parameters, especially the plasma density. In reality, it is difficult to obtain and maintain an uniform, long, high-density plasma shot after shot, due to phenomena such as the ponderomotive blowout, partial and multi-stage ionization, ionization-induced refraction, and density inhomogeneities. In conclusion, in a resonant PBWA, the dephasing between the driver and the plasma wave cannot be easily controlled and it could adversely influence the reproducibility of the electron energy gain.

3.2 Non-Resonant Excitation

Now let us consider the highly non-resonant excitation, $n \gg n_{\text{res}}$ of the RPWs in a PBWA. Such a regime has hitherto not been considered because it is thought to produce only a weak, asymptotic response to the driver of a given strength leading to longitudinal electric fields not of interest to particle acceleration. As an example we show results of simulations that were carried out at a plasma density $n = 7 \times n_{\text{res}}$. All other parameters are the same as the ones mentioned earlier. Forced plasma oscillations are excited by the two-frequency laser pulse. These oscillations represent a RPW that has a phase velocity, v_{ph} , equal to the local group velocity of the laser pulse in the plasma. Note that the higher density changes the effective relativistic Lorentz factor $\gamma_{\text{ph}} \equiv \omega_l / \omega_p$ associated with this RPW compared to that at the exact resonance. Even though the homogeneous response of the plasma might have triggered the onset of the Raman Forward instability, no relativistic waves with a frequency of ω_p were observed in the simulations. Figure 3.8 (a) shows a typical snapshot of the longitudinal (E_x) field associated with the plasma wave. The image is slightly noisier than for the resonant case in Fig. 3.2 due to a smaller number of particles used in the simulations that are carried out at high plasma densities. The wave vector of the plasma wave is Δk , where $\Delta k = k_1 - k_2$ and k_1 and k_2 are the wave vectors of the pump pulse.

Other simulations were performed at different densities with similar results. No nonlinear saturation process has been observed. The E_x field maintains the profile

shown in Fig. 3.8 (a) for as long as the pump pulse of an approximately constant amplitude is present in the plasma. Fig. 3.8 (b) shows a lineout of the E_x along the axis of the laser beam.

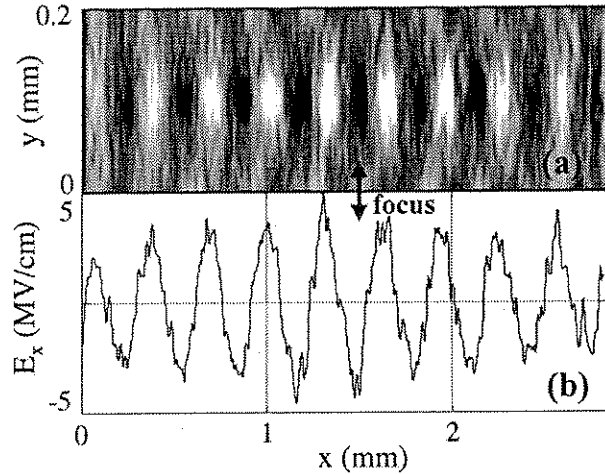


FIG. 3.8: (a) Snapshot of the longitudinal electric field E_x associated with the RPW at 53 ps after the front of the pump pulse, moving from left to right, reached the center of the simulation box; y and x are the transverse and longitudinal directions, respectively. The initial plasma density is $n=7 \times n_{res}$. (b) Horizontal lineout through (a). The black arrow indicates the location of the vacuum focus.

The simulations are performed on a cluster of 3 G4 Apple computers. Usually, 16 particles are placed in a grid of 1024×256 cells with $0.1c/\omega_p$ size per cell. The code is set to run for 10000 steps with $0.1/\omega_p$ time step, which makes the running time to be ~ 48 hours. The frequency difference $\Delta\omega$ is varied compared to ω_p in turboWAVE by adjusting the laser frequencies and keeping the plasma density constant. This is possible because the code does not model any phenomena on the laser cycle time scale and because all the other parameters, like the laser rise time, fall time, etc., are also changing in the input deck. What is important to follow when these changes are done in the input deck of the code are the normalization constants that appear in the output of the code for all the key quantities like the plasma density, electric fields, etc. These

constants, set arbitrarily to some values in the code, were checked against theoretical scaling laws that are valid for any 1-D simulation. For example, when a 1-D simulation is performed at a density $n \gg n_{\text{res}}$, the value of the electric field associated with the RPWs (the longitudinal and transverse electric fields E_x and E_y , respectively, for 2-D) is normalized in the output of the code to the cold wavebreaking limit at density n , $E_{\text{cold at } n}$. The ion and electron density perturbations as output quantities are normalized to the resonant plasma density n_{res} set by the neutral density of the fill gas. The relationship between these quantities and the wave amplitude ε is given by the Poisson's equation:

$$\frac{E/E_{\text{cold at } n}}{\varepsilon} = 0.96\sqrt{n/n_{\text{res}}} \quad (3.3)$$

The code performed 10 runs where the density is varied from $\sim 0.4 n_{\text{res}}$ to $16 n_{\text{res}}$. The 1-D simulation results are presented in Fig. 3.9. Each dot represents the ratio between the normalized longitudinal electric field and the wave amplitude versus the square root of the normalized density for each run. The dotted line is a linear fit for these points and it resembles Eq. 3.3 within the error of determining the exact values for the wave amplitude and the electric field from turboWAVE. It can be concluded that the code accurately models the excitation of RPW in the non-resonant regime and the output can be precisely predicted as quantities expressed in absolute values.

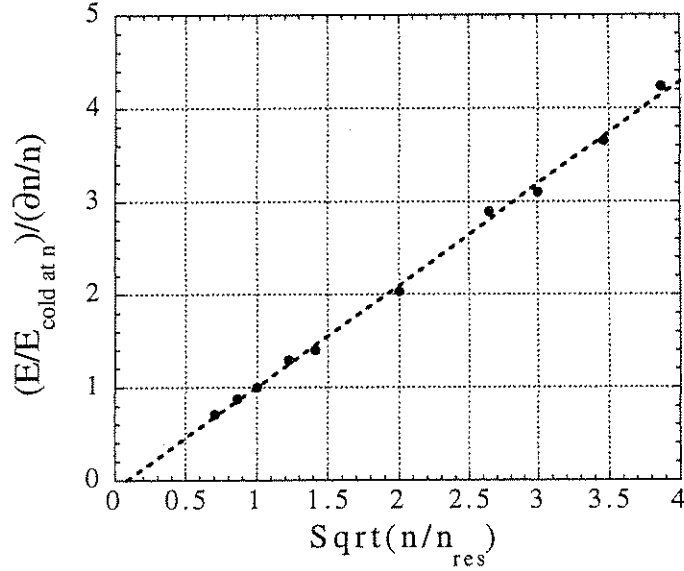


FIG. 3.9: Ratio of normalized longitudinal electric field and wave amplitude versus the square-root of n/n_{res} from the 1-D simulations with turboWAVE (dots); the dashed line represents a linear fit for the data points.

For the non-resonant excitation case at $n=7 \times n_{res}$ the plasma density is large enough to begin affecting the propagation of the laser pulse through the onset of the ionization induced refraction. This can be seen in Fig. 3.10 (a) that shows the evolution in time of the normalized laser intensity on axis and in Fig. 3.10 (b) which represents the longitudinal electric field E_x of the RPW on axis. For the time period between $t=30$ ps and $t=40$ ps, the plasma density created by the first beats of the pulse is high enough to cause strong refraction of the following part of the laser pulse. The energy of the laser pulse on axis is refracted sideways (in the transverse y direction) by the plasma formed at around $x=1$ mm initially upstream of the vacuum focus. Therefore, the intensity of the laser pulse on axis does not reach the maximum value that would otherwise attain in vacuum. The plasma acts as a negative lens, and, the higher the plasma density, the

more difficult it is for the laser pulse to ionize the gas downstream of the vacuum focus. In fact, it takes ~ 12 laser beats to fully ionize the gas present on axis at $x > 2$ mm, see the irregular structure in Fig. 3.10 (b). In spite of the ionization induced refraction, at $t = 45$ ps the plasma is formed over the entire length of the simulation box from $x = 0$ mm to $x = 3$ mm.

The frequency of the plasma wave was determined to be $\Delta\omega$ (at all times) from Fig. 3.10 (b) by taking a vertical lineout. Figure 3.10 (b) also shows that, as opposed to the resonant case in Fig. 3.4 (b), the wavefronts of the non-resonant RPW always move at the nearly constant speed of light even if the ponderomotive force again creates a density depression close to the focal plane.

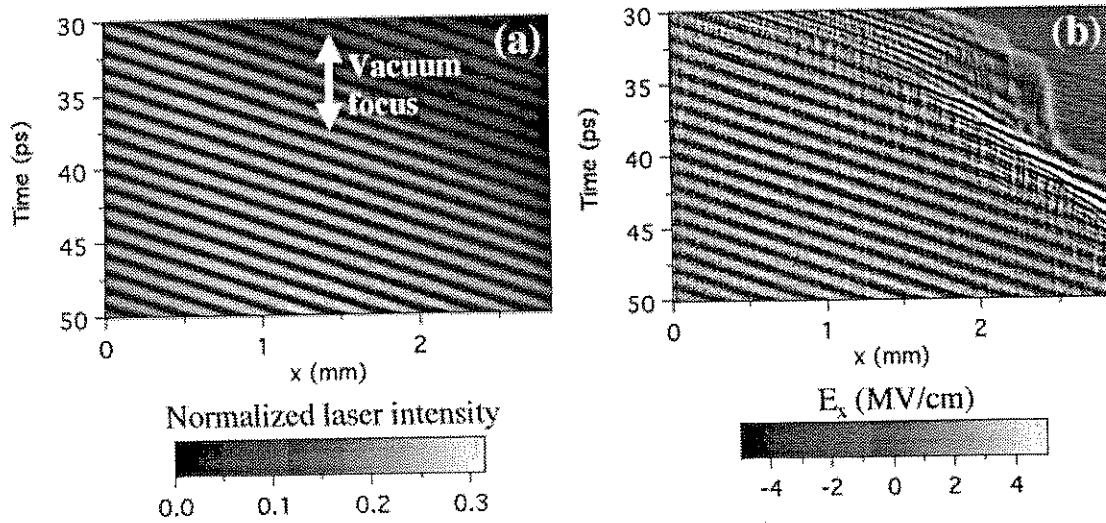


FIG. 3.10: (a) The normalized laser intensity on axis (from $x = 0$ mm to $x = 3$ mm) as a function of time from $t = 30$ ps to $t = 50$ ps; the vertical arrow indicates the position of the “vacuum” focus. (b) The longitudinal electric field associated with the plasma wave on axis, also as a function of time. The initial plasma density is $n = 7 \times n_{res}$.

Even though in this case the wave amplitude $\epsilon = \delta n/n$ is small, $\epsilon \sim 1.8\%$, the maximum local value of E_x , from Fig. 3.8 (b) and Fig. 3.10 (b), is quite high, $E_x = 5$ MV/cm. This is, because, according to Poisson's equation, the electric field is a function of the perturbed density δn and not ϵ . The value of the electric field associated with a 1-D RPW excited at a plasma density equal to n which is different than the resonant density n_{res} , can be expressed as:

$$E_x = 96 \times \frac{dn}{n} \times \frac{n}{n_{res}}, \quad (3.4)$$

where E_x is measured in MV/cm and $\delta n/n = \epsilon$ is the amplitude of the RPW. As an example, in 1-D, a 1% wave excited at $n = 10 \times n_{res}$ has the same accelerating field as a 10% wave at resonance. The 1-D result is not valid for a 2-D (or a 3-D) wave due to the transverse electric fields associated with δn . The exact relationship between E_x and ϵ can only be extracted from the simulation results. We have observed that tightly focussed laser beams drive higher amplitude (than 1-D) waves off-resonance. This can be seen in Fig. 3.11 (a) which shows the maximum amplitude ϵ_{max} of the RPWs obtained from 1-D and 2-D ($w_0 = 50 \mu\text{m}$) simulation results from the PIC code for a range of plasma densities from $0.5 \times n_{res}$ to $14 \times n_{res}$. The ϵ_{max} at resonance, shown in Fig. 3.11 (a) for the 1-D case, is approximately 75%, very close to the 78% value predicted by the 1-D analytical model of Ref. [10]. The 2-D simulations included the formation of the plasma by tunnel ionization of hydrogen and mobile ions. The reason why the 2-D values of ϵ_{max} are higher than the 1-D values is that, with tightly focussed

beams, both the radial and axial oscillations can contribute to the density perturbation δn .

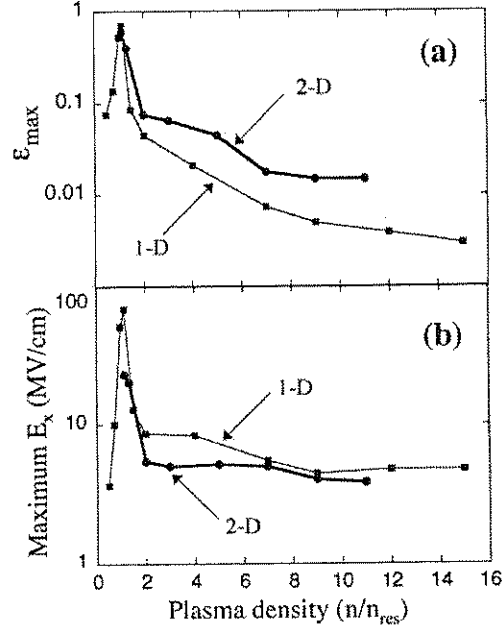


FIG. 3.11: (a) Maximum local amplitudes of the RPWs ϵ_{\max} excited by a 10- μm , 50-ps pulse with normalized vector potentials of $a_1=a_2=0.3$, 1-D (squares, thin line) and 2-D ($w_0=50 \mu\text{m}$, circles, thick line) versus the plasma density normalized to n_{res} . (b) Maximum values of the longitudinal electric fields E_x associated with the RPWs shown in (a).

The PIC simulations can also provide the maximum local value for the longitudinal electric field, E_x , associated with the 1-D and 2-D RPWs whose amplitudes were presented in Fig. 3.11 (a). These values are shown in Fig. 3.11 (b) for the 1-D case (squares), and for the 2-D case (circles). Surprisingly, although the amplitude of the density perturbations in the 2-D simulations are higher than the 1-D simulations, the value of the maximum E_x is the same or somewhat smaller. This is thought to be because of the significant radial component E_y of the electric field associated to the RPWs produced by tightly focussed beams. The maximum E_x for a range of plasma

densities of $2-11 \times n_{\text{res}}$ is ~ 5 MV/cm. Although the 2-D non-resonant E_x is smaller than the peak value of approximately 23 MV/cm at resonance, the non-resonant fields are now insensitive to the exact plasma density and, more important, they are phase-locked with the beat pattern of the laser pulse.

The phase velocity of the RPW excited at $n=7 \times n_{\text{res}}$ can be precisely determined using the same technique as was used in Fig. 3.3, i. e., by following a crest of the E_x associated with the wave in space and time. Figure 3.12 shows the position x of a given crest on axis versus time. The round dots mark the moments when the position of the crest was recorded and the solid line represents the speed-of-light trajectory. As opposed to the resonant case (see Fig. 3.3), there is no measurable difference between the dots and the solid line for the entire length of the plasma. Within the accuracy of the measurement, the instantaneous phase velocity of the wave is constant and is equal to the group velocity of the laser pulse, $v_{\text{ph}} = v_g \cong 0.996c$ at $n=7 \times n_{\text{res}}$. This measurement was performed for other phases (crests) of the plasma wave with the same result, see Fig. 3.10 (b). The electric field E_x that interacts with an externally injected relativistic electron is shown by the dotted line in Fig. 3.13 versus the position of the electron in the plasma. As opposed to the resonant case of Fig. 3.5, the electric field associated with the non-resonant wave does not change polarity at any position x of the injected electron in the plasma. Instead, the profile of the electric field resembles the distribution (profile) of the pump laser pulse. The solid line in Fig. 3.13 shows a snapshot of the inhomogeneous plasma density on axis at the moment of injection, $t \cong 47.5$ ps.

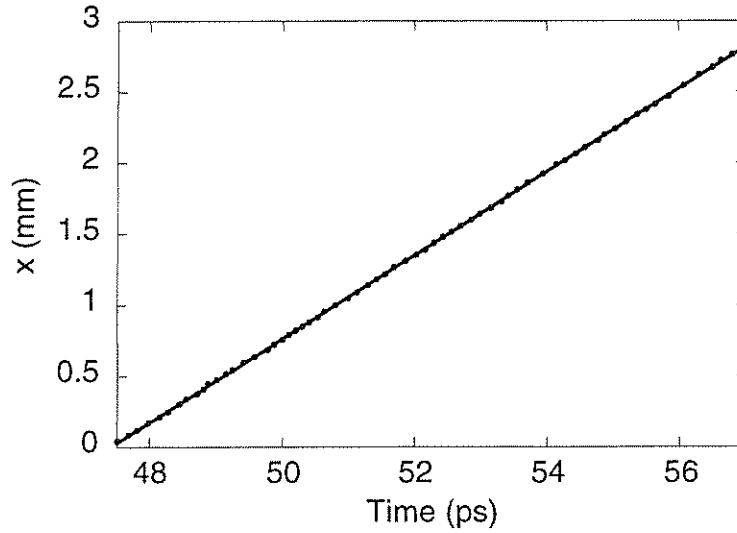


FIG. 3.12: Horizontal position x of a crest of the plasma wave that enters the simulation box at $x=0$ and $t=47.5$ ps versus time (dots) and the speed-of-light trajectory (solid line). The initial plasma density is $n=7 \times n_{\text{res}}$.

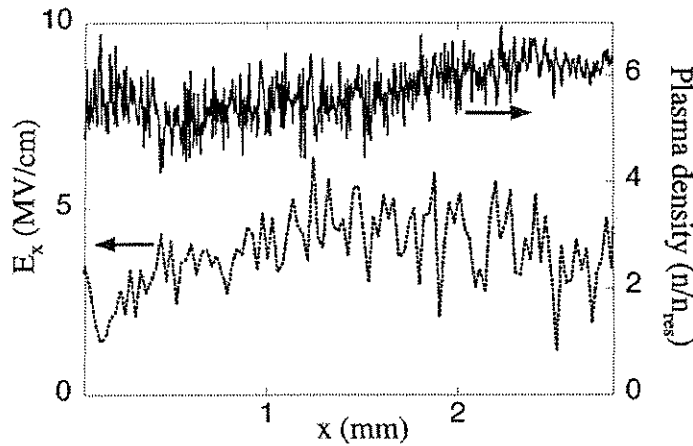


FIG. 3.13: Longitudinal electric field E_x seen by a “virtual”, relativistic electron injected on-axis at $x=0$ and $t=47.5$ ps at the speed of light versus its position x in the plasma (left axis, dotted line) for $n=7 \times n_{\text{res}}$. Axial profile of the plasma density, normalized to n_{res} , at the injection time (right axis, solid line).

In the case of non-resonant excitation, depending on their moment of injection, the electrons are either constantly accelerated or constantly decelerated, *regardless* of the plasma density. The trajectory-averaged electric field $F(t_{\text{inj}})$ is shown in Fig. 3.14

together with the trajectory-averaged normalized laser intensity $G(t_{inj})$ for the $n=7 \times n_{res}$ case. The two quantities, F and G , do not go off-phase with one another, as it is the case with the resonant RPWs shown in Fig. 3.6. This is also observed for simulations performed at other non-resonant plasma densities with laser pulses of various durations and intensities. The maximum trajectory-averaged electric field that can be used to accelerate electrons over the entire interaction length (~ 3 mm) is around 3.5 MV/cm. Overall, a non-resonant PBWA would provide less energy gain than a PBWA operating at resonance, but with much better reproducibility of the energy gain of the phase-locked electrons.

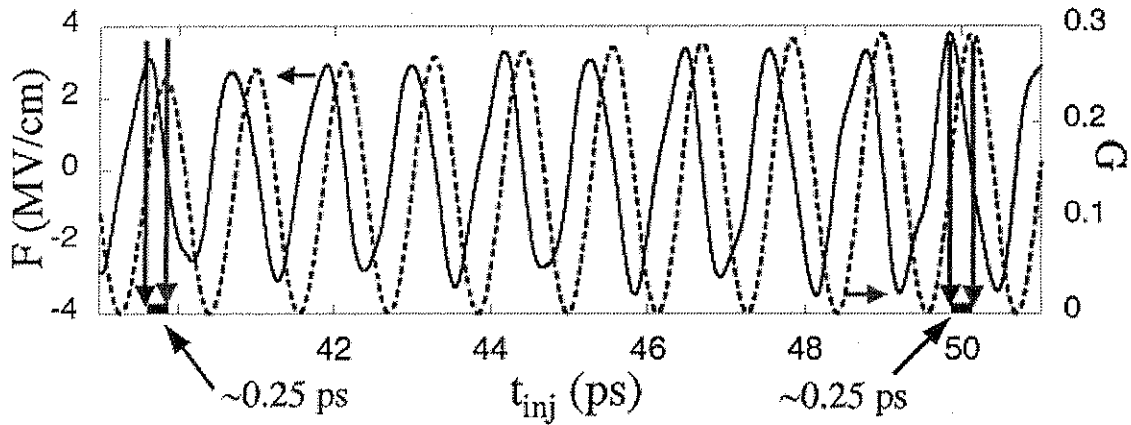


FIG. 3.14: The solid line (left axis) shows the trajectory-averaged electric field F seen by a relativistic electron injected on axis (at $x=0$) versus the injection time, $F=F(t_{inj})$. The dotted line (right axis) shows the trajectory-averaged normalized laser intensity G that the electron is riding along with in the plasma, versus the injection time, $G=G(t_{inj})$. The initial plasma density is $n=7 \times n_{res}$. The constant separation of ~ 0.25 ps between the maxima of F and G (and the phase) is indicated by the vertical arrows.

Experimentally, the excitation of the RPWs in the non-resonant regime represents a slightly easier task than that at resonance because of the not-so-strict conditions imposed on the value of the plasma density. The non-resonant waves excited at plasma

densities much above ω_p can be detected fairly easy if a significant absolute density perturbation δn is created. Therefore, even if their amplitude ε is not large, it is the product $\varepsilon \times n$ that is important for both the TS measurements and electron acceleration (see Eq. 3.4). One factor that remains critical for the experimental observation of the RPWs in either resonant or non-resonant regime is the high intensity of the laser pulse. Details about the laser system and the experimental instruments used to excite and subsequently measure the plasma waves are given in the next chapter.

Chapter 4

Experimental Apparatus

4.1 Introduction

In order to excite a relativistic plasma wave using the beatwave technique, one needs an intense laser pulse operating on two frequencies. The Neptune Laboratory at UCLA that was constructed for the second-generation PBWA experiments hosts such a laser, the interaction chamber, the diagnostic systems and the linear accelerator that produces relativistic electrons to be injected in the plasma wave.

4.2 The Neptune Laser System

The CO₂ laser system in the Neptune laboratory generates TW-level laser pulses with wavelengths around 10- μ m (mid-infrared) that have a larger ponderomotive force, see Eq. 2.3, than the shorter wavelength (1 μ m) pulses produced by solid-state lasers. Let us list the main requirements that the pulses produced by the Neptune laser system have to satisfy in order to qualify for an efficient PBWA driver:

1. the peak power should be on the TW level to provide intensities above the lowest ionization threshold for hydrogen of $\sim 10^{14}$ W/cm² in order to create a few centimeter long plasma;

2. tuning on arbitrary pair of lines (ω_1 and ω_2) to match different plasma densities in the density range 10^{15} cm⁻³ to 10^{17} cm⁻³ and narrow linewidths for these two frequencies compared to $\Delta\omega$;

3. synchronizable on a picosecond scale with the electron beam.

The Neptune laser system satisfies these conditions by operating in a classical MOPA (Master Oscillator Power Amplifier) configuration where a high-quality seed pulse is amplified by a series of amplifiers up to the specified level of power. There are three main components that form this laser system: the master oscillator (MO), the regenerative amplifier (RA) and the large aperture amplifier (LAA). Figure 4.1 shows a simplified schematic of the Neptune laser system together with the other two main components of our experiment, the RF linac and the experimental chamber.

The role of the MO is to create a two-frequency, high-contrast picosecond CO₂ pulse. Since it is difficult to obtain such type of laser pulses directly from a CO₂ oscillator, the pulse is produced by slicing a ~ 150 ns pulse produced by a hybrid laser. This laser combines two low-pressure CO₂ modules with a TEA (transversely excited atmospheric) section to achieve laser oscillation on just two single longitudinal modes[15] by scanning the lengths of the two independent cavities with piezoelectric controllers.

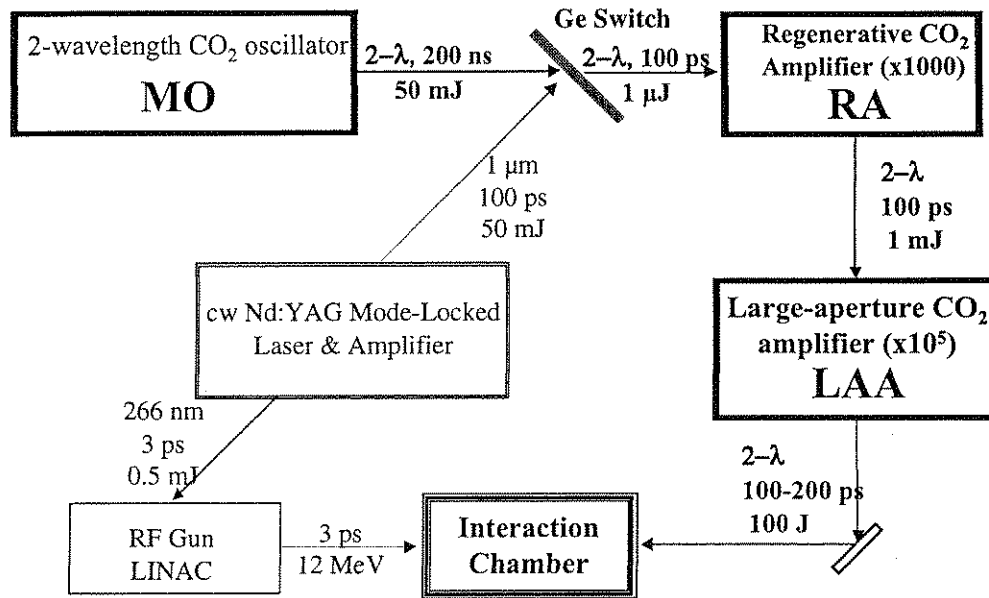


FIG. 4.1: Simplified schematic of the Neptune laser system; MO= master oscillator, RA= regenerative amplifier, LAA= large-aperture amplifier.

This configuration takes advantage of the large number of rotational-vibrational CO_2 lines lying in the range of $9 \mu\text{m}$ to $11 \mu\text{m}$. The pair of lines selected for the PBWA experiments, denoted 10P(20) and 10R(16), correspond to the $10.59 \mu\text{m}$ and $10.27 \mu\text{m}$ wavelengths, respectively. The line ratio is actively controlled by adjusting the losses in one arm inside the folded cavity or by changing the relative timing between the low-pressure sections and the TEA module. The line ratio control at the MO stage is necessary since the gain coefficients for the two lines are not equal. In fact, because each stage of the production or amplification of the laser pulse (MO, RA and LAA) employs CO_2 modules operating with different gas mixtures and at different pressures, the gain coefficient for each CO_2 line is not the same for these stages. Since control of the line ratio is a rather difficult task at the RA and the LAA stages, it is necessary for the MO to produce a seed laser pulse with a $10.6 \mu\text{m}:10.3 \mu\text{m}$ line ratio of

approximately 1:3 to ensure that the energy in the amplified pulse (after the LAA) is equally split between the two lines[16].

A picosecond CO₂ pulse of variable duration (100-400 ps) is sliced from the nanosecond output of the MO using a two stage semiconductor switching system driven by a 100-ps, 1- μ m pulse[17,18]. The 1- μ m pulse is produced by a Nd:YAG laser system formed by an actively mode-locked cw oscillator and an amplifier. A later pulse from the output of the oscillator is amplified (in another amplifier), compressed to \sim 3 ps and frequency quadrupled to 266 nm. This pulse is further used to drive the photocathode of the RF gun, see Fig. 4.1. Therefore, it can be ascertained that the cw Nd:YAG oscillator represents the “clock” of the entire experiment in the Neptune laboratory.

The 1- μ m pulse that is utilized to slice the nanosecond CO₂ pulse contains \sim 50 mJ of energy. This pulse is split in two for the two switches, one that operates in reflection and the other in transmission. Pulses with different widths are created by setting a delay between these switches. The power switching efficiency is approximately 10% and the signal-to-background contrast ratio is 10^3 . During the slicing process, bandwidth is added to the CO₂ pulse depending on its width. We estimate that, following this switch, a 100-ps long pulse will have approximately a 10 GHz bandwidth.

The CO₂ pulse is further amplified in the next stage, the stable regenerative amplifier (RA). In order to amplify the \sim 100 ps far-infrared pulse without a significant increase in the pulse length, a CO₂ module with a bandwidth of at least 10-15 GHz needs to be used. Since a gas laser does not usually have such a large bandwidth, the

pressure broadening mechanism can be used to increase it. The linewidth of a typical CO₂ laser scales linearly with the pressure according to the formula:

$$\Delta\nu(\text{GHz})=3.5\times p(\text{atm}), \quad (4.1)$$

where p is the pressure of the CO₂ mixture in the laser. If we consider that the amplifying medium has a Lorentzian linewidth $\Delta\nu$ and is supposed to amplify a pulse of a τ_{in} duration, we can estimate the length of the output pulse[19]:

$$\tau_{out} = \left[\tau_{in}^2 + \frac{(4 \ln 2) \ln G}{\pi^2 \Delta\nu^2} \right]^{1/2}, \quad (4.2)$$

where G is the total gain that the pulse receives in the laser. To determine the output pulsewidth as a function of the pressure in terms of amplification of 100 ps pulses we take $\tau_{in}=100$ ps, $G=1000$ and we consider $\Delta\nu=3.5$ GHz/atm. Then, Eq. 4.2 becomes[20]:

$$\tau_{out}(ps) = 100 \sqrt{1 + \left(\frac{3.98}{p(\text{atm})} \right)^2}. \quad (4.3)$$

Therefore, the CO₂ laser has to operate at a pressure larger than 5 atmospheres to amplify the 100 ps pulse with less than 20% broadening. To achieve an uniform discharge in the gas mixture at such elevated pressures the inter electrode distance has to be ~1 cm or smaller (for uv-preionized lasers). With such a small aperture for the gain medium, it is not possible to amplify the CO₂ pulses using a multi-pass configuration. That is why it is necessary to use a regenerative amplifier (RA) to initially amplify the seed pulse 1000 times with no significant temporal broadening.

The separation between the CO₂ lines for the P-branch (10.59 μm) and the R-branch (10.27 μm) is 52 GHz and 40 GHz, respectively. When the pressure of the CO₂ gas mixture increases, the gain coefficient for each Lorentzian line in both branches increases due to an additional “boost” from the neighboring lines. Because the R-branch lines are closer spaced than the P-branch lines, the pressure broadening mechanism “helps” the gain coefficient for the R-branch increase faster than that of the P-branch. It is well known that the 10P(20) line has the highest gain of all the CO₂ lines at low-pressures. Therefore, it is fortunate that the pressure broadening mechanism helps equalize the gain coefficients for the 10.59 μm and the 10.27 μm lines, and, in this way, makes the amplification of the two-frequency pulse easier in terms of the line ratio of the output pulse.

The length of the cavity of the RA is approximately 1.5 m and thus the separation between the cavity modes is ~100 MHz. Note that the length of the pulse to be amplified is shorter than the length of the cavity, and, therefore, there are no interference (feed back) effects and no need in fine adjustment of the cavity length of the RA. As it is the case for any injection mode-locked laser with external short pulses, only the bandwidth of the gain medium matters for the temporal profile of the pulse during the amplification process.

The operation of the RA is as follows: the seed pulse that is reflected on the first GE switch is injected into the cavity of the RA; a couple of curved mirrors are used to “match” the injected beam into the cavity; the pulse is amplified while it bounces back and forth inside the RA; it takes between 20 to 30 round-trip passes, depending on how

hard the cavity is pumped, to achieve the necessary 1000 times amplification; at this moment, a pulse train comes out of the RA and goes back on exactly the same path that the seed pulse used to be injected into the cavity; when the pulse train reaches the reflective GE switch, after more than 200 ns, the plasma on the surface of the Ge plate has already recombined; therefore, the plate is transparent now to the CO₂ radiation and the pulse train passes through it; in this way the path of the amplified train of pulses is separated from the path of the input seed pulse.

The temporal shape of the pulse train was measured for each wavelength. A spectrometer was used to separate the lines and two room-temperature detectors (PEM-L-5, Boston Electronics) were used in combination with a 1-GHz scope to record a trace of the pulse trains that is showed in Fig. 4.2 (both channels are shown on one single trace, the 10.27 μm channel is delayed with ~ 5 ns).

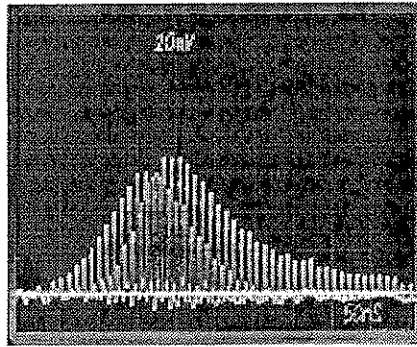


FIG. 4.2: The 10.27 μm and the 10.59 μm pulse trains as recorded in one trace at the output of a spectrometer. The 10.27 channel was delayed with 5 ns and then added to the 10.59 channel. The 10.27 μm pulse train appears first in time, from left to right. The two detectors have similar sensitivities but the 10.27 channel is attenuated ~ 2 times. The vertical is 10 mV/div and the horizontal is 50 ns/div.

Since the seed pulse contains more 10.27 μm than 10.59 μm , the pulse train carries at the beginning more 10.27 μm . The line ratio changes continuously in time. Figure 4.2

shows that it is possible to time the “extraction” process of one of the pulses out of the pulse train in such a way that this single pulse will contain the desired line ratio necessary for the next amplification stage, the LAA. The fast detectors were then replaced with energy meters and the energy in each channel was recorded for 10 consecutive shots. Figure 4.3 shows the ratio between the energy contained in the 10.27 μm pulse train to the energy contained in the 10.59 μm pulse train. Generally there is 3 times more energy for the 10.27 channel to compensate for the higher gain of the 10P(20) line in the LAA. Figure 4.3 also shows the line ratio stability in the normal operating conditions.

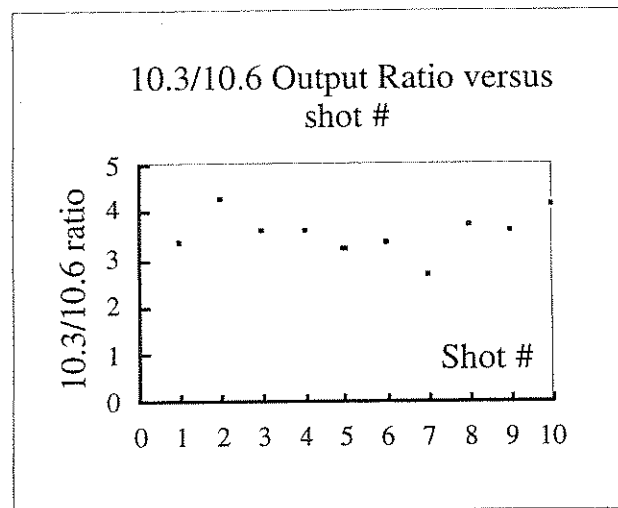


FIG. 4.3: The energy ratio between the 10.27 μm and 10.59 μm pulse trains for ten consecutive shots.

The contrast of the pulse train depends of the contrast of the input seed pulse which is limited to $\sim 10^3$ since the Ge switching plates can only be oriented for one wavelength or the other. Another technique that can be used to produce picosecond two-wavelength (seed) CO_2 pulses with a similar 10% switching efficiency and a superior contrast of 10^5

is described in Appendix B. A good signal-to-background contrast of the seed pulse helps the output pulse gain the competition with the amplification of the nanosecond long “leakage” that is sent into the RA by the imperfect Ge switches. A better contrast of the pulse produced by a MO might be very helpful when amplification of pulses as short as 2 ps is considered[21]. The temporal profile of the pulse trains shown in Fig. 4.2 resembles that of a gain-switch laser pulse. In such cases it is possible for the short pulse to deplete the gain medium in the RA to the extent where that stray injected leakage will not be fully amplified and so, the actual contrast of the pulse train could be better than 10^3 .

The “extraction” of a single pulse out of the pulse train is achieved by a Pockels cell. The cell is driven by a 10-ns high voltage, ~14 kV, pulse provided by a power supply in combination with a laser-triggered spark gap. This selection system can single-out approximately 80% of one of the pulses, usually close to the peak of the pulse train. Due to stray reflections of the high-voltage pulse, post pulses are also switched out of the pulse train with an efficiency of few percent. The energy in the single pulse was measured to be ~1 mJ and its spatial profile is Gaussian[20]. Figure 4.4 (a) shows the pulse train without the switched-out pulse and Fig. 4.4 (b) shows the scope trace of the single pulse.

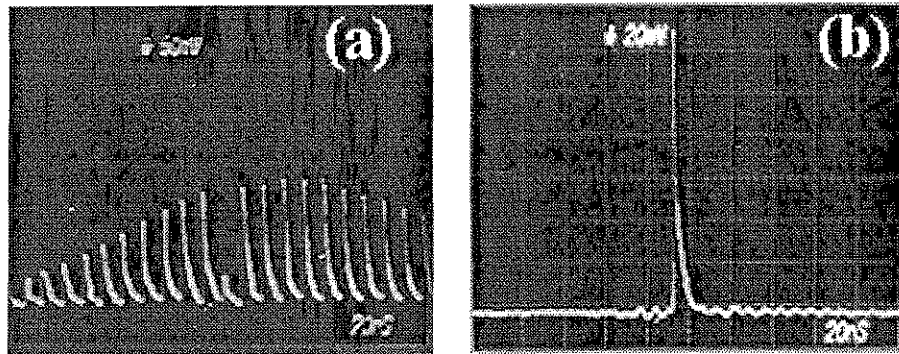


FIG. 4.4: (a) Pulse train without the selected pulse, vertical 50 mV/div, horizontal 20 ns/div. (b) Single pulse switched-out by the Pockels cell, vertical 20 mV/div, horizontal 20 ns/div.

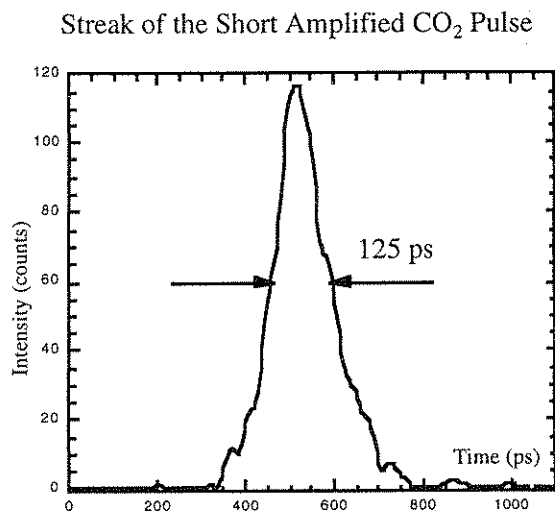


FIG. 4.5: Lineout of the streak image of the 1-mJ CO₂ pulse (after the regenerative amplifier) obtained by frequency mixing in a nonlinear crystal.

The precise duration of the CO₂ pulse after the RA was determined using a streak camera (Imacon 500, Hadland Photonics) that can record visible light pulses with a resolution on the order of 10 ps. The CO₂ light was “added” with the 658-nm light from a laser diode in a nonlinear crystal (AgGaS₂) using a type I phase-matching sum frequency mixing process. The stray light at 658 nm is filtered out, while the new light

at 620 nm consisting of a pulse that has the same temporal profile of the mid-infrared pulse is sent towards the streak camera. Figure 4.5 shows the lineout of a streak image of a CO₂ pulse that is shown to have a full-width at half-maximum (FWHM) of ~125 ps. Overall, the first two stages, the MO and the RA, can produce two-wavelength, 10.59 μm and 10.27 μm, CO₂ pulses from 100 ps to 400 ps and with a peak power between 2 to 10 MW. These pulses are amplified in the last stage, the large-aperture amplifier.

The energy of the CO₂ pulse is increased from 1 mJ to approximately 100 J in the 3-pass (each 2.5-m long) amplifier. The laser module has a large cross section of 20 cm×35 cm and operates with a mixture of 80% CO₂ and 20% N₂ at a pressure of 2.5 atmospheres. The 14 GHz bandwidth of the gain medium is not large enough to amplify 100-ps pulses without broadening. Such a 100-ps pulse broadens to approximately 300 ps when amplified 10⁵ times. In order to obtain shorter amplified pulses, the laser pulse is sent through a passive plasma shutter that is placed in the focus of a telescope (*f*/60) after the first pass. The time-varying high-density plasma modulates the phase of the pulse, especially the falling edge of the pulse. The leading edge is continuously amplified and steepens up while the blue-chirped falling edge is less amplified. Therefore, the pulse shortens and amplifies up to the point where strong power broadening of the gain medium provides the necessary bandwidth to produce pulses as short as 40 ps[22]. Depending on the density of the plasma in the plasma shutter that can be adjusted by changing the pressure of the gas fill, pulses from 40 ps to 300 ps are produced with a maximum power of 1 TW. The power was calculated from the energy and pulse length

measurements. In addition, the power of the laser pulse was checked by focussing the pulse into a low-pressure (<0.3 Torr) interaction chamber filled with gases like He and Ar to a spot size of $\sim 70 \mu\text{m}$. The CO_2 pulse was attenuated down to the tunneling ionization threshold intensity for these gases[23]. Measurements of the plasma appearance in both Ar and He confirmed that the peak power of the CO_2 pulse produced by the Neptune laser system is approximately 1 TW.

4.3 Neptune Experimental Area

The PBWA experiments combine the TW CO_2 laser pulse with the electron beam produced by a RF gun and a linear accelerator (LINAC). A simplified schematic of this combination was shown in Fig. 4.1. The role of the CO_2 pulse is, on one hand, to create the plasma by ionizing the gas, and, on the other, to excite the plasma wave. It is desirable to have RPWs with a wavelength λ_p both longer and shorter than the transverse extent of the plasma. In other words, it is important to study both 1-D and 3-D types of plasma waves. The high power of the laser pulse allows the pulse to be split in two parts, one that is focussed with a $f/3$ off-axis paraboloid (OAP), and the other, with a $f/18$ NaCl lens. These two arms are therefore called the $f/3$ arm and the $f/18$ arm. The $f/3$ arm contains 20-25% of the pulse energy and is focussed to a $1/e^2$ spot size $2w_0=100 \mu\text{m}$. The rest of the energy is sent to the $f/18$ arm and focussed to a $1/e^2$ spot size $2w_0\cong 350 \mu\text{m}$. Both arms can produce plasmas alone. The $f/3$ plasma is 2-3 mm long while the $f/18$ is up to 40 mm long. Figure 4.6 shows schematically the way the

two laser arms are sent collinearly on the same path with the electron beam in the Neptune experimental area. Overall, in the experiments, one can use the f/3 arm only, the f/18 arm only, both arms together (in space and time, see delay line in Fig. 4.6) with the laser operating on 10.59 μm only, the 10.27 μm only or on both CO₂ lines. All these options lead to a variety of experiments that can include or not the electron beam.

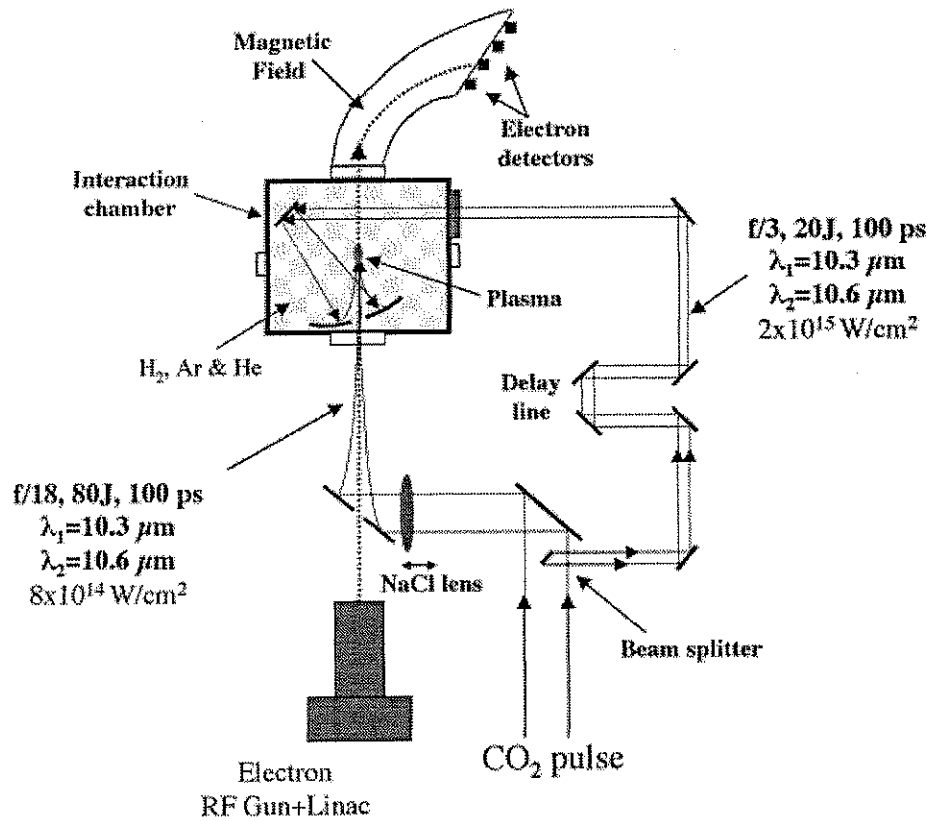


FIG. 4.6: Simplified schematic of the Neptune experimental area.

The electron beam is produced by the photo-injector in the Neptune laboratory. The photo-injector has split accelerator design consisting of a photo-cathode gun, a drift space, and a booster linac known as a plane wave transformer (PWT). The photo-cathode is driven by a 3-ps UV laser pulse made by a laser system that begins with the

1064 mode-locked Nd:YAG oscillator (Antares, Coherent) shown in Fig. 4.1. From the cw train of 100-ps pulses that represent the output of this laser, one pulse is selected and chirped into a 500-m long optical fiber. The pulse is then amplified by a regenerative amplifier by approximately 10^6 times. A pair of gratings is used to remove the chirp and compress the pulse. Adjustments to the grating pair allow control over the pulse length, which is typically 6 ps (FWHM). Two consecutive BBO crystals are used to frequency-double the 1064-nm pulse to produce a 3-ps, 266-nm UV pulse that has ~ 130 μJ of energy. This pulse is transported to the single-crystal copper photo cathode of the RF gun. The combined accelerating fields of 85 MV/m of the RF gun and the ~ 50 MV/m of the PWT linac boost the energy of the electrons to 12 MeV with an energy spread of 0.2% and a total charge of up to 300 pC.

The electron beam is injected collinearly with the CO_2 pulse through a 1-mm hole in a flat mirror under vacuum, see schematic in Fig. 4.6. The direction of the beam and its size is controlled by a set of three quadrupole magnets placed on the outside of the vacuum tube. A couple of specially designed screens are used to monitor the position of both the e-beam and the 10- μm pulse. The electrons and the photons are aligned collinearly with 0.1-degree alignment accuracy. For the PBWA experiments the electron bunch contained typically up to 3×10^8 electrons per shot and it was focussed down to $\sigma_{\text{rms}} = 150$ μm . A correlation technique based on the modulation of transmission of the CO_2 laser pulse by the electron pulse in a thin Ge slab[24] was used to synchronize the electrons with the 10- μm photons with 20-ps uncertainty. Because the duration of the electron pulse is < 10 ps, it overlaps with few wavelengths of the RPW.

The spectrum of the electrons exiting the plasma within a full cone angle of 1 degree was analyzed using a 0.4 T magnetic field applied by a dipole magnet with Browne & Buschner pole pieces (with imaging properties in the energy plane) in combination with a set of Si surface barrier detectors (SBDs) and two fluorescent screens (Lanex) with different sensitivities. One screen was used to detect electrons with energies of ~12 MeV (injection energy), and the other, approximately 100 times more sensitive, from 12.5 MeV to 15 MeV. The number of electrons was estimated by converting the brightness of the fluorescence produced by the electrons using experimentally determined fluorescence efficiency. The SBDs, calibrated with a β source, were used to detect electrons with energies higher than 15 MeV. Special care was taken in shielding the SBDs against stray 12-MeV electrons and X-rays that were produced during the shots. No significant signals above the noise level were measured on the detectors when there was no plasma but a beat-wave and an electron beam; or plasma produced by a single frequency pulse and an electron beam; or plasma produced by a beat-wave but no injected electron beam.

The injection of electrons into the RPWs represented the second stage of the research on the PBWA in Neptune laboratory, after the detection and characterization of the plasmas and the plasma waves. The outcome of the electron acceleration experiments will be shown towards the end of Chapter 6 that contains the experimental results. The next chapter describes a novel diagnostic system that was built around a fast detector, the Imacon 500 streak camera, and was used to detect and characterize the RPWs excited by the TW CO₂ laser pulse produced by the Neptune laser system.

Chapter 5

Collinear Thomson Scattering Diagnostic System

5.1 Introduction

One way to diagnose a RPW is to probe it with a laser beam. The plasma wave essentially represents a moving density perturbation (phase grating) which scatters the probe photons. By analyzing the scattered light, one can measure the frequency and wavenumber of the RPW as well as its amplitude. This information can be used to further calculate the value of the accelerating electric fields induced by the RPW. This method is known as coherent or collective Thomson scattering (TS) and is extensively used as a diagnostic technique for laboratory plasmas[25,26].

In a TS experiment, the probe light scatters off an electron plasma wave with frequency ω_{epw} . The scattering process results in generation of sidebands, Stokes and anti-Stokes, around the frequency of the probe light, ω_{probe} . The frequency of the scattered light, ω_s , is then given by:

$$\omega_s = \omega_{probe} \pm m \times \omega_{epw} \quad (5.1)$$

where $m=1, 2, 3$, etc. The fact that ω_s is slightly different than ω_{probe} is crucial for the detection of the scattered light. Generally, the laser driven RPWs have frequencies around the natural resonances of the plasma, like the plasma frequency, ω_p , given (in cgs units) by:

$$\omega_p = \sqrt{\frac{4\pi n e^2}{m}} \quad (5.2)$$

Therefore, the separation between the frequencies of the scattered and the probe light is proportional to the square root of the plasma density, n .

Thomson scattering is a very useful diagnostic that is limited, however, by the extremely small efficiency of the scattering process in many of the laboratory experiments. Scattering from RPWs is particularly challenging. In order to conserve both the momentum and energy (conditions known as the ω and k matching), scattering must be done in the exact forward direction. The scattering efficiency, given by the ratio of the scattered power P_s , to the incident power of the probe beam, P_0 , is[27]:

$$P_s/P_0 = 0.25 (\delta n r_0 \lambda_{\text{probe}} L)^2, \quad (5.3)$$

where δn is the magnitude of the density fluctuation associated with the plasma wave, r_0 is the classical electron radius, λ_{probe} is the wavelength of the probe laser, and L is the interaction length between the electrons of the wave and the probing photons. The density fluctuation normalized to the plasma density is referred to as the wave amplitude, $\epsilon = \delta n/n$. For an example of a typical Thomson scattering efficiency, consider a scattering experiment on a 10% plasma wave at $n=10^{16} \text{ cm}^{-3}$, with $\lambda_{\text{probe}}=5 \cdot 10^{-5} \text{ cm}$, and $L=0.05 \text{ cm}$. In this case, P_s/P_0 is very small, $\sim 10^{-7}$. Additional

losses for the scattered light occur in the transportation line and reduce P_s even more, approximately 10 times. Therefore, the detection of the scattered light at these low scattering efficiencies represents a very difficult task. Overall, there are two issues that hinder TS measurements at low-plasma densities, between 10^{15}cm^{-3} and 10^{17}cm^{-3} . First, from Eq. 5.3, because $P_s/P_0 \sim (\epsilon n)^2$, the scattering efficiency decreases significantly with n at a fixed amplitude of the plasma wave. Second, the lower the plasma density, the closer the sidebands are to the probe wavelength (from Eq. 5.1 and Eq 5.2) and the more difficult it becomes to separate the scattered light from the probe light.

Due to these difficulties, only the detection of a transverse component of RPWs at low plasma densities ($n \sim 10^{16}\text{cm}^{-3}$) has been achieved in 1985 by Clayton et al.[28]. In that experiment, the plasma wave's small transverse size provided a significant transverse wavenumber component that was detected by small-angle TS. With the probe beam at $\sim 90^\circ$ to the RPW direction, the small angular shift helped separate P_s from P_0 . However, this geometry cannot be used when the transverse size of the RPW is larger than its wavelength (i.e., more 1-D-like waves) and therefore the transverse component is small. Also, it is preferred for a TS experiment to directly measure the on-axis (longitudinal) component of a RPW since the resulting estimate of the wave amplitude does not require exact knowledge of the transverse structure of the wave.

The conservation of momentum defines the geometry of a TS process and relates the wave vector of the scattered pulse, \mathbf{k}_s , to the wave vector of the electron plasma wave, \mathbf{k}_{epw} :

$$\mathbf{k}_s = \mathbf{k}_{\text{probe}} \pm \mathbf{k}_{\text{epw}}, \quad (5.4)$$

where $\mathbf{k}_{\text{probe}}$ is the wave vector of the probe beam. Eq. 5.1 and Eq. 5.4 have to be simultaneously satisfied for all coherent TS processes. In the somewhat special case of scattering from the longitudinal component of a RPW where $\omega_{\text{epw}}/k_{\text{epw}} \cong c$, the only possible scattering geometry is the collinear one where the probe pulse propagates along the same direction as the plasma wave[29,30].

Collinear TS experiments (with an independent probe pulse) successfully detected RPWs when the plasma density was 10^{17} cm^{-3} or higher[31,32,33], by taking advantage of the fact that both P_s/P_0 and the frequency separation between the scattered and probe light increase with increasing n . In another series of TS experiments, the relativistic plasmons were diagnosed using longitudinal pump-probe interferometry with laser pulses shorter than the plasma wavelength[34,35,36].

At low plasma densities, the only measurements that showed the existence of the RPWs in a collinear scattering geometry are the forward self-scattering experiments performed at $n=10^{16} \text{ cm}^{-3}$ using the beatwave excitation technique[28,37]. Though this type of measurement succeeded in analyzing the time variation of the RPWs[38], it is difficult to estimate the amplitude of the plasma waves due to the strong four-wave mixing phenomena that also participate in the production of the sidebands[37]. Also, a precise determination of the amplitude ϵ of the plasma wave in the forward-scattering experiments is complicated because the “probe” pulse may be strong enough to affect the plasma wave itself. It is important for the probe pulse to be (1) powerful enough to bring the scattered light at detectable levels, and (2) sufficiently weak not to affect the

plasma or the plasma wave[25]. Therefore, it is preferred for the TS experiments to be performed with an independent probe beam.

In this chapter we present a collinear Thomson scattering diagnostic system for the study of relativistic plasma waves. Both the frequency and the k-matching relations, Eq. 5.1 and Eq. 5.4, are satisfied and an independent probe pulse is used. Relativistic plasma waves are detected in a wide range of plasma densities, from $2 \times 10^{15} \text{ cm}^{-3}$ to 10^{17} cm^{-3} . The main task is to separate the signal (scattered light) from the probe light that is $\sim 10^9$ times more intense and only $\pm 8 \text{ \AA}$ away at $n=10^{16} \text{ cm}^{-3}$. For this purpose a novel spatial-spectral filter was devised.

5.2 Experimental Setup

The collinear TS experimental setup was designed initially to detect the plasma waves produced by the $f/3$ arm. The energy of the two-wavelength CO_2 laser pulse was varied from 20 J to 80 J. This energy was generally distributed between the two CO_2 lines with a ratio of 10.6 \mu m to 10.3 \mu m of approximately 3:1. Throughout this study, the CO_2 lines are kept unchanged. Therefore, the difference between the two frequencies of the CO_2 pulse, $\Delta\omega$, is the same for all shots. The $10\text{-}\mu\text{m}$ beam is focused into an interaction chamber with the $f/3$ OAP that has a focal length $f = 15.2 \text{ cm}$. The beam hits the OAP at an angle of ~ 40 degrees with a maximum diameter of 9 cm. The focusing given by this OAP can be varied from $f/1.5$ to $f/4$ by limiting the beam diameter with an iris. The maximum intensity achieved is approximately $2 \times 10^{15} \text{ W/cm}^2$.

The plasma density is given by the pressure of the fill gas. The pressure was monitored with a capacitance manometer gauge (CM100-G10A, Leybold-Heraeus) with an accuracy of 1% of the reading. The plasma density was directly inferred in the same manner as Clayton et al.[30] and Villeneuve et al.[39] by recording the frequency shift acquired by a probe beam that scatters on the plasma waves driven by stimulated Raman scattering (SRS). The results from these 90° Thomson scattering measurements (the scattering is performed transversely to the wave vector of the SRS waves) are presented in detail in Appendix C. Figure 5.1 presents the correlation between the plasma density given by the pressure gauge readings (assuming full ionization of the filling gas) and the plasma density inferred from scattering on SRS-driven waves in H₂.

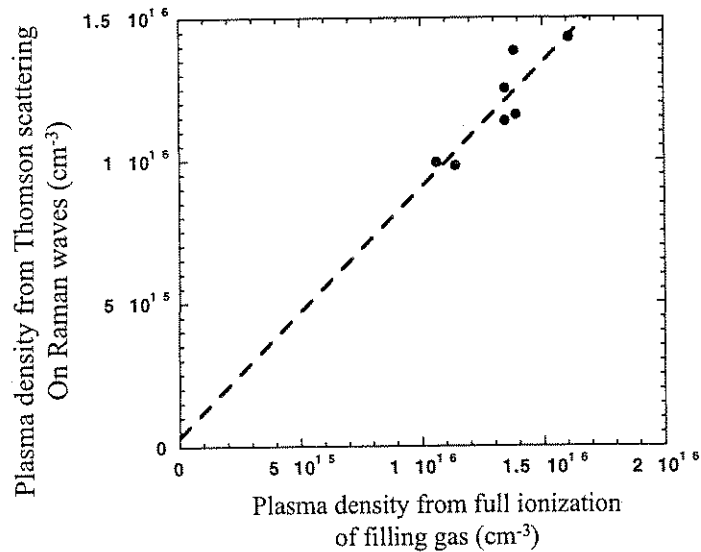


FIG. 5.1: Plasma density from scattering measurements on SRS waves versus the plasma density assuming full ionization of H₂ molecules; the dashed line represents a linear fit of the experimental data.

The dashed line in Fig. 5.1 represents a linear fit of the data points. The actual plasma density n can be expressed as a function of the n_{gas} which is the plasma density given by the pressure of the gas assuming full ionization of all the H_2 molecules:

$$n_{\text{gas}}(\text{cm}^{-3}) = 1.15 \times n(\text{cm}^{-3}) - 3.95 \times 10^{14}. \quad (5.5)$$

The difference between n and n_{gas} could be attributed to the temperature effects related to the excitation of the SRS waves, incomplete ionization of the gas or to a small deviation of the fit compared to the exact dependence due to the rather few data points. The relationship between the pressure of the H_2 gas p_{gas} and n_{gas} is $p_{\text{gas}} = 0.5 \times n_{\text{gas}} kT$ where $k = 1.38 \times 10^{-23} \text{ JK}^{-1}$ is Boltzmann constant and $T = 300 \text{ K}$ is the temperature of the gas. For the two CO_2 lines the resonant density is $n = 9.4 \times 10^{15} \text{ cm}^{-3}$. The pressure of the H_2 gas in the interaction chamber has to be $p_{\text{gas}} = 170 \text{ mTorr}$ so that $\omega_p = \Delta\omega$. Within the experimental errors we can conclude that the majority of the hydrogen atoms in the focal volume are being ionized and the plasma density can be controlled by changing the gas pressure.

In any TS measurement, the parameters of the probe laser pulse are determined by the conditions of the experiment. In our case, the temporal evolution of the RPW on very fast time scales demands the use of a streak camera. Thus, the wavelength of the probe pulse is set from the beginning to be in the visible range. Then, due to the very small scattering efficiencies, between 10^{-8} and 10^{-10} , the peak power of the probe pulse has to be above the MW level to obtain good signal levels.

A commercial Nd:YAG laser equipped with a frequency-doubling nonlinear crystal was selected to provide the probe pulse that satisfies the above-mentioned conditions.

This laser (DCR-11, Quanta-Ray) produces a 2 ns-long, linearly-polarized Q-switched pulse having approximately 50 mJ of energy. Using a calibrated Ne lamp (Oriental Instruments), we found that $\lambda_{\text{probe}}=532.10\pm0.02$ nm (green). The pointing stability at the focal plane of the plasma-producing laser pulse is better than 20 μm when the temperature at which the laser is operating is maintained constant. This, combined with the good pointing stability of the CO_2 laser, ensured that the scattering process takes place every shot.

Another important requirement for the probe laser pulse is related to its bandwidth. The scattered light is comprised of sidebands that have their wavelength shifted from λ_{probe} by just few \AA . It is therefore important for the bandwidth of the probe pulse to be small enough so that the very weak signal at frequency ω_s will not be overcome by laser power in the “wings” of the spectrum of the probe pulse. The spectrum of the visible laser pulse used in this experiment was measured using the high-quality optical filter that will be described in the next sections. The measurement showed that the spectral power drops sufficiently fast, allowing for the detection of signals situated more than $\pm 2 \text{\AA}$ (~ 250 GHz) away from the centerline of the probe light. In addition, two weak Raman-like sidebands produced within the laser cavity were detected in the spectrum at 532.1 ± 0.65 nm. These sidebands are present for all shots, with or without plasma. They have the same temporal profile as λ_{probe} and do not represent a Thomson scattering signal.

A simplified version of the experimental setup (top view) is presented in Fig. 5.2. The most important elements in the TS diagnostic setup are: the interaction (vacuum)

chamber where the plasma wave is produced and where the scattering phenomena take place, the DCR-11 laser that produces the probe pulse, the optical system used to filter-out the probe light and the following optical tools necessary for the detection and measurement of the scattered radiation. The inset of Fig. 5.2 shows an alternative scattering geometry within the interaction chamber that was used to detect the $f/18$ produced RPWs. The rest of the optical setup was used with no significant differences in both the $f/3$ and the $f/18$ collinear TS experiments.

The plasma is produced by focusing the two-wavelength CO_2 laser pulse with the OAP at the interaction point (IP) at the center of the interaction chamber. The OAP has a 1.5-cm hole through which the probe beam is injected on axis. The probe beam is focused at the IP by the lens L1. The infrared and visible beams copropagate within an angle of less than 0.4° . After passing through the focus, the CO_2 beam expands and stops on a teflon dump that has a 1.5-cm hole in the center for the transportation of the probe pulse. A Gaussian fit of the profile of the probe beam at the IP shows a $1/e^2$ intensity spot size $2w_0=180 \mu\text{m}$, slightly larger than the size of the CO_2 laser pulse. The 532 nm beam thus spatially covers the plasma wave over its entire length of ~ 2 mm. Furthermore, to avoid any chance of misalignment during operation due to the thermal drift of the Nd:YAG laser, an on-line beam position monitor was installed by collecting the “leakage” through a high-reflective mirror.

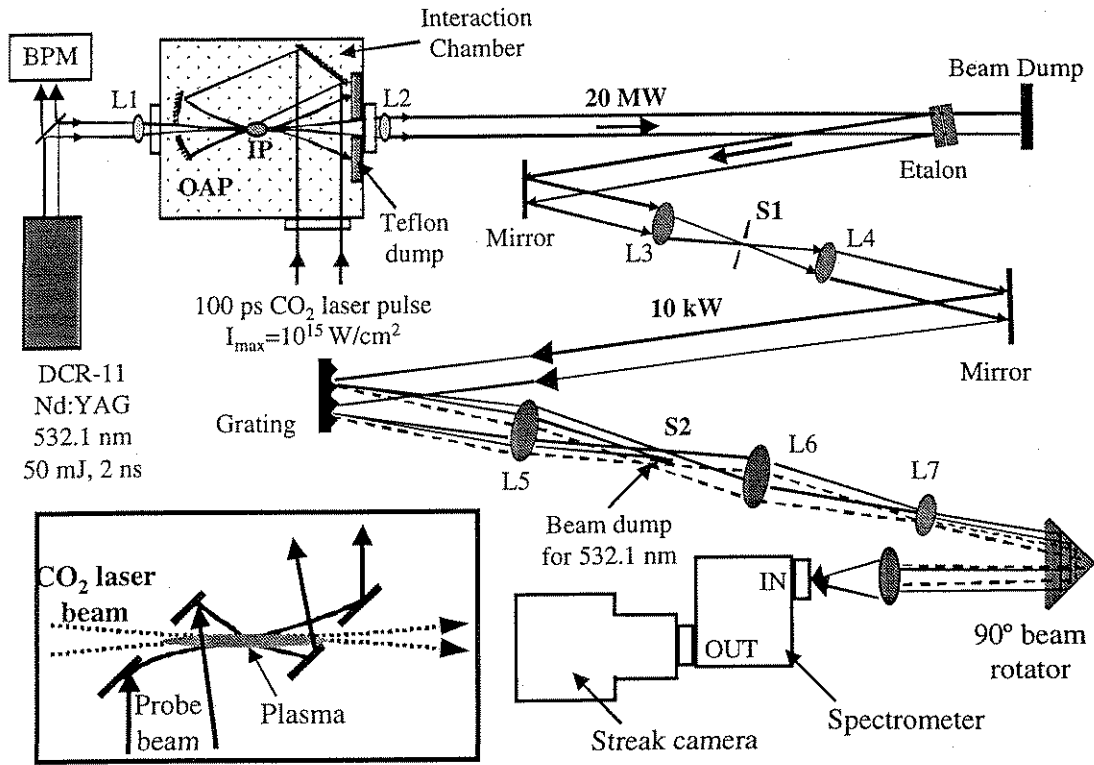


FIG. 5.2: Collinear Thomson scattering experimental setup. L1 to L7 are lenses; S1, S2=spatial filters; OAP=Off Axis Parabolic mirrors; IP=Interaction Point, BPM=beam position monitor used to check the pointing stability of the probe beam. The inset shows an alternative probing geometry for $f/18$ CO₂ laser plasmas ($w_0=200 \mu\text{m}$).

After passing through the plasma, the probe beam and the scattered radiation expand and are recollimated by the lens L2. After the IP, as a result of the scattering process, $\sim 10^{-9}$ of the photons in the probe pulse (for ~ 100 ps) acquire a shift in frequency that makes their wavelength differ from λ_{probe} by $\pm 8 \text{ \AA}$. To separate these photons from the ones that did not scatter on the RPW, a high-quality filter is necessary[40].

The filtering process in our experiment is done by a novel spatial-spectral optical system consisting of two components. The first one is a high-power filter based on a air-

spaced Fabry-Perot etalon and a spatial filter (S1). The second is a high-quality, low-power filter made of a 2400 grooves/mm grating and another spatial filter (S2).

The etalon is used as a reflecting notch filter. That is, it reflects both the red and blue shifted scattered light and transmits the probe light. In between the etalon and the grating there is the spatial filter S1 made of two 300 mm focal length lenses (L3 and L4) and a 200 μm pinhole. The goal of the spatial filter is to block some of the stray light accumulated by the high-power probe pulse passing through or reflecting on all the 23 interfaces present in the beam path up to that point, including the etalon. It should be mentioned that some of the optics used for transportation and alignment are not shown in Fig. 5.2 to allow a clear picture of the essential optical elements.

The spatial filter S1 “geometrically” cleans the beam for the next optical elements, the grating and the spatial filter S2. Without the S1 filter, the capability of the grating to reduce the stray light decreases ~ 1000 times. The dispersive properties of the grating are exploited by the spatial filter S2 (formed by lenses L5 and L6 and a beam dump) which blocks the probe light and transmits the sidebands. Since the dispersion of the grating is not compensated by another dispersive element (to avoid introducing more losses), it is necessary to use one more lens, a field lens L7[41], placed at a waist between the grating and the spectrometer to collect as much of the spectrum as possible and transport it to the detection system. After the filter S2, the power of the stray light decreases from 10 kW to less than 2 mW (including losses).

At $\sim\text{mW}$ levels of power, the stray light and the signal cannot produce any damage to the detection system formed by an imaging spectrometer and a streak camera (see

Fig. 5.2). After the S2 filter, a 90-degree beam rotator transforms the horizontal dispersion plane into a vertical one, so that different wavelengths in the probe beam will be positioned vertically along the slit of the imaging spectrometer. The role of the spectrometer is to again separate the scattered light and the stray probe light, which by now have comparable levels of power when the RPW amplitude is around 10%. The streak camera is used to record the temporal evolution of the fundamentals and higher harmonic sidebands. The stray-light rejection factor for the entire optical filter (including the spectrometer) is $\sim 10^{-12}$. A more detailed description of the main components of the spatial-spectral filter and the detection system is presented below.

5.3 The Etalon

The etalon shown in Fig. 5.2 is an air-spaced Fabry-Perot etalon with anti-reflection (AR) coatings at 532 nm on the external surfaces. It is designed to reduce the intensity of the stray light below the damage threshold for the next dispersive component of the filtering system (the holographic grating), on one hand, and, on the other, to transmit as much of the scattered light as possible.

If $\Delta\phi$ represents the phase change acquired by the probe light for one round trip of the etalon, then, at normal incidence:

$$\Delta\phi = 4\pi L / \lambda_{\text{probe}}, \quad (5.6)$$

where L is the thickness of the etalon. The steady-state (i.e. after some fill time) reflectivity and the transmission of an etalon can be expressed as[42]:

$$R=I_r/I_i=(\mathfrak{F}\sin^2(\Delta\phi/2))/(1+\mathfrak{F}\sin^2(\Delta\phi/2)) \text{ and } T=I_t/I_i=1/(1+\mathfrak{F}\sin^2(\Delta\phi/2)), \quad (5.7)$$

where I_r , I_t and I_i represent the intensities of the reflected, transmitted and incident beams on the etalon, respectively. The corresponding reflection and transmission coefficients are R and T , respectively. The finesse \mathfrak{F} of the etalon is defined as:

$$\mathfrak{F}=4\mathfrak{R}/(1-\mathfrak{R})^2, \quad (5.8)$$

where \mathfrak{R} is the reflectivity of each etalon surface (assumed to be equal here).

Before the etalon was installed in the TS experimental setup, a Tungsten lamp was used as a white-light source to check the spectral properties of the etalon. The white-light, collimated with a spatial filter, was sent through the etalon and into a spectrometer coupled to a 16-bit CCD camera. The experimental arrangement is shown in Fig. 5.3 (a).

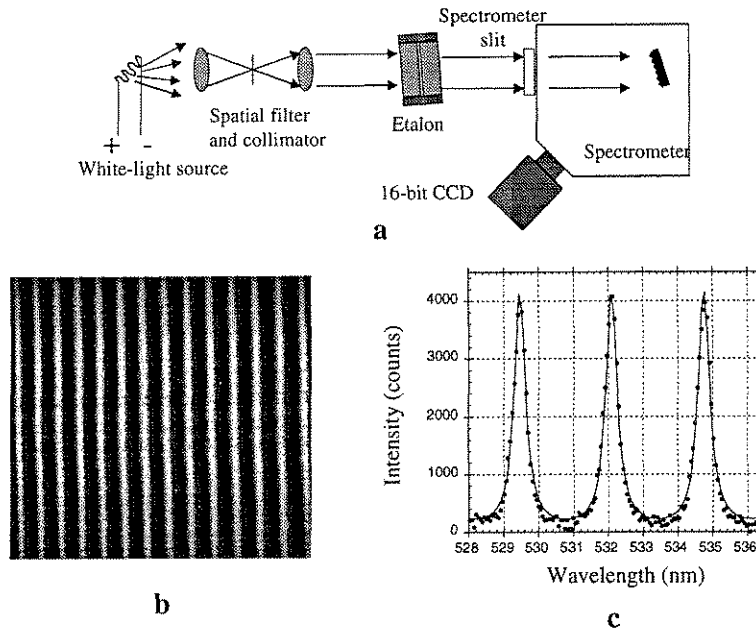


FIG. 5.3: Experimental setup used to measure the spectral properties of the etalon (a), fringes obtained on the 16-bit CCD camera (b), and lineout through the fringes (dots) superimposed on a etalon transmission fit line using Eq. 5.7 (c).

Even if the coherence length of the lamp is much less than L , interference effects can still be easily observed. A similar spectral interference phenomenon has been demonstrated in 1994 in a Mach-Zehnder interferometer[43]. The presence of the etalon in the path of the white-light induces the appearance of spectral fringes (recorded by the CCD camera) in the output plane of the spectrometer, see Fig. 5.3 (b). A lineout through these fringes was fit using Eq. 5.7. The thickness of the etalon, $L=52 \mu\text{m}$, and its finesse, $\mathcal{F}\cong 10$, are extracted from this fit. Also, the reflectivity of the etalon at $\lambda=\lambda_{\text{probe}}\pm 8 \text{ \AA}$ is measured to be $\sim 95\%$, close to the number initially projected in the theoretical design. The important parameters of the etalon are specified in Table I.

Characteristic	Value
Thickness	52 μm
Clear aperture	30 mm
External Interfaces	AR coated for 532 nm
Internal Interfaces	74% [$\pm 2\%$] reflective at 532 nm
Free Spectral Range	2.7 nm
FWHM	0.26 nm
Fill Time	<1 ps
Finesse	10.37
Internal Field Enhancement	3.8 times
Damage Threshold	2 J/cm ² for 8 ns pulses at 1 μm

Table I. Characteristics of the etalon used to filter out the stray light.

The amount of stray light at 532 nm reflected by the etalon was measured with the probe laser pulse at full power. It was found that ~10% of the incoming light is reflected, more than expected from the theoretical estimations. This is due, on one hand, to the imperfect alignment of the inner surfaces of the etalon, and, on the other, to the interference produced by the external interfaces of the etalon. Even if these surfaces are AR coated, they still interfere well enough to increase the stray light reflectivity at λ_{probe} . Therefore, it was necessary to use the etalon in a triple-pass configuration to reduce the stray light 1000 times and reflect ~86% of the scattered light. To use the etalon in a multi-pass configuration the scattered light is redirected towards the etalon at different angles of incidence corresponding to different transmission maxima for λ_{probe} . Although the effective thickness of the etalon slightly increases for the additional passes, its transmission properties are not significantly changed. In Fig. 5.2, the etalon is represented in a one-pass configuration for simplicity.

The 1000-times reduction of the power (and energy) of the stray light is crucial for the operation of the spatial filter S1. The 10-kW, 532-nm light passes through the 200- μm pinhole of S1 without creating any plasma (spark) that could affect the scattered light and the operation of the filtering grating.

5.4 The Filtering Grating

The attenuation of the 532-nm light introduced by the etalon is not enough to bring the power of the probe beam to a safe level for the streak camera. Additional filters are

needed in order to reduce the stray light to the level of few mW. The total attenuation needed is more than 6 orders of magnitude and so a high-quality filter is necessary. For this purpose we use a grating in combination with the spatial filter S2.

It is well known that holographic gratings can be used as dispersive elements with extremely good stray-light rejection factors[44]. A 2400 grooves/mm grating (Jobin Yvon) was selected as an additional filter. The performance of the grating as a stray light filter was tested in various operating geometries before it was introduced in the experimental setup. Approximately 1 mJ of the output of the probe laser was transported directly onto the grating. The incidence and the reflection angles were varied to provide different dispersions. The probe light that was reflected in the first order was focussed with lenses with focal lengths varying from 30 cm to 1 m. A sharp edge (razor blade) was used in the focus of the lens as a dump for the 532.1-nm light. The blade was mounted on a micrometer translation stage that can move perpendicularly on the direction of propagation of the probe pulse. The filtering process was simulated by moving the edge into the beam. Behind the razor blade a photodiode recorded the amount of transmitted light versus the position of the dump. A second photodiode monitored the level of the incident light. Calibrated attenuators were used to maintain the signal below the saturation level for the detectors. The ratio between the energy of light transmitted past the razor blade and the energy of the incident light on the grating is shown in Fig. 5.4 versus the position of the razor blade which was actually “translated” into wavelength of the light reflected by the grating. For this case the dispersion was 1.7 \AA/mm . It was found that the rejection power of the grating increases

significantly when focussing lenses with longer focal lengths are used. No major changes were recorded when the dispersion of the grating was changed from 7 \AA/mm to 1.6 \AA/mm . When the edge approaches 532.8 \AA ($\sim 7 \text{ \AA}$ away from the center-line) the rejection factor of the probe light is better than 10^{-7} , but, it is important to mention that this “stray light rejection test” was performed close to the probe laser with only 1 mJ of energy and minimal scattering of the pulse on just the few optical elements used for the transportation of the beam. In reality, when the grating was placed within the experimental setup and the probe laser was used at full power, the rejection factor reduced significantly, mainly due to a “halo” that the probe beam acquired on all the optical surfaces that it propagate through or reflected on. This halo was blocked using the spatial filter S1 as described in Section 5.2 and the rejection factor recovered to $\sim 2 \times 10^{-7}$.

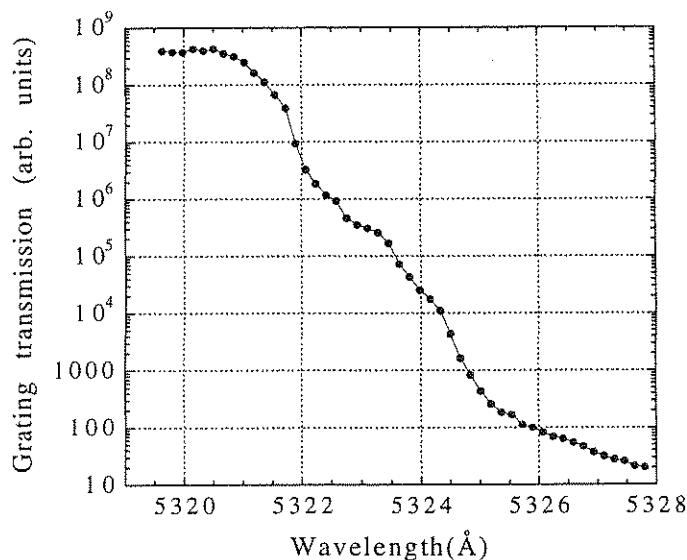


FIG. 5.4: Measurement of the stray light rejection of the 2400 grooves/mm grating used as a filter; the graph shows the ratio of the transmitted over the incident 532-nm light on the grating versus the position of the razor blade in \AA . The stray light rejection factor is better than 10^{-7} approximately 7 \AA away from the 532.1 nm .

During the experiments, after the spatial filter S1 (see Fig. 5.2), the visible pulse containing the signal and the unwanted probe light propagate in a collimated beam towards the grating. The light is dispersed in the horizontal plane in the first order of diffraction. The polarization of the beam is perpendicular to the orientation of the grooves, thus maximizing the reflectivity of the grating (up to 60%). The 1-m focal length lens, L5, is positioned approximately 10 inches after the grating to bring the probe light to a focus. At this distance, the 2-inch diameter lens collects all wavelengths within ± 5 nm around λ_{probe} . The probe light is dumped in the focal plane of the lens on a set of razor blades that is part of the spatial filter S2. The width and position of this dump determines the spectral window around λ_{probe} that is blocked. For the purpose of this TS experiment the dump was 3.5-mm wide (centered on λ_{probe}) and the probe light was attenuated by a factor of $\sim 2 \times 10^{-7}$. The parameters of the grating are summarized in Table II.

Parameter	Value
Grooves/mm	2400
Size	50×50 mm ²
Reflectivity at 532 nm	60% (p-polarized)
Incidence angle	45°
Reflection angle	33°
Order	I st
Angular dispersion	0.164 °/nm
Linear dispersion	3.5 Å/mm
Beam diameter	20 mm
Resolving power	6×10 ⁵
Stray light rejection at ±8 Å	~2×10 ⁻⁷
Damage Threshold	50 mJ/cm ² for 300 ps pulses at 1 μm

Table II. Parameters of the grating used as a spectral filter.

5.5 Detection System

The scattered light, comprised of the red and blue shifted sidebands, is collected and propagated towards the detection system. The transportation line consists of few mirrors, the field lens, and the 90° beam-rotator that is used to transform the horizontal dispersion plane defined by the filtering grating into a vertical one, to match the slit of the spectrometer. A 10-inch focal length lens is used to focus the scattered light on the slit. Different frequencies are focussed at different positions on the slit. Special care was taken with the alignment of the 90° rotator to ensure that all frequencies in the scattered

light dispersed by the filtering grating will be focussed along the 100- μm slit of the spectrometer and will pass through the slit with no significant losses.

The 640-cm focal length spectrometer (HR640, Jobin Yvon) uses a 1800-grooves/mm grating in a Czerny-Turner configuration with an aperture of $f/5.7$. The spectrometer does not normally image in the non-dispersive (vertical) direction. A cylindrical lens was added close to the exit of the spectrometer, effectively transforming the HR640 into an imaging spectrometer. Since the grooves of the HR640 grating are parallel to the input slit, this grating *again* disperses the scattered light inside the spectrometer, but this time in the horizontal plane. Therefore, due to the combined dispersive actions of the filtering grating and the HR640 grating, the spectrum at the exit of the spectrometer will be rotated with respect to the usual horizontal direction.

The output of the spectrometer is imaged onto the photocathode of a streak camera. It is important to mention that, even if the peak power of the stray light was reduced to a safe level of ~ 2 mW prior to the spectrometer, this is still enough power to saturate the photocathode of the streak camera due to space charge. To avoid saturation at λ_{probe} , an attenuation strip is set in the output plane of the HR640. The 500- μm -wide neutral-density strip reduces the stray light 10-100 times and does not affect the sidebands that are to be recorded by the streak camera.

The S-20 photocathode of the streak camera (Imacon 500, Hadland Photonics) is sensitive for the incident green light. The temporal resolution is <4 ps on the fastest sweep speed. For this experiment the camera was operated on a slower sweep speed with a resolution of ~ 15 ps. This was adequate since the overall temporal resolution was

limited by the rather large instrumental broadening given by the two uncompensated gratings present in the beam path. The phenomenon of temporal stretching of a short pulse after it encounters a grating is shown in Fig. 5.5.

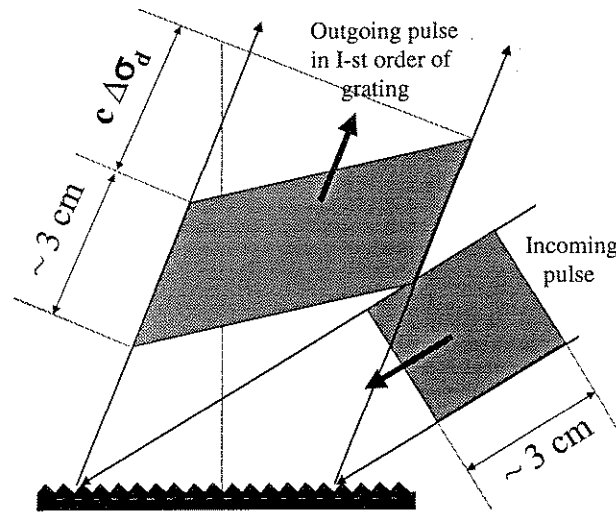


FIG. 5.5: Temporal stretching of a 100 ps long (~ 30 mm) scattered light pulse on a grating. The transverse extent of the beam is approximately 20 mm.

The temporal delay $\Delta\tau_d$ induced by a grating having N grooves/mm at a wavelength λ and operating at an incident angle i is[45]:

$$\Delta\tau_d = DN\lambda / (c \cos(i)), \quad (5.9)$$

where D is the effective diameter of the beam on the grating. Using this formula, the delay induced by the filtering grating and by the HR640 spectrometer was estimated to be approximately 85 ps and 120 ps, respectively. The total pulse broadening acquired by the scattered pulse is the result of the combined effects induced by the two gratings that have orthogonal dispersion planes. The total broadening was measured experimentally with a short 532-nm pulse (~ 20 ps FWHM) that was sent through the

spatial-spectral filter on exactly the same path followed by the scattered light. The pulse length was measured to be 20 ps with the gratings operating in the 0th order (no delay) and ~100 ps in the 1st order. We can conclude that the temporal resolution of the spectrometer-streak camera combination is $\Delta\tau \sim 100$ ps at the sweep speed used in the TS measurements.

The spectral resolution of the detection system was measured by recording the spectral lines emitted by a Ne calibration lamp. A transverse lineout through these lines showed a spectral resolution of approximately 0.5 Å when the slit was open to 100 μm. This corresponds to a bandwidth, $\Delta\nu = 5.3 \times 10^{10}$ Hz, and so the time-bandwidth product characteristic for this detection system is $\Delta\tau\Delta\nu \cong 5$.

5.6 White Light Characterization Of The Entire Optical System

As it was shown above, the optical system used to filter out the stray light and to analyze the signal is based on the dispersive properties of an etalon and two gratings. Predicting the performance of the system is not trivial even if each optical element is fully characterized and properly aligned. In addition, due the fact that the dispersive action of the filtering grating is not compensated by another optical element, only a certain spectral window of the scattered light can be transported into the imaging spectrometer without significant losses. To precisely determine the size of this spectral window, the white-light source was placed in the optical path before the first pass of the etalon to simulate the propagation of the probe beam through the entire assemblage. The

light emitted by the tungsten lamp passes through the optical system and is recorded by the streak camera operating in the time-integrated mode, just as a simple CCD camera. Fig. 5.6 (a) shows the recorded 2D image where the horizontal axis is the wavelength in nm and the vertical axis is the vertical position on the photocathode of the streak camera which is proportional to the position of the light on the entrance slit.

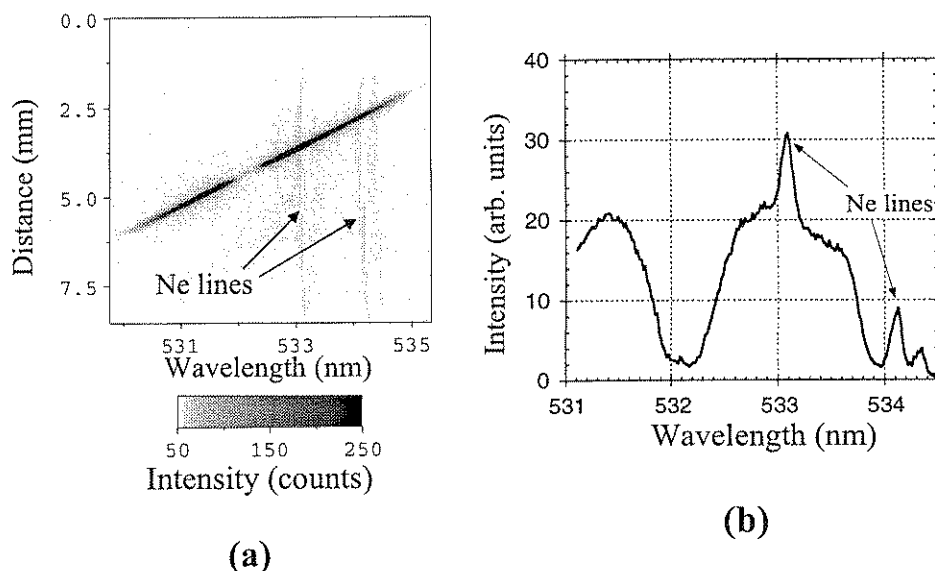


FIG. 5.6: a) Relative transmission of white-light versus wavelength as recorded by the streak camera operating as a CCD camera. The weak vertical lines, coming from a Ne lamp, are for calibration only. b) Lineout of the relative transmission of white-light versus wavelength. The plot is obtained by summing the 2D data in (a) vertically in a region of interest around 532.9 nm (the first red-shifted sideband).

The weak vertical lines in the right side of the image are coming from the Ne lamp that was placed in the beam path just before the spectrometer so as to fill the slit vertically. The Ne lamp was introduced for wavelength calibration purposes only. The spectrum of the white-light lamp is tilted because of the combined actions of the two gratings that

have orthogonal dispersion planes, as it was discussed in Sec. 5.5. The transmission minimum situated around 532.1 nm is due to the 3-pass etalon. By summing the 2-D data in Fig. 5.6 (a) vertically, the curve of the relative transmission of the scattered light versus wavelength is obtained and is shown in Fig. 5.6 (b).

For this measurement, the size of the transport optics, particularly the field lens, limited the collected bandwidth to that seen in Fig. 5.6 (b). However, this was sufficiently wide to collect the $\pm 8 \text{ \AA}$ shifted sidebands, $\lambda_{\text{blue}}=531.3 \text{ nm}$ and $\lambda_{\text{red}}=532.9 \text{ nm}$. Figure Fig. 5.6 (b) shows that both of these wavelengths are propagated up to the streak camera with similar efficiencies. By increasing the size of the transport optics, the maximum spectrum successfully collected was $\pm 22 \text{ \AA}$ around λ_{probe} . Thus, at least two sidebands generated in the scattering process on both the blue and the red side of the probe wavelength can be collected and transported by the optical system. This complex optical filter introduces ~ 10 times losses for all frequencies.

The attenuation of the stray light induced by the etalon in the 3-pass geometry appears to be in Fig. 5.6 (b) only ~ 10 times as opposed to 1000 times as it was previously measured. The difference is due to the slight misalignment of the white-light source, which, being a polychromatic source, cannot be aligned with the same precision as the very well collimated, monochromatic probe beam in the 3-pass geometry for the etalon. Nonetheless, the information in Fig. 5.6 is extremely useful in the modeling of the transmission of the wavelengths of interest. For this measurement, the spatial filter S2 was disabled by removing the beam dump that stops the 532-nm light. When S2 is active, the signal recorded by the streak camera at this wavelength goes down to the

noise level while no change in the transmission of the sidebands is observed. Due to the high extinction ratio of the filtering grating, precise measurements of the optical transmission using the weak white-light source and the streak camera (which has a rather small dynamic range) are not possible.

Chapter 6

Experimental Results

6.1 F/3 Collinear Thomson Scattering

To demonstrate the applicability of the collinear TS technique towards the characterization of the RPWs, the interaction chamber was filled with Hydrogen, Ar or He. The plasma density was varied from $2 \times 10^{15} \text{ cm}^{-3}$ to $1.4 \times 10^{17} \text{ cm}^{-3}$ by varying the pressure of the gas fill in the interaction chamber. A typical signal on the streak camera representing the frequency and time-resolved sidebands generated in the scattering process at resonance (in He) with the f/3 focussing geometry is shown in Fig. 6.1.

The streak record shows spectral features having two distinct time scales. The three long streaks represent the residual leak of the probe light at λ_{probe} and the two sidebands situated approximately $\pm 6.5 \text{ \AA}$ away from the center-line, which are generated in the cavity of the probe laser. These features are always present in the spectrum of the scattered light, even when there is no plasma in the target chamber, and are thus not connected with the TS process. Their presence in the experiment can be diminished using additional masks or neutral density filters in filter S2 without affecting the

propagation of the sidebands, since this stray light does not affect the reading of the signal while it offers some information about the intensity of the probe laser pulse.

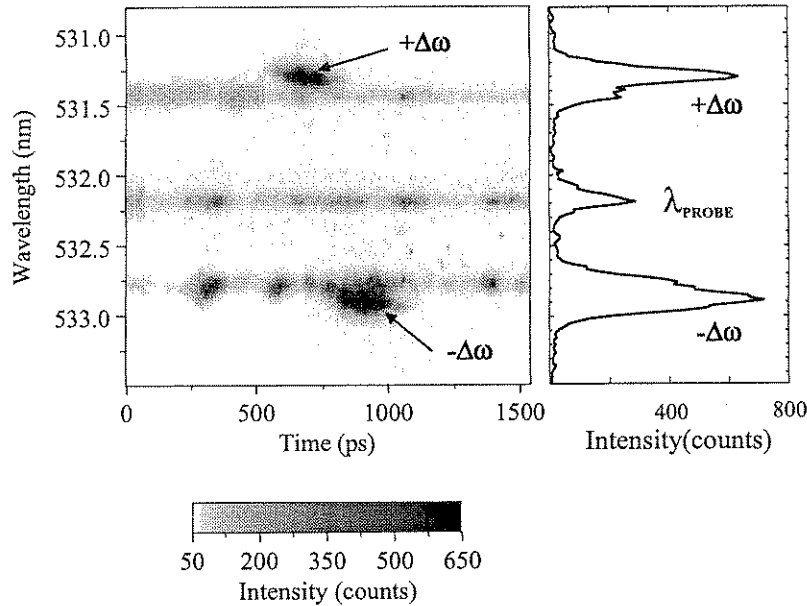


FIG. 6.1: Red and blue shifted sidebands generated by collinear TS of the 532.1-nm probe pulse on the RPW in He (He^{1+}) at 322 mTorr. The CO_2 pulse was $f/3$ focussed to an intensity of approximately 10^{15} W/cm^2 . The three lines in the streak record that temporally stretch from the beginning to the end of the streak are not a result of the scattering process (see text). The right-hand curve represents a lineout through the sidebands.

The short, picosecond-time-scale sidebands shifted with $\pm 8.1 \text{ \AA}$ away from the wavelength of the probe light are the result of scattering from the RPW. Note that these two sidebands are actually coincident in time but appear shifted for the same reason that the white light spectrum was tilted in Fig. 5.6 (a), i. e., the uncompensated dispersion of the filtering grating. The power of the scattered light, $P_s/P_0 \cong 2 \times 10^{-8}$, is roughly equal in each sideband, as expected from the scattering process. The 8.1-\AA separation between these features and the wavelength of the probe pulse corresponds exactly to the $\Delta\omega$ separation between the two frequencies of the CO_2 pulse. The streak shown in Fig. 6.1

was obtained in He at 322 mTorr at a corresponding plasma density $n \cong 10^{16} \text{ cm}^{-3}$. At this density, $\Delta\omega = \omega_p$ and the RPW excitation is resonant. The frequency of the RPW, given by the separation of the sidebands, is therefore either $\Delta\omega$ or ω_p . The amplitude of the wave was estimated from the absolute amount of scattered light to be 2-4% (for an interaction length in the He^{1+} plasma of slightly less than 1 mm).

RPWs were also excited when the plasma density was slowly dropped below $n_{\text{res}} = 10^{16} \text{ cm}^{-3}$. The intensity of the sidebands decreased until the plasma density reached $\sim 10^{15} \text{ cm}^{-3}$, at which point the signal became undetectable by the streak camera.

The TS becomes more efficient when the plasma density is higher than 10^{16} cm^{-3} due to the increased number of electrons participating in the scattering process. Figure 6.2 shows the sidebands generated in He at $n = 6 \times 10^{16} \text{ cm}^{-3}$. The first (fundamental) and the second harmonics are clearly visible, on both the red and the blue side of λ_{probe} . The fundamentals are optically attenuated 10 times in the imaging spectrometer and they are ~ 30 times stronger than the second harmonics. On the red side, even the third harmonic is visible, although its intensity is very weak. The frequency of the RPW is still $\Delta\omega$, which this time is different than ω_p , $\Delta\omega = 0.4\omega_p$. Figure 6.2 also shows the capability of the optical system to filter and collect the first two harmonics without significant losses as it was discussed in Chapter 5 (the transmission of the red-shifted side was deliberately set higher than that of the blue side to allow the collection of the third harmonic for the shot shown in Fig. 6.2).

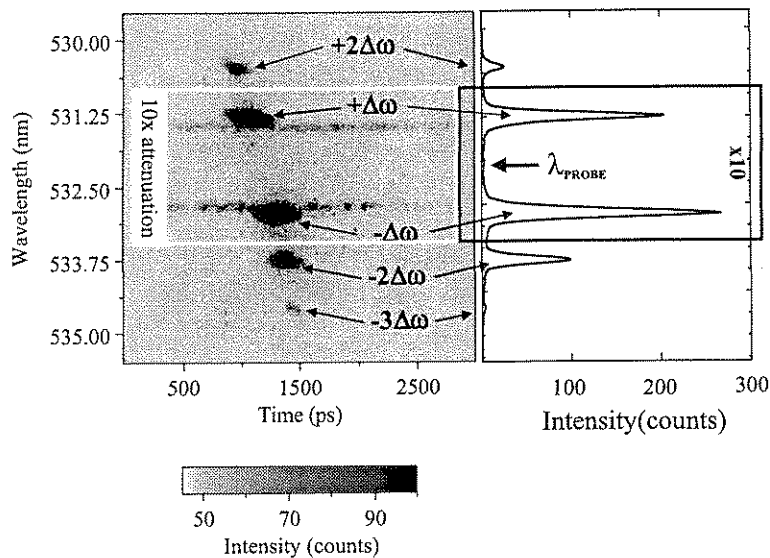


FIG. 6.2: Sidebands produced through collinear TS in He at 1.7 Torr of filling gas pressure, approximately 6 times above resonance ($\Delta\omega=0.4 \omega_p$). The intensity of the CO₂ laser pulse ($f/3$) was $\sim 1.5 \times 10^{15} \text{ W/cm}^2$. Two blue-shifted and three red-shifted sidebands can be seen separated with $\sim 8 \text{ \AA}$, characteristic of $\Delta\omega$. The stray light at 532.1 nm has been reduced below the detection threshold of the streak camera. The right-hand curve represents a lineout through the sidebands.

Temporally, the sidebands are short lived, their duration being approximately 150 ps (FWHM). As mentioned before, the temporal broadening introduced by the TS setup does not allow the resolving of phenomena faster than 100 ps. Therefore, it can only be concluded from Figures 6.1 and 6.2 that the duration of the plasma wave is shorter or comparable to the duration of the CO₂ laser pulse. The plasma wave decays significantly, below the detection threshold for the streak camera, after the action of the infrared pulse on the plasma is over. Similar TS results were obtained in H₂ and Ar.

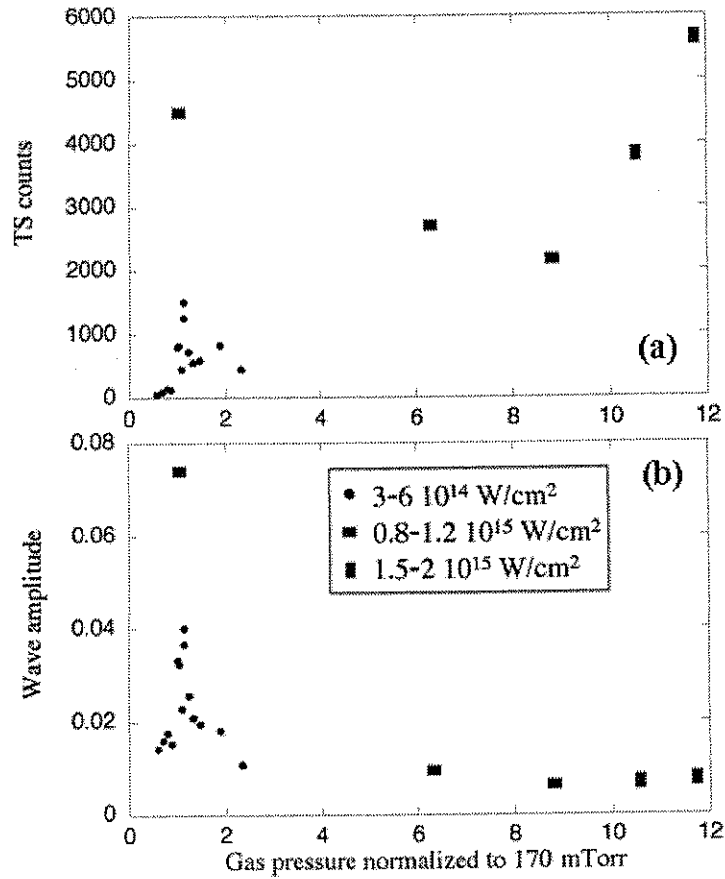


FIG. 6.3: (a) The number of counts in the first red-shifted Thomson scattering sideband versus the gas pressure in the interaction chamber normalized to 170 mTorr; (b) the plasma wave amplitude obtained from (a) versus the normalized pressure.

Figure 6.3 (a) shows the number of counts recorded in the first red-shifted TS sideband as a function of the gas pressure in the interaction chamber normalized to 170 mTorr, value that is considered the resonant pressure from the measured frequency shift of the SRS plasma waves (see Fig. 5.1, Chapter 5). The data is extracted from figures like Fig. 6.1 and Fig. 6.2 for three different sets of shots, depending on the power of the laser pulse. Figure 6.3 (b) shows the wave amplitude that has been obtained from Fig. 6.3 (a) by using the reversed TS efficiency formula (Eq. 5.3):

$$\varepsilon = \frac{2}{\pi} \frac{n_{\text{crit}}}{n} \frac{\lambda_{\text{pr}}}{L} \sqrt{\frac{P_s}{P_0}}, \quad (6.1)$$

where n_{crit} is the critical density corresponding to the probe wavelength, λ_{pr} . The horizontal axis can be interpreted as the normalized plasma density, but, since the transverse ponderomotive force of the laser pulse constantly changes the plasma density, it becomes difficult to define a “resonant” pressure for a real, dynamic 3-D system. The maximum TS signal is recorded at 190-200 mTorr, slightly above the 170 mTorr of gas pressure that corresponds to a $9.4 \times 10^{15} \text{ cm}^{-3}$ resonant density. This discrepancy appears because the plasma wave is strongly driven by the CO_2 pulse at its peak power at resonance only after the plasma density decreased to n_{res} during the rising edge of the pulse. For $3 \times n_{\text{res}} < n < 12 \times n_{\text{res}}$, the amplitude of the plasma waves was observed to be approximately constant at around 1% (CO_2 laser pulses with different intensities were used, see Fig. 6.3 (b)). Since P_s is proportional to $(\varepsilon n)^2$, the background plasma density n becomes important for detection purposes. For $n \gg n_{\text{res}}$, even if the amplitude of the RPW is rather small, the recorded P_s is actually significant due to the increased number δn of electrons in the wave. The opposite happens for the $n < n_{\text{res}}$ side where P_s decreases rapidly below the detection threshold. The interaction length L used in Eq. 6.1 was taken to be equal to the Rayleigh range of the CO_2 laser beam, $L=1.5 \text{ mm}$, and n , the plasma density corresponding to the fully ionized neutral density.

The power of the light scattered in the sidebands at $n \gg n_{\text{res}}$ is approximately the same (slightly larger if we consider the shots with similar CO_2 laser pulse power) with

that scattered around resonance, see Fig. 6.3 (a). Regardless of the plasma density, P_s can be related to the amplitude of the longitudinal electric field E_x associated with a RPW that is given by the Poisson's equation, $E_x = 4\pi\delta n$. Since $P_s \sim (\delta n)^2$, the result is that the electric field is proportional with the square root of P_s , $E_x \sim \sqrt{P_s}$. That means, the electric fields that can be used to accelerate electrons at $n = n_{res}$ and at $n \gg n_{res}$ are approximately the same, even if the non-resonant plasma wave amplitude is small. In other words, the reason for why there are similar P_s values at resonance and off-resonance, $\delta n = \epsilon \times n$, can also be used to infer the equality between the electric fields at both $n = n_{res}$ and $n \gg n_{res}$.

2-D simulations were performed with input laser and plasma parameters close to those at which few well-documented experimental shots were undertaken. The plasma wave amplitude ϵ_{exp} resulting from the TS measurements are compared to the similar (trajectory-averaged) quantity ϵ_{sim} resulting from the simulations. Figure 6.4 shows both ϵ_{exp} and ϵ_{sim} as a function of the normalized pressure of the gas (or, equivalently, the normalized plasma density). A good agreement can be observed for the non-resonant shots. For the resonant shot the simulation seems to indicate that the wave amplitude is larger than that measured in the experiment. This discrepancy can be explained if the response time of the TS diagnostic is taken into account. It is possible that, at resonance, the wave amplitude is in fact larger than the 7% measured in the experiment for a period of time of less than 100 ps (a spike). In this case, the TS diagnostic system integrates the signal over its response time of 100 ps and the ϵ_{exp} appears to be smaller than the exact amplitude of the wave. It is important to mention that the scattering process is

susceptible to detuning between the RPW and the probe beam, the same way as with the detuning between the wave and the CO₂ driver, see Chapter 4. However, as shown in Chapter 4, the non-resonant excitation is susceptible to these effects to a much lesser extent, which explains a better agreement between the experiment and the simulations.

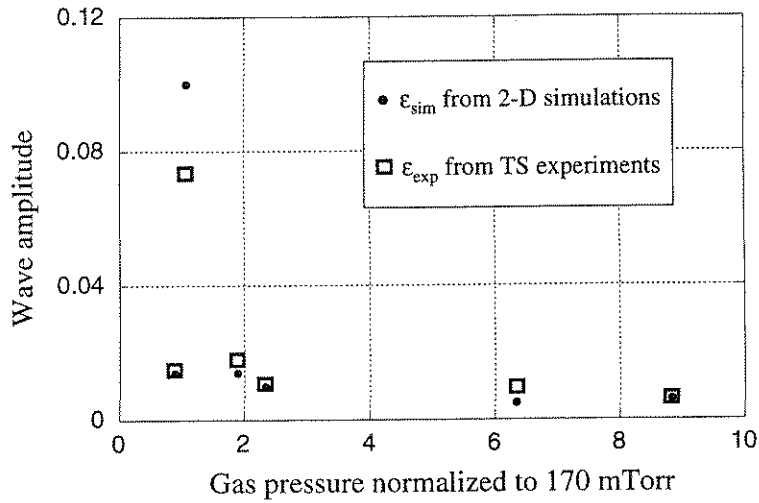


FIG. 6.4: The plasma wave amplitude for six selected shots as resulting from the TS measurements, ϵ_{exp} , and from the 2-D simulations, ϵ_{sim} , versus the pressure of the fill gas normalized to 170 mTorr.

An example of a RPW that can have a high amplitude for just few tens of picoseconds at resonance is shown in Fig. 6.5 that shows the frequency and time-resolved TS spectrum for a 10^{15} W/cm² shot taken in 195 mTorr of H₂.

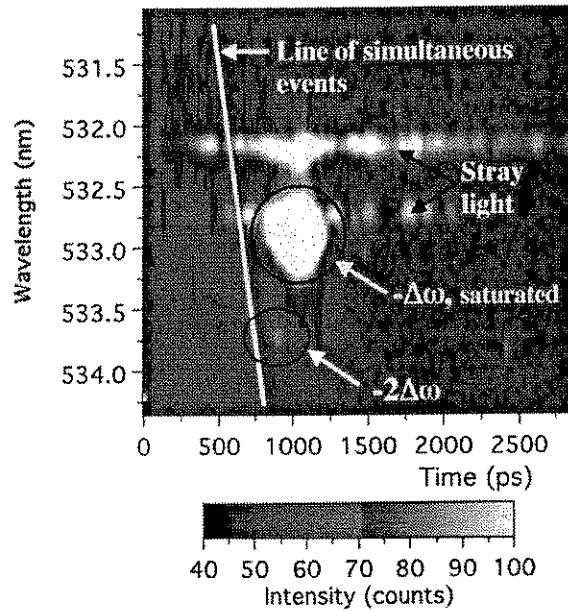


FIG. 6.5: The red-shifted sidebands, $-\Delta\omega$ and $-2\Delta\omega$, produced by collinear TS in 195 mTorr of hydrogen.

For this shot, only the first ($-\Delta\omega$) and the second ($-2\Delta\omega$) red-shifted harmonics were collected and streaked. Figure 6.6 shows the temporal lineouts for each sideband with the delay introduced by the TS diagnostic system being compensated for. The first harmonic, lasting for more than 200 ps, is very intense and saturated the photocathode of the streak camera.

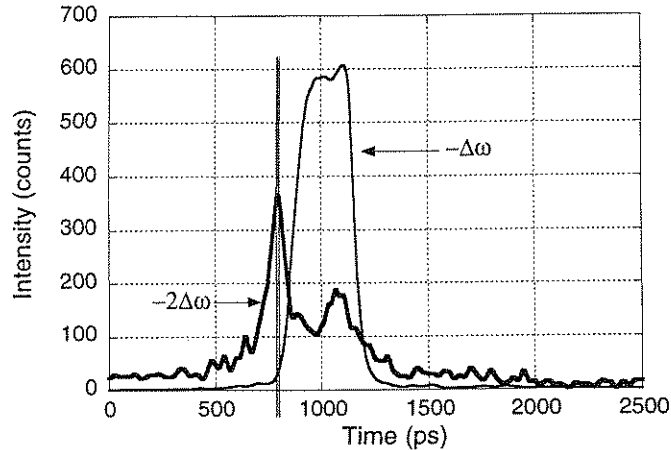


FIG. 6.6: Temporal lineouts of the first (thin line) and the second (thick line) red-shifted harmonics shown in Fig. 6.5. The approximately 103 ps time delay introduced by the TS diagnostic system is removed. The vertical line marks the time when the second harmonic signal is maximum. The intensity of the second harmonic was multiplied by 20 for visualization purposes.

The second harmonic is much weaker and has a much shorter duration of ~ 50 ps (only the initial burst is considered, the second part of the signal is just light coming from the saturated first harmonic). It is possible that the $-2\Delta\omega$ signal is produced just for the time when the amplitude of the RPW is very high. The 100-ps response time of the TS system broadens the light pulses scattered in both sidebands in such a way that the peak of the second harmonic appears on the rising edge of the first harmonic. Only the highest intensity part of the $-2\Delta\omega$ signal is though recorded, the rest being below the noise level of the streak camera. Therefore, for this particular shot, the second harmonic signal appears to be shorter than the response time of the TS system of ~ 100 ps. Other similar shots performed around the resonant density also show that the $-2\Delta\omega$ signal is generally shorter and tends to appear earlier than the $-\Delta\omega$ signal. The shots taken at $n \gg n_{\text{res}}$ do not show the same behavior. The second harmonic signals are generally longer and follow the first harmonic. This would imply that the light recorded at $-2\Delta\omega$

and $-3\Delta\omega$ by the streak camera is mostly produced by the probe beam which scatters off a wave with frequency $\Delta\omega$ and not due to the scattering process from a RPW with frequency $2\Delta\omega$ or $3\Delta\omega$. The exact answer to this question could be offered by a modified TS diagnostic system for which, by compensating for the dispersion of the grating used to filter-out the stray light, the resolution can be improved to less than 20 ps.

The TS process on the RPW is probably not the only way to excite the observed sidebands. A four-wave-mixing phenomenon in the gas surrounding the plasma can also participate in the generation of these new frequencies[46]. The intensity of the scattered light produced by this mechanism is much smaller than the intensity of the TS generated sidebands. No scattered light was recorded when the power of the two-frequency CO_2 pump pulses was just not high enough to ionize the gas. Also, the difference in the third-order nonlinear susceptibility for the three gases studied in this experiment, He, H_2 and especially Ar, is expected to produce significant differences in the intensity of the scattered light for each gas. For example, the third-order nonlinear susceptibility for Ar is approximately 20 times larger than that of He[47,48], a fact that would make the sidebands generated in Ar around 400 times stronger than those generated in He. This difference is not observed in the experimental results that show similar levels of intensity of the scattered light for all three gases under study. In addition, when the power of the laser pulse was increased, the TS signal increased significantly, up to 20 times. This would not be expected in the case of a four-wave-mixing process happening in the gas that exists outside the plasma because the intensity of the pulse was not high

enough to ionize it. More powerful pulses create the plasma earlier (in space and time) and do not really increase the length over which the gas is present. Moreover, when the plasma density was brought below n_{res} , the TS signal decreased dramatically, faster than what one would expect from a $\chi^{(3)}$ process where the intensity of the scattered light is $\sim n^2$. For example, the TS signal was 4500 counts at ~ 200 mTorr of H_2 , see Fig. 6.3 (a), and it dropped below the detection threshold of 10 counts at 100 mTorr, clear sign of the enhancement of the scattering process close to the resonant density. We can conclude that, at least in the density range for these measurements, the probe light scattered into sidebands is only a result of the collinear TS process on the beat-wave excited RPW.

The results from the collinear TS measurements show that RPWs are excited both at resonance and off resonance by the TW CO_2 laser pulse focused in the $f/3$ geometry. The wave amplitude ϵ_{exp} extracted from these measurements is in good agreement with the ϵ_{sim} from the 2-D simulations, especially for the non-resonant shots. Therefore, we use the simulation results to extract the maximum value of the trajectory-averaged electric field generated by these waves. This value is ~ 10 MV/cm for the most powerful experimental shots that generally have $a_1=0.1$ and $a_2=0.2$ taken around the resonant density. Given the short interaction length of ~ 2 mm, it means that the injected electrons will gain approximately 2 MeV of energy.

The experimental observation of the accelerated electrons when the RPWs were excited using the $f/3$ focussing optic proved to be difficult due to the small focal spot leading to strong transverse fields and the imperfect matching of the e-beam

($\sigma_{rms}=150 \mu\text{m}$) into the 100- μm accelerating structure of the RPW. A 2-D simulation performed at resonance for an intense laser pulse with $a_1=a_2=0.2$ and a spot size of $w_0=50 \mu\text{m}$ showed that transverse electric fields of up to 12 MV/cm are excited in the plasma. Figure 6.7 presents a snapshot of the transverse E_y field associated with the RPW from that simulation.

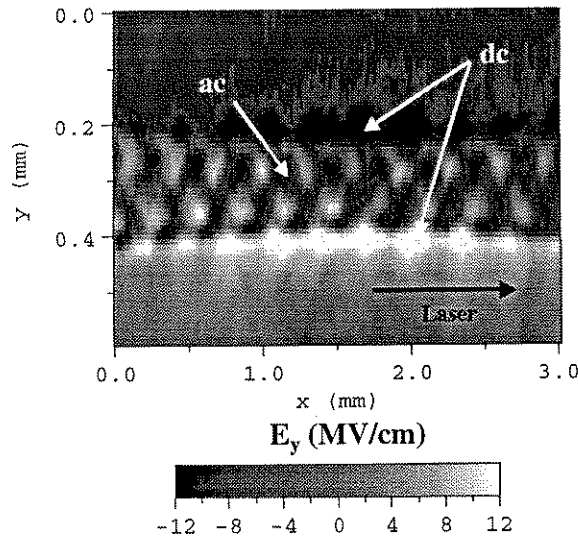


FIG. 6.7: Snapshot of the transverse electric field E_y associated with the plasma wave excited at resonance from the 2-D simulation results. The 2-D image is recorded when the peak of the laser pulse reaches the focal plane situated at $x=1.5 \text{ mm}$. The simulation parameters are: spot size $w_0=50 \mu\text{m}$, $a_1=a_2=0.2$.

The field has two components, one that is constant in time (dc), and another that is oscillating and relativistic (ac). The first one is created at the plasma boundary by the electrons that are pushed out of the plasma by the ponderomotive force of the laser pulse. The second one is due to the density perturbations within the plasma, close to the axis of the laser pulse. The latter one is also due to the ponderomotive force of the laser pulse. Similar results were obtained when the excitation was non-resonant. The E_y fields

are positive if they are oriented in the positive direction of the y-axis and negative if otherwise. During the electron injection experiments, these transverse electric fields significantly increased the transverse size of the e-beam thus hindering the measurements of the longitudinal fields associated with the RPWs excited in the plasma. Therefore, the electron injection experiments were continued with the f/18 focusing arm because of the larger spot size and a longer interaction length, together with the TS measurements.

6.2 F/18 Collinear Thomson Scattering And Electron Injection

The f/18 TS measurements were performed with the same optical filter used for the f/3 case that was described in detail in Chapter 5. The only difference was the scattering geometry in the interaction chamber. A schematic of the optical arrangement that was used to co-propagate the probe and the 10- μm beams was shown in the inset of Fig. 5.2. This time, the RPWs were probed by a doughnut-shaped beam. This influenced the rejection factor of the etalon that reduced slightly more than 10 times. It was therefore necessary to use a 100x neutral density filter in the HR-640 spectrometer (instead of a 10x one) to reduce the intensity of the light at λ_{probe} below the saturation level of the photocathode of the streak camera. The intensity of the CO_2 pulse is up to $8 \times 10^{14} \text{ W/cm}^2$ and the plasma wave resembles more the profile of a plane wave. RPWs are excited in these conditions only in H_2 , both at resonance and off resonance.

Figure 6.8 shows the frequency and time-resolved streak camera images for two shots, one at resonance, Fig. 6.8 (a) in 160 mTorr of H_2 , and the other off resonance, Fig. 6.8 (b) in 373 mTorr of H_2 . Due to the added degree of complexity introduced by the doughnut-shaped probe beam, only the first red-shifted sideband was recorded in the $f/18$ TS experiments. The intensity of the light scattered in this sideband P_s depends not only on the amplitude of the wave, but also on the position along the plasma where the probing is done, because, as opposed to the $f/3$ TS measurements where the probe beam sampled the entire plasma, in the $f/18$ case the probe beam samples only approximately 1.5 mm of the 3-cm long plasma. Figure 6.8 (b) shows that RPWs having a frequency $\Delta\omega$ and a wavenumber Δk can be excited off resonance using the $f/18$ arm of the laser system. Extensive $f/18$ TS measurements at higher plasma densities could not be attempted due to powerful back-scattering of the laser pulse on non-relativistic waves that are excited in the plasma, see Appendix C. The back-scattered laser light is reflected back into the large aperture amplifier and amplified above the damage threshold for the optics used to transport the CO_2 beam.

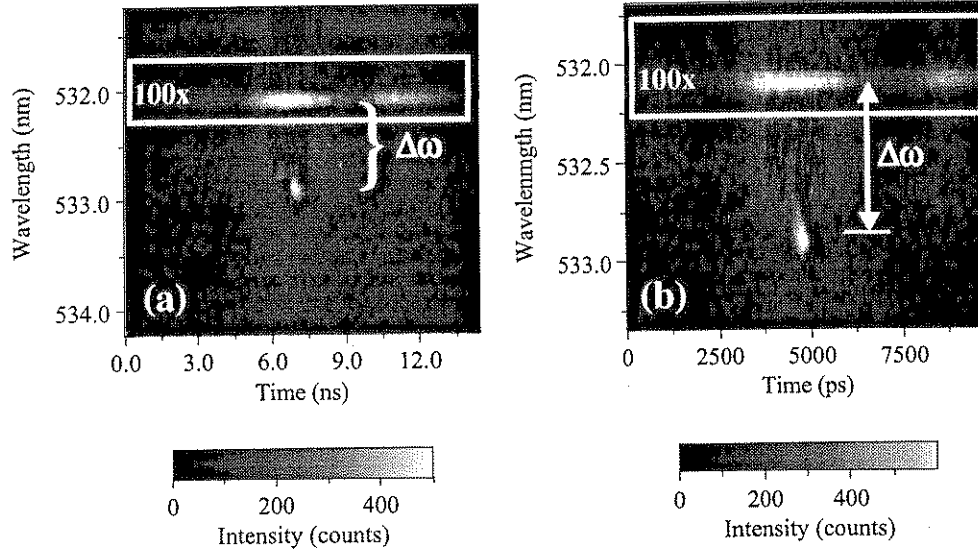


FIG. 6.8: Streak images of the red-shifted Thomson scattered light for two $f/18$ shots in hydrogen, (a) at resonance (160 mTorr) and (b) off resonance at $n=2.4 \times n_{\text{res}}$ (373 mTorr). The frequency separation between the red-shifted sideband and the probe light corresponds to a $\Delta\omega$ shift for both cases.

The wave amplitude from this non-resonant shot was estimated from the total amount of scattered light to be $\epsilon_{\text{TS}} \approx 0.6\%$. The corresponding longitudinal electric field E_x would then be ~ 2 MV/cm in the 1-D approximation. 2-D simulations for the $f/18$ TS shots were performed at laser parameters similar with the experimental ones. The wave amplitude for the same non-resonant shot at $n=2.4 \times n_{\text{res}}$ was approximately two times smaller than that predicted by the TS measurements, $\epsilon_{\text{sim}} = 0.3\%$. The difference could be attributed to few factors. First, as mentioned above, the $f/18$ TS measurements are less precise compared to the $f/3$ ones due to a more complicated scattering setup. Second, these measurements reveal the information about some local value of the wave amplitude with a 100-ps response time. Third, the simulation results for the $f/18$ case are difficult to analyze due to the very small amplitude of the waves excited in a noisy background. Various Fourier transform techniques were employed to extract the values

of the ϵ_{sim} from the output of the code. These techniques could underestimate the wave amplitude due to their space-averaging nature. Overall, the f/18 TS measurements proved the existence of the non-resonantly excited RPWs.

The magnitude of the electric fields associated with both the resonant and the non-resonant RPWs was determined from the electron injection measurements. Details of the experimental setup were presented in Chapter 4. Figure 6.9 shows the electron spectrum for the two-frequency shot #11999 taken in 497 mTorr of H_2 . The single-shot spectrum is composed of the data obtained from the fluorescent screens (first four dots from 12 MeV to 15 MeV included) and the data from the surface barrier detectors, next four dots, 17 MeV to 28 MeV. The inset of Fig. 6.9 shows two images of the electron beam on the fluorescent screens after it went through the plasma and the spectrometer. The top image shows the unperturbed electron beam for a single-frequency shot with plasma taken at the same plasma density with the two-frequency shot shown on the bottom image. As expected, the single frequency shot shows only the injected electron beam at 12 MeV, whereas the beat-wave shot shows a decrease in the number of incident electrons at 12 MeV and accelerated electrons on the more sensitive screen.

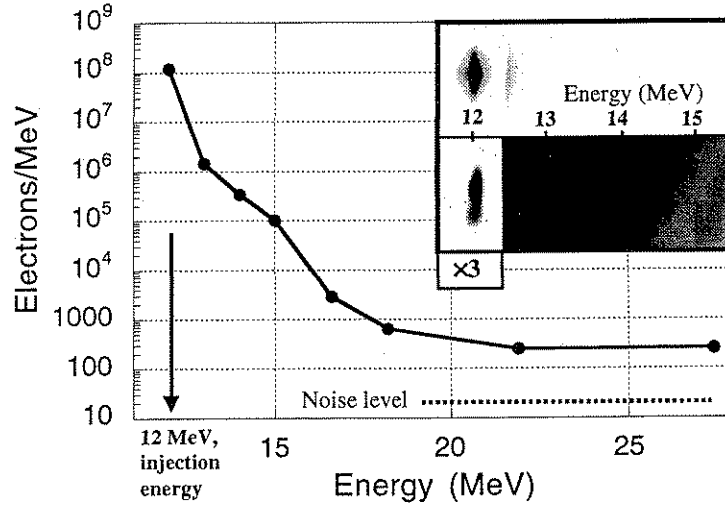


FIG. 6.9: The spectrum of the accelerated electrons for a two-frequency shot with plasma in H_2 at $n=3.3 \times n_{res}$. The CO_2 laser pulse was focused with $f/18$ optics. The inset shows the image of the electron beam on the two fluorescent screens covering an energy interval of 12-15 MeV (top image shows the electron spectrum for a single frequency shot with plasma and the bottom for the two-frequency shot).

Electrons with a maximum energy of up to 28 MeV, i.e., an overall energy gain of 16 MeV (approximately 2.5 times less than the gain obtained at resonance[49]), were seen. Therefore, the non-resonantly excited RPWs produced an average E_x of 4 to 8 MV/cm if an interaction length of 4 to 2 cm is assumed. The amplitude of the plasma wave was also estimated to be 1-2 % from the 2-D simulations performed at the laser parameters close to the ones used in these electron injection experiments. The corresponding electric fields are approximately 6 MV/cm as computed from the simulations.

Overall, the TS measurements show that the small-amplitude, non-resonant RPWs are excited by the two-frequency laser pulse propagating in plasma. The results from the electron injection experiments suggest that, even if the amplitude of these waves is rather small, the electric fields associated with them have significant magnitudes. This is due to the increased background plasma density that enhances the density perturbation δn .

Chapter 7

Conclusions

Controlled, mono-energetic acceleration of externally injected electron bunches in plasmas by relativistic plasma waves represents the fundamental goal for the second generation of plasma accelerators. This kind of acceleration is also the main subject of this dissertation. 2-D simulations and experiments are used to explore the present possibilities to achieve mono-energetic acceleration in a laboratory. The Neptune laboratory in UCLA, with its combination of a TW laser system and a picosecond electron gun, is probably the principal contender to demonstrate it.

A microscopic picture of the beatwave excitation process of a RPW is discussed in Chapter 2 starting from the trajectory of a free electron in the field of a plane electromagnetic wave (or a laser pulse). 2-D simulations are used in Chapter 3 to extensively analyze the beatwave excitation process for both resonant and non-resonant plasmas. The computer modeling is specifically used to study the phase relationship between the RPW and the beat pattern of the driving pulse, from the point of view of an externally injected electron that is phase-locked with the laser pulse. It is found that the

phase between such an electron and the resonant plasma waves is very susceptible to small changes in parameters like the plasma density, laser pulse rise time and amplitude. While such a resonant wave can produce very high accelerating gradients, the precarious stability of its phase and its phase velocity makes mono-energetic acceleration of a series of electron bunches a very difficult task. The results from the 2-D simulations performed at plasma densities much higher than the resonant density show that RPWs having the same frequency and wave number as the beat pattern of the pump laser pulse are excited. The phase velocity of these waves is equal to the group velocity of the laser pulse in the plasma and is, therefore, constant and nearly independent of the spatial and temporal variations of the plasma density. These plasmons are always phase-locked with respect to the driving electromagnetic beat wave, which in turn makes them well suited for the acceleration of phased-locked electrons. Experimentally, such waves have been excited over a wide range of plasma densities using the TW CO₂ laser system described in Chapter 4 and detected using a novel collinear Thomson scattering diagnostic system detailed in Chapter 5. The key part of this diagnostic is a novel spatial-spectral filter that is utilized to simultaneously attenuate the probe light $\sim 10^9$ times and collect the weak scattered light which is shifted 3–24 Å from the probe wavelength. The amplitude $\delta n/n$ of these waves has been inferred from the intensity of the scattered light and then shown to be in good agreement with the results from the 2-D simulations. Although the amplitude of these waves is relatively smaller than that at resonance, the longitudinal electric fields associated with them can be quite significant (100s of MV/m), depending on the

intensity of the laser pulse. This is because of the elevated background plasma density that contributes to a significant δn . Accelerating gradients of 400-500 MeV/m are directly inferred from the energies gained by the injected electrons. The results from both the TS measurements and the electron injection experiments were presented in Chapter 6.

The experimental evidence of the excitation and existence of the non-resonant RPWs and its associated electric fields represents a step forward towards the goal of phase-locked, mono-energetic acceleration. Operation at an elevated pressure might offer some advantages when higher non-resonant acceleration gradients are sought, like the decrease in the self-focusing threshold (see Appendix D) and easier guiding. The recent creation of sub-picosecond electron bunches in the Neptune laboratory could be conjoined with the excitation of longer wavelength RPWs (by modifying the CO₂ lines) to make the acceleration of phase-locked electrons a project on the agenda of the Neptune laboratory. In such a case, serious attention has to be given to concurrent phenomena like the ionization induced refraction, strong transverse fields and beam loading, just to name a few.

Appendix A

Motion Of A Free Electron In The Field Of A Plane EM Wave

Let's consider the case of a plane electromagnetic (EM) wave that interacts with a free electron. Figure A.1 defines the geometry of the interaction process with the electron initially placed at rest in vacuum at the (0,0,0) position. The electric field is linearly polarized so that:

$$\mathbf{E} = \hat{y}E_0\text{Cos}(kx - \omega t), \quad (\text{A.1})$$

where ω and k are the frequency and the wavenumber of the EM wave and $\omega=ck$.

Using:

$$-\nabla \times \mathbf{E} = \frac{1}{c} \frac{\partial \mathbf{B}}{\partial t}, \quad (\text{A.2})$$

the magnetic field \mathbf{B} can be determined. Thus, we obtain:

$$\mathbf{B} = \hat{z}E_0\text{Cos}(kx - \omega t), \quad (\text{A.3})$$

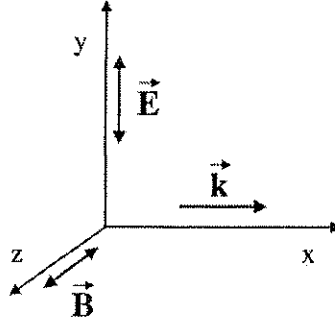


Fig. A.1. Geometry of interaction between a free electron initially at rest at $x=y=z=0$ and a plane EM wave.

Therefore the wave is moving in the x direction with the electric field in the y direction and the magnetic field along z . The Lorentz equation of motion is:

$$\frac{d\mathbf{p}}{dt} = -e(\mathbf{E} + \mathbf{v} \times \mathbf{B}), \quad (\text{A.4})$$

where we consider $e=+1.6 \times 10^{-19}$ C the positive value of the electron charge and \mathbf{v} is the velocity of the particle. The momentum of the electron, \mathbf{p} , is defined as $\mathbf{p} = m_0 \gamma \mathbf{v}$, with γ being the relativistic Lorentz factor:

$$\gamma = 1 / \sqrt{1 - \frac{v^2}{c^2}}. \quad (\text{A.5})$$

It is important to mention that in this treatment the electron is considered relativistic at all times, that is, no previous or ulterior assumption is made on the strength of the EM wave. Eq. A.4 written along the y and x coordinates, becomes:

$$\frac{dp_y}{dt} = -eE_y \left(1 - \frac{v_x}{c}\right) \quad (\text{A.6})$$

$$\frac{dp_x}{dt} = -eE_y \frac{v_y}{c}, \quad (\text{A.7})$$

where the indexes on the subscript represent projections of the respective quantities on the axes x or y. If we multiply Eq. A.4 with v and then use the following identity:

$$\mathbf{v} \frac{d\mathbf{p}}{dt} = \frac{d(\gamma m_0 c^2)}{dt} \quad (\text{A.8})$$

we obtain the first constant of motion. This can be expressed as:

$$\gamma m_0 c - p_x = \text{const.} \quad (\text{A.9})$$

To derive another (second) constant of motion, we first introduce the vector potential from $\mathbf{E} = -1/c(\partial\mathbf{A}/\partial t)$ as:

$$\mathbf{A} = \hat{y} \frac{cE_0}{\omega} \text{Sin}(kx - \omega t). \quad (\text{A.10})$$

From Eq. A.10 we can derive:

$$\frac{\partial A_y}{\partial x} = E_y. \quad (\text{A.11})$$

Using:

$$\frac{dA_y}{dt} = \frac{\partial A_y}{\partial t} + v_x \frac{\partial A_y}{\partial x} \quad (\text{A.12})$$

in combination with Eq. A.6 we obtain the second constant of motion:

$$p_y - \frac{e}{c} A_y = \text{const.} \quad (\text{A.13})$$

Initially, at $t_0=0$, $p_y=0$ and so is $A_y=0$. Then, we suddenly “turn on” the EM wave over the electron. Therefore, since A_y is known, we can determine p_y :

$$p_y = \frac{e}{c} A_y. \quad (\text{A.14})$$

Similar initial conditions set for Eq. A.9 result in:

$$\gamma m_0 c - p_x = m_0 c. \quad (\text{A.15})$$

Coupling A.15 with the identity $\gamma^2 = 1 + (p_x^2 + p_y^2)/(m_0 c)^2$, p_x becomes:

$$\frac{p_x}{m_0 c} = \frac{p_y^2}{2 m_0^2 c^2} = \frac{1}{2} \frac{e^2 A_y^2}{m_0^2 c^4}. \quad (\text{A.16})$$

Equations A.14 and A.16 are very important in the understanding of the motion of the electron. Since A_y has a sinusoidal behavior, from A.14 results that the electron will have a “quiver” motion on the y axis. The time-averaged value of the y -momentum, $\langle p_y \rangle$, is though null, $\langle p_y \rangle = 0$. That means there is no overall “drift” in the y direction. Not the same is valid for the x -momentum. Eq. A.16 shows that p_x is always positive, regardless of the value of A_y . We can rewrite Eq. A.16 as:

$$\frac{p_x}{m_0 c} = \frac{1}{2} \frac{e^2 E_0^2 \text{Sin}^2(kx - \omega t)}{m_0^2 c^2 \omega^2} = \frac{1}{2} a^2, \quad (\text{A.17})$$

where a is the normalized vector potential,

$$a = \frac{e E_0 \text{Sin}(kx - \omega t)}{m_0 c \omega} = a_{\max} \text{Sin}(kx - \omega t) \quad (\text{A.18})$$

The time-averaged p_x is:

$$\left\langle \frac{p_x}{m_0 c} \right\rangle = \frac{1}{2} \langle a^2 \rangle = \frac{1}{4} a_{\max}^2 \quad (\text{A.19})$$

In a similar way, Eq. A.14 becomes:

$$\frac{P_y}{m_0 c} = a, \quad (\text{A.20})$$

with, again, a zero time-averaged value. Eq. A.17 and A.20 can be further used to determine the trajectory of the electron in the (x,y) plane, that is, y versus x.

First, let's write $\phi=k(x-ct)$. Then we derivate ϕ in respect to y:

$$\frac{d\phi}{dy} = k\left(\frac{dx}{dy} - c\frac{dt}{dy}\right). \quad (\text{A.21})$$

We continue with:

$$\frac{d\phi}{dy} = k\left(\frac{p_x}{p_y} - c\frac{dt}{dy}\right). \quad (\text{A.22})$$

We replace dt/dy with $\gamma m_0/p_y$ and obtain:

$$\frac{d\phi}{dy} = k\left(\frac{p_x}{p_y} - c\frac{\gamma m_0}{p_y}\right). \quad (\text{A.23})$$

Finally, after few more steps involving Eq. A.15, we have:

$$\frac{d\phi}{dy} = \frac{k}{a_{\max} \text{Sin}(\phi)}. \quad (\text{A.24})$$

Integration of Eq. A.24 results in:

$$y = \frac{a_{\max}}{k} [1 - \text{Cos}(\phi)] = \frac{a_{\max}}{k} [1 - \text{Cos}(kx - \omega t)]. \quad (\text{A.25})$$

Equation A.25 shows that the electron describes a sinusoidal motion in the direction of the electric field \mathbf{E} of the EM wave. To calculate x as a function of ϕ we write:

$$\frac{d\phi}{dx} = k\left(1 - c\frac{dt}{dx}\right) = k\left(1 - c\frac{\gamma m_0}{p_x}\right). \quad (\text{A.26})$$

We use γ from Eq. A.15 into Eq. A.26 and continue with:

$$\frac{d\phi}{dx} = k \left[1 - c \left(1 + \frac{p_x}{m_0 c} \right) \frac{m_0}{p_x} \right] = \frac{-2k}{a_{\max}^2 \sin^2(\phi)}. \quad (\text{A.27})$$

Integration of Eq. A.27 results in:

$$x = -\frac{a_{\max}^2}{4k} \left[\phi - \frac{1}{2} \sin(2\phi) \right]. \quad (\text{A.28})$$

We finally write the two equations for x and y:

$$\begin{aligned} y &= \frac{a_{\max}}{k} [1 - \cos(\phi)] \\ x &= -\frac{a_{\max}^2}{4k} \left[\phi - \frac{1}{2} \sin(2\phi) \right] \end{aligned} \quad (\text{A.29})$$

The trajectory of the electron can be now found by making a parametric plot of y vs. x through the variable ϕ , see Fig. 2.1 in Chapter 2.

Appendix B

Experimental Measurements Based On The Optical Kerr Effect

B.1 Production Of Picosecond, Multi-Wavelength CO₂ Laser Pulses

A wavelength-independent method for optical gating, based on the Optical Kerr Effect, is presented. Using this method, 100 ps, 10kW, two-wavelength pulses (10.3 μm and 10.6 μm) with a signal-to-background contrast of 10^5 are produced by slicing a long CO₂ pulse. The capability of gating consecutive pulses separated on a picosecond time scale using this method is also shown.

The OKE gating technique is based on the rotation of the polarization of a relatively long probe pulse during the time when the Kerr medium is birefringent. In our experiment the birefringence is excited in this nonlinear medium by a much shorter, 100 ps, 1.06 μm pump pulse through the molecular orientation effect. The Kerr cell is placed between a polarizer and an analyzer. The function of the polarizer is to “clean”

the polarization of the incoming CO₂ pulse and to transmit only linearly polarized radiation. The analyzer is used to dump the long CO₂ pulse and to transmit only the short gated pulse which has its polarization rotated by $\pi/2$ rad in the Kerr medium. In the middle infrared region the best choice for the Kerr medium is CS₂ which transmits both 10 μm and 1 μm pulses, has a large nonlinear index of refraction $n_2=10^{-20} \text{ m}^2/\text{V}^2$, and a very fast ~ 2 ps relaxation time[50].

In our experiment the pulse is generated by a laser operating on two CO₂ lines, 10P(20) and 10R(16), with wavelengths equal to 10.6 μm and 10.3 μm , respectively. The experimental setup is presented in Fig. B.1. In order to obtain simultaneous oscillation on two CO₂ lines with equal line ratio, a grating was used to separate the optical cavities for the lines, as suggested by Sheffield[15]. To obtain single-longitudinal-mode generation on each wavelength, a hybrid technique is used[51]. Thus, the folded hybrid cavity (Fig. B.1) has two low-pressure discharge sections and a TEA CO₂ module capable of producing a 400 ns, 70 mJ, two-wavelength pulse with good shot-to-shot reproducibility (5-7%). The gain switched CO₂ pulse contains ~ 120 kW of peak power. Such a multi-line laser resonator can be tuned on an arbitrary pair of lines with the line ratio controlled simply by varying the diffraction losses in the two cavities[16]. The pump pulse is produced by a Nd:YAG laser system that delivers pulses with energies up to 150 mJ in ~ 100 ps. The oscilloscope traces of the pump (1 μm) and probe (10.3 μm and 10.6 μm) pulses are presented in Fig. B.2. Relative

delay between these pulses was adjusted to provide gating at the maximum of the CO₂ laser pulse.

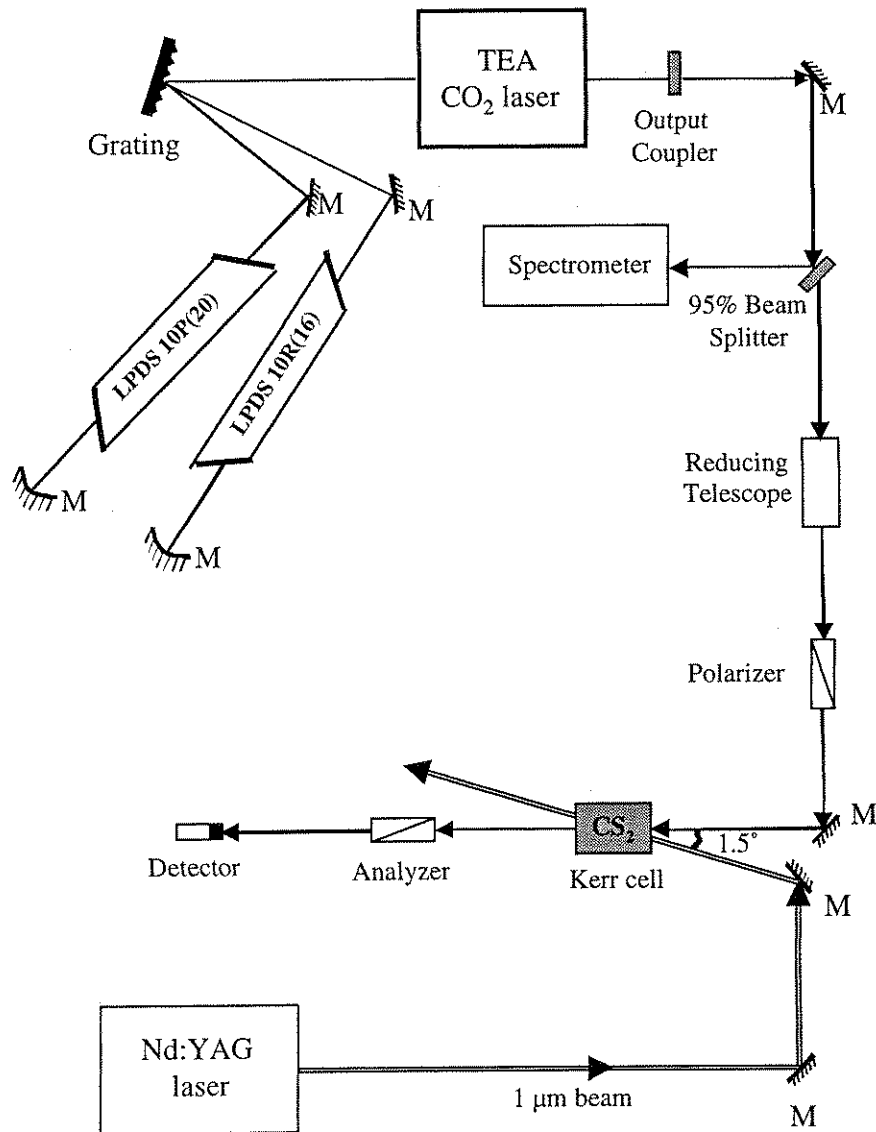


FIG. B.1: Schematic of the experimental setup for Kerr modulation of a two-wavelength CO₂ laser pulse: LPDS represents the low-pressure discharge sections and M is mirror.

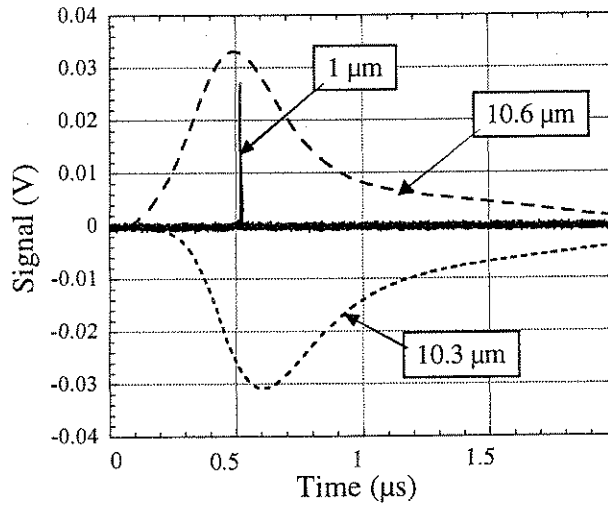


FIG. B.2: Temporal dynamics of the pulses involved in the gating process. The relative timing between the 10.6 μm and the 10.3 μm probe pulses from the CO_2 laser and the 1 μm pump pulse (10.3 μm trace is inverted).

In this experiment a 10^6 :1 extinction ratio for the 10- μm polarizer-analyzer system was necessary to provide a good signal-to-background contrast for the switched-out pulse. Any coated optical element, such as a beam combiner, present in the CO_2 beam path in between the polarizer and the analyzer, significantly decreases the polarizer-analyzer contrast. That is why a non-collinear interaction geometry between the pump and the probe pulses in the Kerr cell was used. A drawback of employing a non-collinear geometry is that the CO_2 pulse has to “fit” within the 1- μm beam inside the CS_2 cell. For this purpose we reduced the beam size of the 10- μm laser and made the angle between the two beams as small as possible. The beam size of the 10- μm radiation coming out of the CO_2 laser was reduced four times to approximately $2w_0=2$ mm, with the help of a beam compressor, while the beam size of the 1- μm laser was around $2w_0=6$ mm. The angle between the beams was 1.5° and the 2-cm long Kerr

cell was translated from the intersection point ± 1 cm along the CO_2 path without significant change in the gated signal. Therefore, it can be concluded that the interaction between the two laser pulses was present along the entire length of the cell.

It is known that the Kerr effect is most efficient when the angle between the polarizations of the probe and pump beams is $\pi/4$ rad. That is why the polarization of the $1 \mu\text{m}$ laser pulse was rotated and “cleaned” using a combination of a half-wave plate and a high-energy polarizer cube with extinction ratio $10^4:1$. Although the CO_2 laser output is p-polarized, the optics used to transport the beam from the oscillator to the Kerr cell induce significant depolarization of the infrared beam. To obtain a linearly polarized CO_2 pulse, two Ge plates, one set at the Brewster angle for $10.6 \mu\text{m}$ and the other for $10.3 \mu\text{m}$, were used as a polarizer. For the analyzer, 6 Ge plates and a low-power wire polarizer were used. Using this polarizer-analyzer combination, a maximum extinction ratio of 10^6 was achieved. It was important to use uncoated NaCl windows for the Kerr cell in order to maintain this high extinction ratio when the cell was placed in between the polarizer and the analyzer. The total losses introduced in the CO_2 beam, including absorption in the CS_2 cell, were approximately 50% of the output of the oscillator.

The transmission of the probe beam through the Kerr cell is given by[52]:

$$T(t) = A \sin^2 \left[2.34 \times 10^6 \left(\frac{\pi L}{\lambda} \right) n_2 I_{\text{pump}}(t) \right] \quad (\text{B.1})$$

where A is the total attenuation of the $10\text{-}\mu\text{m}$ beam due to the optical elements used in the path ($A=0.5$), L is the interaction length ($L=2$ cm), λ is the wavelength of the probe

beam ($\lambda=10\ \mu\text{m}$) and $I_{\text{pump}}(t)$ is the intensity of the pump pulse as a function of time in W/cm^2 (for a 100 mJ pulse the peak intensity is $3.5\ \text{GW}/\text{cm}^2$). For the above-mentioned parameters, the peak transmission of the 10- μm beam becomes 12%, corresponding to a maximum rotation in polarization of the CO_2 pulse of $\pi/6$ rad.

For these parameters, we measured the transmission of the Kerr switch using both a fast-response ($<1\text{ns}$) photoelectromagnetic detector (Boston Electronics PEM-L-3) and an energy meter. The detection system is not fast enough to resolve picosecond CO_2 pulses and was mainly used to monitor the contrast of the gated pulse. The pulse energy was measured using a Gentec energy meter with a sensitivity of 217 V/J, coupled to a Gentec 100x amplifier. The maximum energy recorded in the switched-out pulse was 1.1 μJ when pump pulses with intensities of $3.5\ \text{GW}/\text{cm}^2$ were utilized. The degradation of the CS_2 due to dissociation begins to occur beyond pump intensities of $3.5\ \text{GW}/\text{cm}^2$. After approximately 5 hours of operation at 1Hz repetition rate the Kerr medium became yellowish and the CS_2 was replaced to avoid any degradation of the performance of the system. Because self-focussing of the CO_2 pulse inside the CS_2 cell could affect the interaction geometry, we monitored the CO_2 beam profile using a pyroelectric 2-D array detector (Spiricon Pyrocam). No significant changes in the spatial profile of the 10- μm beam were observed.

The energy in the switched-out pulse of approximately 1 μJ corresponds to a 10% power switching efficiency for a pulse that is 100 ps long. This number is close to the theoretically calculated efficiency (Eq. B.1) of approximately 12%. The slight

difference could be attributed to the absorption of the pump pulse inside the Kerr cell, which is neglected in Eq. B.1. Since it is difficult to record mid-infrared pulses with picosecond time resolution, we investigated the switched-out pulse by replacing the probe CO₂ pulse with a 658 nm single-longitudinal-mode laser diode pulse in a similar switching geometry. As a detector we used a streak camera (Hadland Photonics Imacon 500) with <10 ps resolution. In Figure 3, three streaks of the gated visible pulse taken at pump intensity levels of 0.85 GW/cm², 1.6 GW/cm² and 2.6 GW/cm² are shown.

The temporal shape of the switched-out visible pulse is shown in Fig. B.3 (a). The polarization of the visible beam is rotated by $\sim\pi/2$ rad when the peak power of the pump beam reaches approximately 0.85 GW/cm². The pulse length (FWHM) is ~ 100 ps. Slightly smaller values were recorded when the rotation in polarization was less than $\pi/2$ rad. Due to the nonlinearity of the switching process, the width of the gated pulse is not necessarily the same as the width of the pump pulse. To investigate this issue, we modeled the shapes and the widths of the switched-out pulses when Gaussian, Lorentzian, and triangular pump pulses are employed. The theoretical calculations show that the gated pulses have widths comparable to the pump when the rotation of the probe beam polarization is close to $\pi/2$ rad. Even though for smaller values of rotation the calculations show that the switched-out pulse is slightly shorter than the pump pulse, we do not expect significant shortening of the switched-out CO₂ pulses when 10% switching efficiency is recorded. Therefore, the duration of the gated 10- μm pulses should be approximately 100 ps (FWHM).

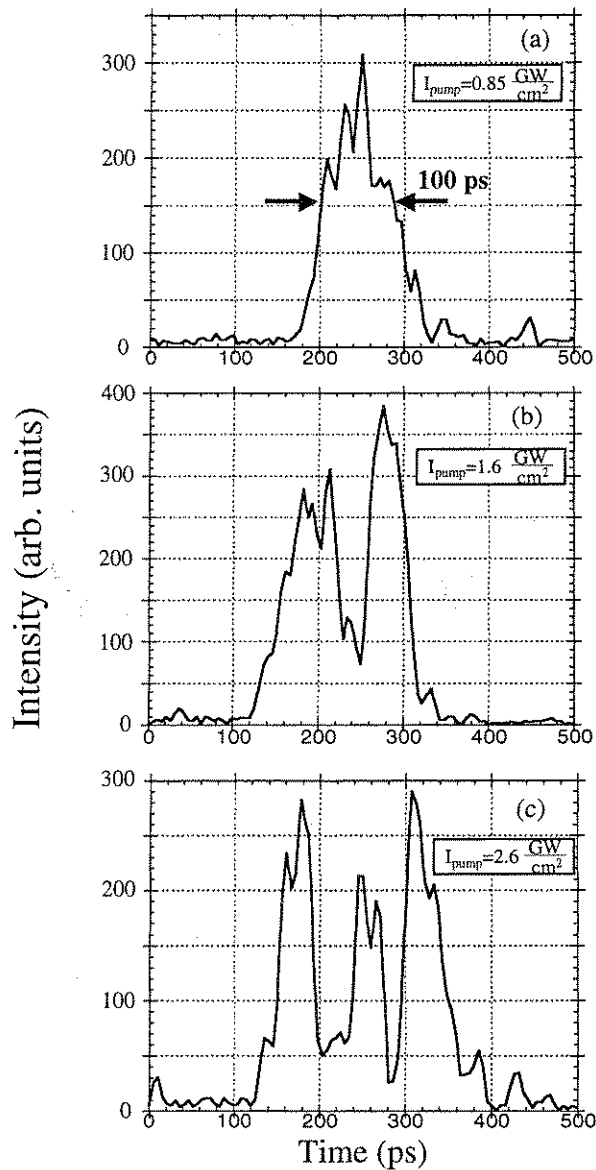


FIG. B.3: Temporal profile of the switched-out 658 nm pulse recorded with a streak camera at three different pump intensities. These intensities correspond to a rotation of the polarization of the probe pulse of: (a) $\pi/2$ rad; (b) π rad and (c) $3\pi/2$ rad.

Also, in this experiment, with lasers operating on 10 μm and 1 μm wavelengths, the dispersion of CS_2 of approximately 0.9 ps/cm does not produce any significant broadening of the gated pulse. The phenomena of dispersion in the Kerr medium and

the limited response time of CS₂ become important when shorter pump pulses (1-10 ps) are employed. Ultimately, mid-infrared pulses as short as 2 ps can be produced using this technique.

Figures B.3 (b) and B.3 (c) show the temporal profile of the gated visible pulse when pump pulse intensities of 1.6 GW/cm² and 2.6 GW/cm² were employed, respectively. For these levels of pump power the OKE induced in the Kerr cell is strong enough to produce “over-rotation”[53] of the polarization of the probe pulse with π rad [Fig. B.3 (b)] and $3\pi/2$ rad [Fig. B.3 (c)]. This shows that the switching mechanism presented here based on OKE can be used to gate a series of consecutive pulses separated in time by few tens of picoseconds while maintaining the same high-contrast and the same switching efficiency. The ability to construct an optical modulator based on OKE in CS₂ may become very important when a train of CO₂ pulses is required[54].

In conclusion, a wavelength-independent technique for gating CO₂ laser pulses on a picosecond time-scale with parameters suitable for further amplification is demonstrated. This has produced two-wavelength, 10.3 μm and 10.6 μm , CO₂ laser pulses with duration of $\sim 100\text{ps}$ and signal-to-background contrast of 10^5 . The energy contained in these pulses is 1 μJ and this corresponds to a 10% power switching efficiency. The capability of this method to gate a train of mid-infrared pulses separated on picosecond time scale has been shown.

Compared to the previous OKE device used to streak the infrared pulses[55], the new device presents some advantages (besides the compact body). A pair of diaphragms (Iris #1 and Iris #2, see Fig. B.4) and a Ge-slab beam combiner are used to align on the same axis the focussed CO₂ beam and the focussed visible beam. This precise alignment allows this device to streak infrared pulses with peak powers as low as few tens of kW. The system uses a 20-mW visible pulse produced by a diode laser which is more stable in time (no spikes) compared to a powerful probe pulse offered by a frequency-doubled Nd:YAG laser. When very low power CO₂ pulses need to be measured, such an intense probe pulse can also be used with this system due to the high-damage threshold and wide broadband of the high-contrast (10⁵:1) polarizer-analyzer pair. This pair of thin-film polarizers is superior to the previously used pair of polarizing cubes as they do not change the direction of propagation of the probe beam when they are moved in or out of the system (sometimes necessary for alignment). The contrast of the polarizer-analyzer pair is also good enough so that even a cw source of visible light can be used as a probe light (a He-Ne laser, for example). This setup was successfully used to measure the CO₂ pulse time delay introduced by the active gain medium in the LAA, see Appendix C.

B.3 Delay Of The CO₂ Pulses In The Large Aperture Amplifier

The synchronization of the CO₂ pulse with the electron bunch has been done in two steps. First, the CO₂ pulse produced by the RA was synchronized with the e-beam. This pulse is produced every 4 seconds and propagates three times through the 2.5-m long

LAA that has no inversion of population. The modulation of the transmission of the infrared pulse through a 1-mm thick slab of Ge is used to perform cross-correlation measurements. More details on this step can be found in Ref. [56]. The second step necessary to synchronize the high-power CO₂ pulses with the electron bunch consists on the measurement of the delay acquired by these pulses while they are strongly amplified in the LAA. Even if the CO₂ pulses originate from a laser system operating at the center of the 10P(20) and 10R(16) lines, the 100-ps short pulses that are injected into the second and the third pass of the LAA have a significant blue chirp imposed by the plasma shutter. The higher-frequency part of the pulse “sees” a higher index of refraction of the inverted gain medium and, therefore, will propagate slower in comparison with the no-gain case. It is necessary to measure this delay in order to compensate the timing of the CO₂ pulse to match that of the electron bunch. This was done by comparing the timing of the unamplified and amplified CO₂ pulses with a third reference signal. This signal is actually the 532-nm pulse that is used to create the electron bunch. As we mentioned in Chapter 4, this pulse originates from one of the 100-ps, 1064-nm pulses that are part of the cw pulse train offered by the “clock” of the Neptune laboratory, the cw mode-locked Antares Nd:YAG laser. The pulse was shortened by chirping it into a 500-m long single-mode fiber followed by the subsequent compression with a pair of gratings. The 1064-nm pulse was frequency-doubled to 532-nm (green) using a non-linear crystal.

The streak camera was used to record the visible pulse that is “locked” with the unamplified CO₂ pulse. Both the amplified and unamplified CO₂ pulses were streaked

using the Kerr setup mentioned above in Section B.2. An optical delay line was used to bring the visible pulse and the unamplified CO₂ pulse within 500 ps in order to precisely record the time delay between them, Δt_{un} . The delay was observed to be constant, as expected from two laser pulses originating from the same “clock”, as long as the temperature of the fiber is maintained the same. When the LAA was “fired” and the CO₂ gain medium became inverted, another delay was recorded between the visible pulse and, this time, the amplified CO₂ pulse, Δt_{am} . Note that the attenuators introduced in the path of the 10- μ m beam did not significantly increase the optical path of the amplified CO₂ pulse. The difference $\Delta t = \Delta t_{am} - \Delta t_{un}$ represents the delay acquired by the 10- μ m pulse while it is amplified in the LAA. Figures B.5 (a) and B.5 (b) show the streak camera images that recorded the visible (reference) pulse together with the unamplified and the amplified CO₂ pulses, respectively. Figure B.5 (c) shows on one single plot a time lineout of all four events, the visible and the unamplified CO₂ pulses, see Fig. B.5 (a), plus the visible and the amplified CO₂ pulses, see Fig. B.5 (b). The delay Δt accumulated by the 10- μ m pulse in the LAA is, as revealed by a series of measurements, $\Delta t = 120 \pm 20$ ps.

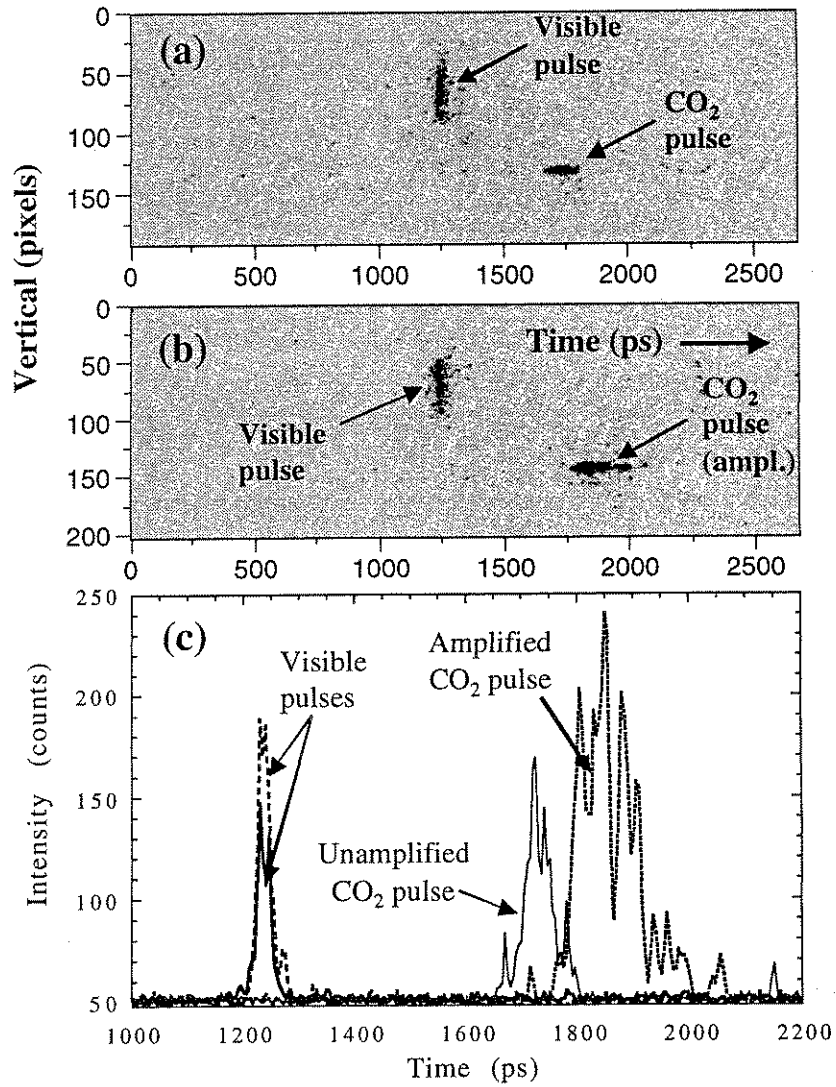


FIG. B.5: (a) Streak camera image of the visible (reference) pulse and the CO₂ pulse that passes through the no-gain LAA (unamplified). (b) Streak camera image of the visible pulse and the CO₂ pulse that is amplified in the LAA. (c) Temporal lineouts of all four events shown in (a) and (b).

Appendix C

90° Thomson Scattering From Non-Relativistic Plasma Waves

C.1 Scattering Geometry

When a powerful electromagnetic (EM) wave propagates through an underdense plasma a number of parametric instabilities, in which electrostatic plasma waves are excited, can take place. The incident EM wave decays into scattered secondary EM waves and various plasmons. The study of the excitation of these plasma waves is important given the fact that, in some cases, nearly all energy in the incident EM wave can be transferred into the scattered waves. These newly created plasma waves can be detected using an independent probe laser pulse to perform Thomson scattering. The intensity of the probe pulse has to be large enough to produce detectable scattered signal and, at the same time, small enough not to perturb the plasma waves from which the scattering takes place. In the Neptune laboratory we used the 50 MW, 532-nm visible pulse to probe plasma waves like the Stimulated Raman Scattering (SRS) and Stimulated Brillouin Scattering (SBS) for both the $f/3$ and the $f/18$ focusing schemes.

The Raman instability can be most simply characterized as the resonant decay of an incident photon (frequency ω_0 and wavenumber \mathbf{k}_0) into a scattered photon (ω_s , \mathbf{k}_s) plus an electron plasma wave (ω_{epw} , \mathbf{k}_{sepw}). The energy and momentum conservation equations are:

$$\begin{aligned}\omega_0 &= \omega_s \pm \omega_{epw} \\ \mathbf{k}_0 &= \mathbf{k}_s \pm \mathbf{k}_{epw}.\end{aligned}\tag{C.1}$$

Among the various Raman instabilities that are excited by 100-ps long laser pulses in plasma densities of $0.1\% \times n_{crit}$ (critical density for 10- μm radiation), the one that has the largest growth rate is the backscatter SRS[57]. The plasma waves excited in this process have a frequency $\omega_{SRS} \cong \omega_p$ and a wavenumber $k_{SRS} \cong 2 \times k_0$.

The Brillouin instability represents the decay of the incident EM wave into another EM wave and an ion acoustic phonon. The energy and momentum conservation equations are also represented by Eqs. C.1. In this case, the plasma waves have a frequency $\omega_{SRS} \cong 2k_0 \times c_s$ and a wavenumber $k_{SRS} \cong 2 \times k_0$ (for the backscatter SBS). Here, c_s is the ion acoustic velocity. More details about the SRS and SBS waves, like the growth rates, dispersion relations, etc., can be found in Ref. [58].

Once the SRS and the SBS waves are excited in the plasma, their detection using TS is done by first establishing the scattering geometry. In this Appendix we calculate the scattering angles at which the incident (probe) and the emerging (scattered) beams have to intersect the plasma in order to maximize the scattering process on a SRS plasmon. The energy and momentum conservation equations (for the TS measurements) are:

$$\begin{aligned}\omega_i &= \omega_e + \omega_p \\ \mathbf{k}_i &= \mathbf{k}_e + 2\mathbf{k}_0,\end{aligned}\tag{C.2}$$

where the i and e indexes stand for the incident and emerging EM waves. A diagram of the scattering geometry is shown in Fig. C.1.

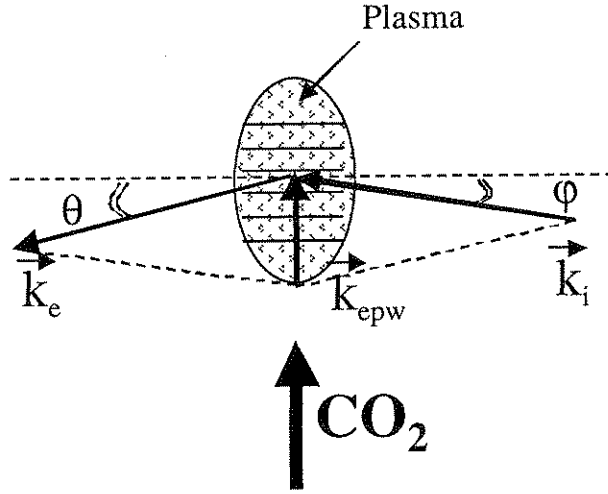


FIG. C.1: Thomson scattering geometry where an incident EM wave (\mathbf{k}_i) scatters off a non-relativistic plasma wave (\mathbf{k}_{epw}) into an emerging EM wave (\mathbf{k}_e). The plasma wave is excited by a CO_2 pulse propagating in plasma.

The Equations C.2 can be rewritten by breaking down the momentum conservation relation on the vertical and horizontal axes:

$$\begin{aligned}ck_i &= ck_e + ck_p \\ k_i \sin(\varphi) &= -k_e \sin(\theta) + 2k_0 \\ k_i \cos(\varphi) &= k_e \cos(\theta),\end{aligned}\tag{C.3}$$

where $k_p = \omega_p/c$. This set of equations provide the following expressions for the scattering angles θ and φ :

$$\begin{aligned}\theta &= \text{Arcsin}\left[\frac{4k_0^2 + k_p^2 + 2k_i k_p}{4k_0(k_p + k_i)}\right] \\ \varphi &= \text{Arctan}\left[\frac{2k_0}{\text{Cos}(\theta) \times (k_i + k_p)} - \tan(\theta)\right].\end{aligned}\tag{C.4}$$

Therefore, for the SRS case the scattering angles are: $\varphi=1.99^\circ$ and $\theta=3.75^\circ$. The total deflection angle for the incident probe beam is $\varphi+\theta=5.753^\circ$. Similar values are obtained in the case of TS on SBS waves, $\varphi=2.88^\circ$, $\theta=2.88^\circ$, and the total deflection angle is $\varphi+\theta=5.758^\circ$. Since in both cases the total deflection angle has approximately the same value, 5.75° , it means that the TS measurements could be done in such a way that both the SRS and the SBS waves be detected simultaneously using one single probe beam.

C.2 Experimental Setup

Figure C.2 shows a schematic of the TS experimental arrangement in the interaction chamber. The two arms of the 10- μm beam, $f/3$ and $f/18$, can be fired both independently or simultaneously. The probe pulse is brought sideways to the plasma, at the scattering angles calculated above. The beam passes through a viewing dump in order to minimize the stray light that would scatter on all of the chamber walls. The main part of the probe beam is sent into a special dump that also minimizes the backscattered stray light. The TS light is collected with a lens and transported towards the detection system formed by a spectrometer-streak camera combination. Various CCD cameras are used to spatially align the three laser beams. The images of the plasmas created in one single shot by the two arms of the 10- μm laser pulse are shown in the right side of Fig. C.2.

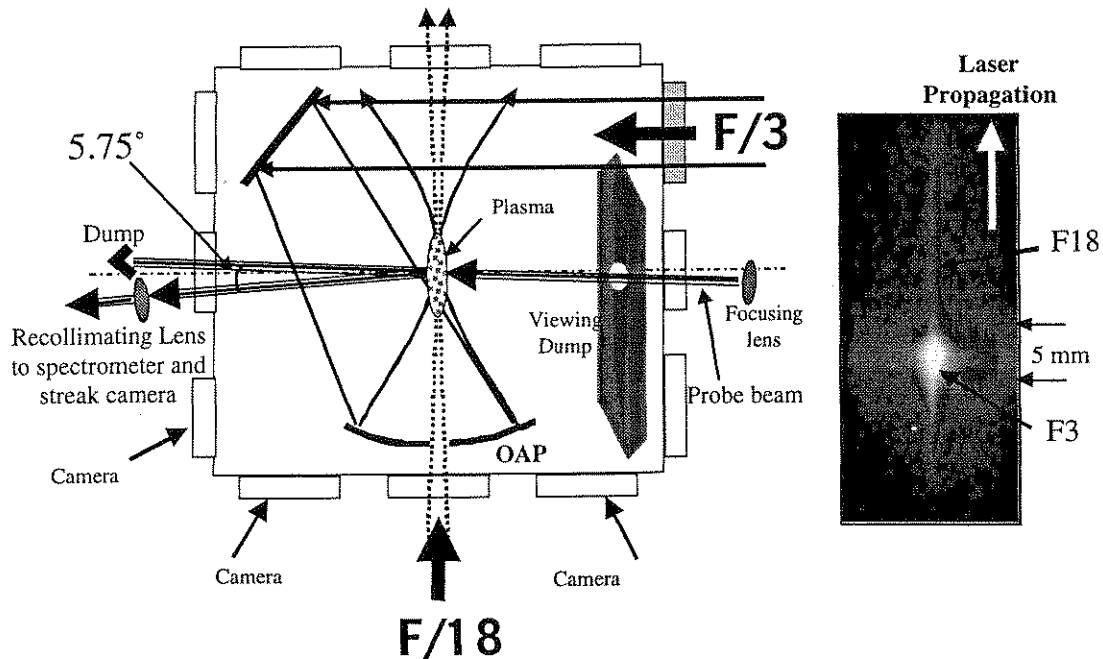


FIG. C.2: Schematic of the Thomson scattering geometry in the interaction chamber, left. Images of the two plasmas created simultaneously by the $f/3$ and the $f/18$ arms of the $10\text{-}\mu\text{m}$ laser beam, right.

C.3 Experimental Results

Figure C.3 shows the frequency and time-resolved streak camera images of the scattered light for the 90° TS experiment performed on the $f/3$ plasma with the laser operating only on the $10.6\text{ }\mu\text{m}$ wavelength. The peak power of the laser pulse was 10^{15} W/cm^2 . Two features can be distinguished besides the ns-long leakage of the probe light at $\lambda_{\text{probe}}=532\text{ nm}$ (zero wavelength shift). One is the SRS signal, shifted in frequency with the wavelength shift that corresponds to ω_p at a H_2 gas pressure of 215 mTorr. A series of 90° TS measurements were undertaken at different pressures (plasma densities). The wavelength (frequency) shift for the SRS signal was recorded and this information was used to make the plot shown in Fig. 5.1 (Chapter 5) that shows

the value of the TS measured plasma density versus the pressure of the fill gas. The second feature in Fig. C.3 is the SBS signal that is not measurably shifted in frequency compared to the 532-nm probe light. This is expected since the frequency of the SBS plasmon is $\omega_{\text{SRS}} \cong 2k_0 \times c_s$, a value much smaller compared to ω_p .

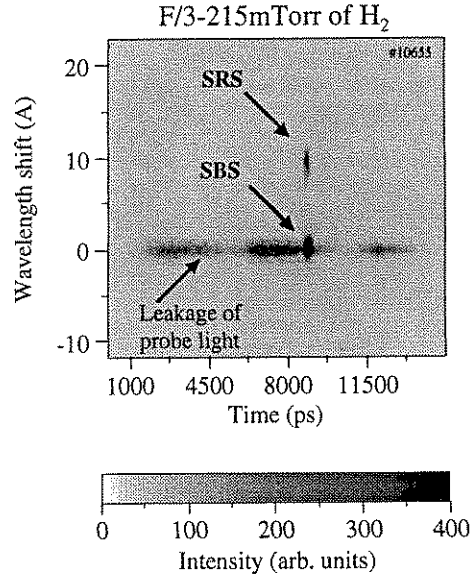


FIG. C.3: Frequency and time-resolved streak camera images of the f/3 Thomson scattered light. The vertical is the wavelength shift from the 532-nm probe light and the horizontal is the time scale in picoseconds. The H_2 gas pressure was 215 mTorr ($n=0.13\% \times n_{\text{crit}}$) and the laser intensity up to 10^{15} W/cm^2 .

Both electrostatic plasma waves are excited and exist for the duration of the laser pulse. When the time scale was expanded, the two plasma waves were shown to coexist simultaneously in the plasma. When the plasma density was raised up to $n=2.4 \times n_{\text{res}}$ ($n_{\text{res}}=10^{16} \text{ cm}^{-3}$), which is around 400 mTorr of H_2 , the SBS signal steadily increased and dominated the spectrum of the TS light to the extent where the Raman waves could not be detected anymore.

Another set of TS measurements was performed on the f/18 produced plasma waves. Figure C.4 (a) shows a typical time-resolved spectrum of the plasma waves that are excited in the ~30-mm long plasmas. Surprisingly, as opposed to the f/3 TS spectra, no SRS or SBS type of signals was recorded. Instead, the streak shows a bright, intense feature having a wavelength shift corresponding to a frequency shift of slightly less than $\omega_p/2$. This feature has been recorded for tens of f/18 shots, with not even on single shot showing any SRS or SBS signals. Figure C.4 (b) shows the temporal profile of the light scattered in this feature. The duration of the TS light is approximately the same with that of the 10- μm pulse, 100 ps (FWHM). The plasma density was varied up to $2 \times n_{\text{res}}$ and a series of TS measurements were undertaken. No correlation was established between the plasma density and the wavelength shift of this Thomson scattered light. More precise measurements are needed in order to exactly determine the frequency and the wavenumber of these plasma waves. The difference between the f/3 and the f/18 TS spectra was exploited as a method of synchronization of the plasma waves excited when both arms are fired simultaneously.

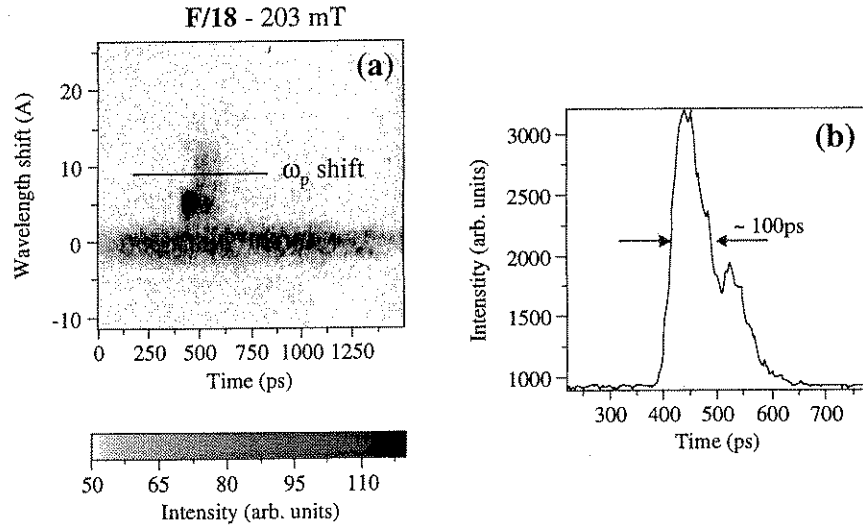


FIG. C.4: (a) Frequency and time-resolved streak camera images of the $f/18$ Thomson scattered light. The vertical is the wavelength shift from the 532-nm probe light and the horizontal is the time scale in picoseconds. The H_2 gas pressure was 203 mTorr ($n=0.12\% \times n_{crit}$) and the laser intensity up to $4 \times 10^{14} \text{ W/cm}^2$. (b) Lineout from (a) through the bright feature that has a $\sim 5 \text{ \AA}$ wavelength shift.

Figure C.5 (a) shows the streak camera image of the Thomson scattered light when both the $f/3$ and the $f/18$ arms were fired in one shot ($10.6 \mu\text{m}$ only). Both arms produced plasmas and excited plasma waves. The $f/3$ pulse reached the center of the interaction chamber $\sim 50 \text{ ps}$ before the $f/18$ one. Each arm produced individually their own characteristic TS signals on the streak camera: the $f/3$ excited the SRS and SBS waves, while the $f/18$ excited the unusual “ $\omega_p/2$ ” feature.

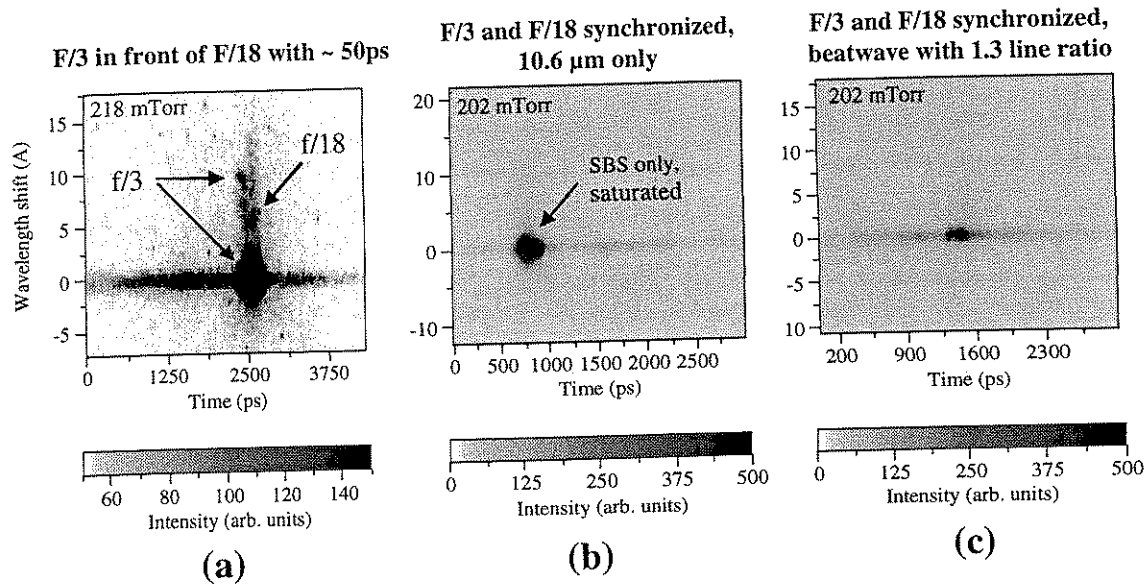


FIG. C.5: Time-resolved spectra of the TS light for: (a) a $f/3$ and $f/18$ single shot with the $f/3$ arm producing the plasma 50 ps before the $f/18$ arm; shot is $10.6 \mu\text{m}$ only and is taken in 218 mTorr of H_2 (b) a synchronized $f/3$ and $f/18$ shot in 202 mTorr of H_2 (single frequency, $10.6 \mu\text{m}$ only) (c) synchronized, $f/3$ and $f/18$ beatwave shot with 1.3 line ratio in 202 mTorr of H_2 .

Figure C.5 (b) shows a typical TS spectrum when the $f/3$ and the $f/18$ arms were synchronized within 10 ps. The laser system operated on $10.6 \mu\text{m}$ wavelength only. The spectrum shows only one feature, a powerful SBS signal. While the SRS and SBS waves coexisted for the TS shots taken with the $f/3$ arm only, it appears that the “addition” of the $f/18$ arm quenches the SRS plasma waves, whose signature signal is not recorded anymore by the streak camera. In addition, the feature that is characteristic to the $f/18$ -only TS measurements, is also suppressed. Note that this competition process is recorded only at the location where the probing is done.

The 90° TS measurements also provided indirect evidence for the existence of relativistic plasma waves when the laser system operated on both the 10.6 and the $10.3 \mu\text{m}$ lines, as a part of the “double beatwave experiment”[59]. Figure C.5 (c) shows

the TS spectrum for a two-frequency shot where the $f/3$ and $f/18$ arms were fired simultaneously. The SBS signal was few times less intense, compared to the one recorded in Fig. C.5 (b), at similar levels of laser power. It is believed that the relativistic plasma wave interferes in the Brillouin excitation process and that results in a reduction in the amplitude of the SBS waves and, correspondingly, a decrease in the TS signal.

Overall, the results from the 90° TS measurements showed that various non-relativistic waves are excited when the laser pulse propagates through the plasma. The use of two different focusing schemes, $f/3$ and $f/18$, determine the excitation of different plasma waves. The waves excited by the two laser pulses can be synchronized on-line to within 10 ps using the unobtrusive 90° TS probing setup. Indirect evidence for the excitation of RPWs can be inferred from the reduction of the SBS signal recorded by the streak camera.

Appendix D

High-Amplitude Non-Resonant Plasma Waves

Successful acceleration of electrons to ultra-high energies relies on the existence of high gradients of acceleration over meter long interaction lengths. As it has been shown in Chapter 3, the resonantly excited RPWs become gradually dephased with respect to the beat pattern of the laser pulse. In order to avoid this dephasing in the acceleration of phase-locked electrons, the injection time has to be early, before the dephasing appears and, correspondingly, before the wave grows to a large amplitude. This means that the peak power of the laser pulses (having typically a normalized vector potential $a > 0.3$) is not optimally used. This excess power can be used by increasing the transverse size of the laser beam and, consequently, the interaction length. Given the fact that today's laser system can produce laser pulses with $a \gg 1$, the increase in the interaction length would be significant. Then it is necessary to have available very long, uniform and stable plasmas, which are usually difficult to produce. Higher accelerating gradients could be produced by resonant RPWs at higher plasma densities, with the drawback of having plasma waves with smaller wavelengths ($< 100 \mu\text{m}$). Experimentally, loading

phase-locked electrons in the buckets of these waves could reach the spatial and temporal limits imposed by the jitter effects in the PBWA.

It may be possible to excite non-resonant RPWs at $n \gg n_{res}$ that will create accelerating fields on the order of few GV/m over reasonable (<1 meter) interaction lengths and with periods larger than 300 μm . Such an acceleration structure would efficiently use the peak power of the laser pulse and will be free of dephasing, regardless of the eventual plasma density inhomogeneities. In this chapter we evaluate through 2-D simulations the possibility for these non-resonant waves to produce high gradients of acceleration.

One way to increase the amplitude of the plasma waves is to excite them with stronger laser pulses. The intensity of the two-frequency laser pulse was increased from $a_1=a_2=0.1$ to $a_1=a_2=1$ in a series of 2-D simulations. The spot size was kept constant at $w_0=50 \mu\text{m}$. The simulation box was “filled” with H_2 that was ionized by the laser pulse to produce an initial plasma density $n=7 \times n_{res}$. The dots in Figure D.1 show the maximum value of the longitudinal electric field E_x associated with the non-resonant plasma waves versus the strength of the laser pulse represented by the normalized vector potential a . In these simulations the line ratio was always 1, that is, $a_1=a_2=a$. The continuous line in Fig. D.1 represents a power-of-two fit of the data. As expected, E_x increases with increasing a and is proportional to the (ponderomotive) force that drives the non-resonant oscillator, which, in turn, is proportional to a^2 . Thus, by increasing the power of the driving pulse, the accelerating fields could go up to few GV/m. This represents a significant fraction, slightly more than 10% of the upper limit for these

fields in a plasma of density n , $E_{\text{cold}}[\text{MV/cm}] \approx (n[\text{cm}^{-3}])^{1/2}$. For example, in Chapter 3 it was shown that the maximum E_x that can be used for acceleration at resonance (the “coherent” E_x before the dephasing appears) is 8-10 MV/cm out of the maximum 100 MV/cm at $n=n_{\text{res}}=10^{16} \text{ cm}^{-3}$.

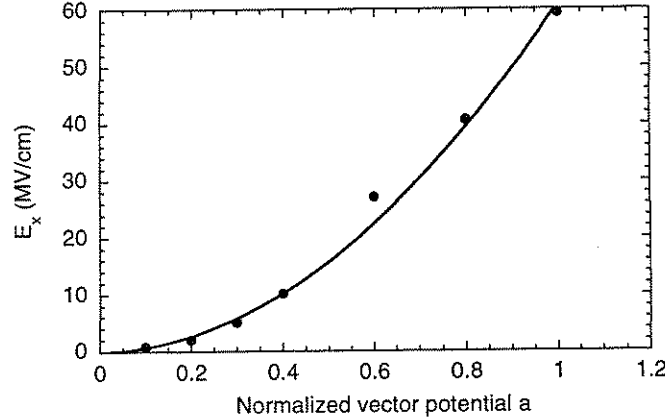


FIG. D.1: Maximum value of the longitudinal electric field E_x (dots) associated with the relativistic plasma waves excited at $n=7 \times n_{\text{res}}$ versus the normalized vector potential a of the laser pulse. The spot size used in the 2-D simulations is $w_0=50 \mu\text{m}$.

Therefore, approximately 10% of the maximum available field can be used to accelerate electrons, regardless of the power of the laser pulse. A similar value can be used for the non-resonant excitation, too. From Fig. D.1 one can see that an electric field of $\sim 30 \text{ MV/cm}$ (slightly more than 10% of the maximum 265 MV/cm that can be produced at $7 \times 10^{16} \text{ cm}^{-3}$) can be used to accelerate electrons, of course using more intense pulses with $a_1=a_2=a \geq 0.8$. Another difference is the wavelength of the plasma waves which is larger by a factor of $\sqrt{7}=2.65$ for the non-resonant RPWs.

The amplitude of the non-resonant fields could be further increased, together with an increase in the interaction length, by taking advantage of a lower laser power

threshold for the onset of relativistic self-focusing. According to Ref. [60], the self-focussing threshold for a $9 \times 10^{16} \text{cm}^{-3}$ could be achieved with CO_2 laser pulses having less than 1 TW of power. We performed 2-D simulations at a plasma density of $9 \times 10^{16} \text{cm}^{-3}$ ($n=9 \times n_{\text{res}}$). A 50-ps, two-frequency laser pulse with $a_1=a_2=0.6$ was focussed to $w_0=100 \mu\text{m}$ in a slab of preformed plasma. Note that the plasma fills the simulation box uniformly and no pre-formed plasma channel exists. A CO_2 laser pulse with these parameters would have a power of ~ 3 TW and would achieve an intensity of up to 10^{16}W/cm^2 . Figure D.2 (a) shows a snapshot of the normalized a^2 intensity of the beat pattern of the laser pulse close to the time when the peak of the pulse reached the simulation box. Figure D.2 (b) shows the ion distribution in the simulation box at that time. The coordinates are x (horizontal, from 0 to 4 mm) and y (vertical, from 0 to 0.36 mm). The intensity of the pulse on its axis is high enough as to lower the effective refractive index of the plasma in this region (the electrons oscillate slower in the laser field because of relativistic effects). Therefore, the laser pulse “guides” itself through this channel, creating the self-focusing mechanism. This effect is further enhanced by the expulsion of the plasma out of this axial region due to the transverse ponderomotive force of the pulse. Figure D.2 (b) shows the plasma channel on axis, while Fig. D.2 (a) shows the guiding of the laser pulse in this channel. While the plasma density inside the channel decreases up to 3 times of the initial value of $9 \times 10^{16} \text{cm}^{-3}$, the intensity of the pulse is increased by the guiding process. Figure D.2 (c) shows on the left vertical the lineout of the laser intensity on the axis of the beam in Fig. D.2 (a), and, on the right vertical, the horizontal lineout of the ion distribution in Fig. D.2 (b).

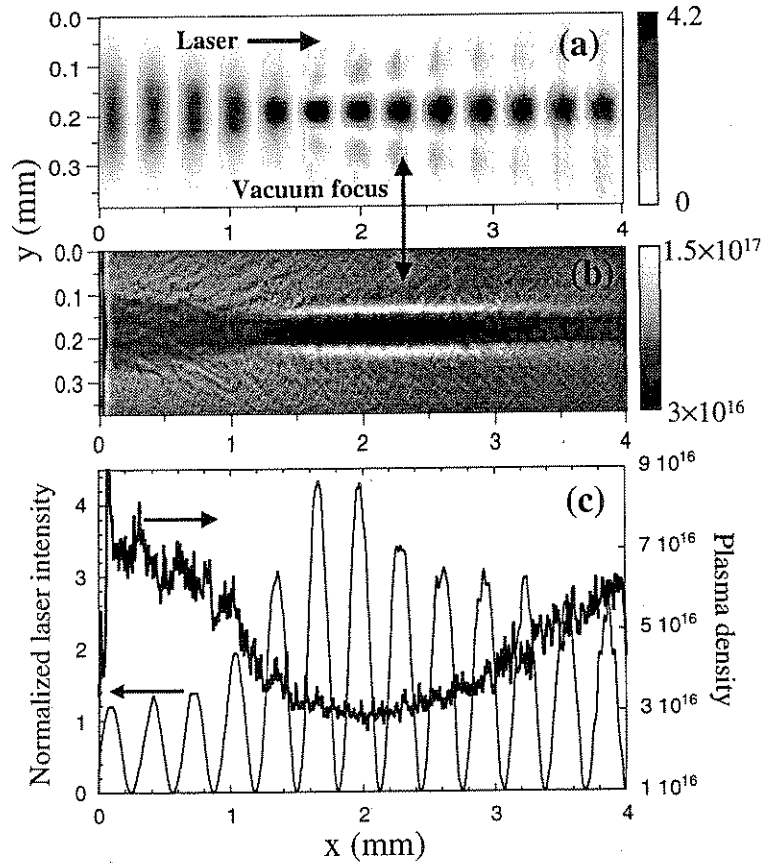


FIG. D.2: (a) Snapshot of the normalized intensity of the two-frequency laser pulse. (b) Snapshot of the ion density distribution. (c) Horizontal lineouts through the center of the simulation box for (a) and (b). The snapshots were taken at the same time, when the peak of the laser pulse reached the center of the box. The laser pulse moves from left to right.

The intensity of the laser pulse in the channel increases more than 2.5 times the maximum value of 1.44 that the laser would have in the vacuum focus. Almost the entire energy of the pulse is concentrated inside the 50- μm wide channel in which large amplitude plasma waves are being non-resonantly excited. Figure D.3 (a) shows a snapshot of the longitudinal electric field associated with the waves that are produced in the channel. Figure D.3 (b) shows a lineout of Fig. D.3 (a) along the laser axis. The

simulation results are noisy due to a reduced number of particles per cell that is used at plasma densities many times above the resonant density.

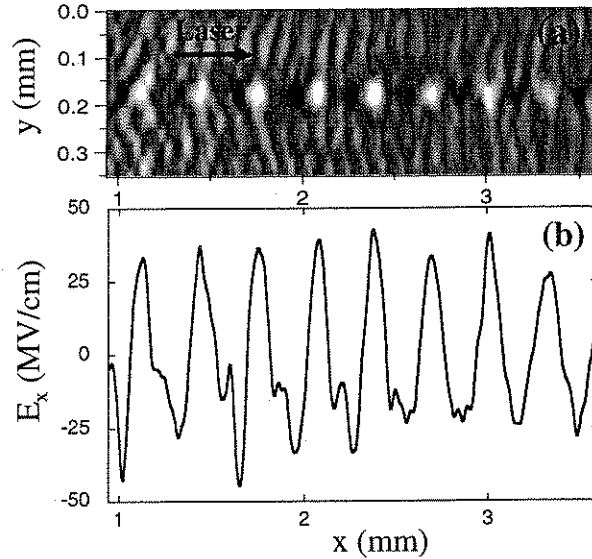


FIG. D.3: (a) Snapshot of the longitudinal electric field E_x of the plasma waves in the channel. (b) Horizontal lineout of (a) along the laser axis.

Positive electric fields E_x as high as 40 MV/cm are produced, with an average of ~ 30 MV/cm over the length of the channel, $L_{ch} \cong 2.7$ mm. Higher amplitude fields might be excited in such channels if the laser parameters and the initial values for the plasma density would be optimized.

The results from this 2-D simulation (Figures D.2 and D.3) represent just an example meant to show that the self focusing mechanism could be used to create plasma channels where high-amplitude electric fields are excited. A sum of other plasma instabilities, like the Raman forward scattering and SBS, are not modeled by the code used in the above simulations. Such phenomena might adversely affect the transportation of the laser pulse inside the channel and the excitation of the non-resonant RPWs.

Experimental evidence that supports these simulation results rely on the existence of intense two-frequency laser pulses with $a > 1$ and the production of high-density plasma slabs.

-
- [15] R. L. Sheffield et al. Appl. Phys. Lett. **29**, 588 (1976).
- [16] S. Ya. Tochitsky, R. Narang, C. Filip, B. Blue, C. E. Clayton, K. A. Marsh, and C. Joshi, Proceed. LASERS'99, December 13-16, Quebec, STS press McLean, VA, 2000, p. 265-272.
- [17] P.B. Corkum, IEEE J. Quantum Electron. **21**, 216 (1985).
- [18] R. Narang, Master thesis, UCLA 1999, Los Angeles, California.
- [19] A.E. Siegman, *Lasers*, University Science Books, Mill Valley, California 1986.
- [20] C. V. Filip, Master thesis, UCLA 1999, Los Angeles, California.
- [21] C.V. Filip et al. Appl. Optics **41**, 3743-3747 (2002).
- [22] S. Ya. Tochitsky et al. Opt. Lett. **26**, 813-815 (2001).
- [23] W. P. Leemans et al., Phys. Rev. A **46**, 1091 (1992).
- [24] P.B. Corkum et al., J. of Appl. Phys. **50**, 3079 (1979).
- [25] D. E Evans and J. Katzenstein. Rep. Prog. Phys. **32**, 207 (1969).
- [26] J. Sheffield. *Plasma Scattering of Electromagnetic Radiation*", Academic Press, New York 1975.
- [27] R. E. Slusher and C. M. Surko. Phys. Fluids **23**, 472 (1980).
- [28] C. E. Clayton et al. Phys. Rev. Lett. **54**, 2343 (1985).
- [29] F. Martin et al. Phys. Rev. Lett. **55**, 1651 (1985).
- [30] C. E. Clayton et al. Phys. Rev. Lett. **55**, 1652 (1985).
- [31] A. E. Dangor et al. Physica Scripta **T30**, 107 (1990).
- [32] F. Moulin et al. Phys. Plasmas **1**, 1318 (1994).

-
- [33] S.P. Le Blanc et al. Phys. Rev. Lett. **77**, 5381 (1996).
- [34] C. W. Siders et al. IEEE Trans. Plasma Sci. **24**, 301 (1996).
- [35] C. W. Siders et al. Phys. Rev. Lett. **76**, 3570 (1996).
- [36] J. R. Marquès et al. Phys. Rev. Lett. **76**, 3566 (1996).
- [37] A. K. Lal et al. Phys. Plasmas **4**, 1434 (1997).
- [38] A. Lal et al. Rev. Sci. Instrum. **68**, 690 (1997).
- [39] D. M. Villeneuve et al. J. Opt. Soc. Am. B. **8**, 895 (1991).
- [40] C.V. Filip et al. Rev. Sci. Instr. **74**, 3576 (2003).
- [41] W.J. Smith. *Modern Optical Engineering*, McGraw-Hill, New York, New York 1990, p. 239.
- [42] M. Born and E. Wolf. *Optics*, 7th (expanded) edition, Cambridge University Press, Cambridge 1999, p. 363.
- [43] D. N. Rao and V. N. Kumar. J. Mod. Opt. **41**, 1757 (1994).
- [44] T. L. Mikes. Can. J. of Spectroscopy **25**, 41A (1980).
- [45] H.A. Baldis et al. Applied Optics **21**, 297 (1982).
- [46] F. Amiranoff et al. Phys. Rev. Lett. **25**, 3710 (1992).
- [47] W. G. Rado. Appl. Phys. Lett. **11**, 123 (1967).
- [48] H. J. Lehmeier et al. Opt. Comm. **56**, 67 (1985).
- [49] S. Ya. Tochitsky et al. to be published.
- [50] M.A. Duguay and J.W. Hansen. Appl. Phys. Lett. **15**, 192 (1969).
- [51] D.M. Tratt et al. Prog. Quant. Electr. **10**, 229 (1985).

-
- [52] T.C. Owen et al. Appl. Phys. Lett. **22**, 272 (1973).
- [53] T. Morioka and M. Saruwatari. IEEE Journal on Selected Areas in Communications **6**, 1186, (1988).
- [54] T. Hirose, Proceed. LASERS'98, December 7-11, Tucson, AZ, STS press McLean, VA, 1999, p. 836-844.
- [55] M. J. Everett, Ph.D. dissertation, UCLA 1994.
- [56] R. Narang, Ph.D. dissertation, UCLA 2003.
- [57] D. W. Forslund et al. Phys. Fluids **18**, 1002 (1975).
- [58] W. L. Kruer, *The physics of laser plasma interactions*, Addison-Wesley Publishing Company, 1988.
- [59] R. Narang et al. Proceedings of the 2001 Particle Accelerator Conference, IEEE. Part vol.5, pp.3996-8, Piscataway, NJ, USA 2001.
- [60] P. Sprangle et al. Phys. Rev. Lett. **69**, 2200 (1992).